

# STUDY OF PLASMONIC PHENOMENA IN METAL NANOSTRUCTURE ARRAYS

by

**Yun-suk Jung**

B.S. in E.E., ChungAng University, 1994

M.S. in E.E., University of Pittsburgh, 2002

Submitted to the Graduate Faculty of  
Swanson School of Engineering in partial fulfillment  
of the requirements for the degree of  
Doctor of Philosophy

University of Pittsburgh

2009

UNIVERSITY OF PITTSBURGH  
SWANSON SCHOOL OF ENGINEERING

This dissertation was presented

by

Yun-suk Jung

It was defended on

July 22<sup>nd</sup>, 2009

and approved by

Joel Falk, Professor, Department of Electrical and Computer Engineering

William Stanchina, Professor, Department of Electrical and Computer Engineering

Minhee Yun, Assistant Professor, Department of Electrical and Computer Engineering

Rob Coalson, Professor, Department of Chemistry

Dissertation Director: Hong Koo Kim, Professor, Department of Electrical and Computer  
Engineering

Copyright © by Yun-suk Jung

2009

# **STUDY OF PLASMONIC PHENOMENA IN METAL NANOSTRUCTURE ARRAYS**

Yun-suk Jung, PhD

University of Pittsburgh, 2009

Metal nanostructures have received considerable attention for their ability to guide and manipulate light at the nanometer scale. As in the case of electronics, scaling down the dimensions of photonic devices is expected to bring numerous benefits in terms of speed, capacity, and energy efficiency in information processing. Surface plasmons, collective oscillation of electrons excited by light, are basically photon waves trapped/squeezed at a metal/dielectric interface. The reduced size in electromagnetic field distribution offers a potential for nanoscale reduction of photonic devices. The intrinsic coupling between electrons and photons also offers a potential for merging electronics and photonics on the same platform.

In this thesis, we have investigated metallic nanostructures as a medium for plasmonic interactions. Surface plasmons excited on a metallic structure can produce many interesting phenomena that can be observed in the near-field to far-field regime. We have studied the anomalous behavior of surface plasmons that are excited in a resonant cavity structure of a metal nanoslit array. We show that modification of a metal nanoslit array by a self-assembled monolayer of molecules can give rise to a blue-shift in the peak transmission wavelength. A simple model was developed to predict the wavelength shift and its sign. We have characterized the near- to far-field distribution of optical wavefronts emanating from a nanoslit formed in a thin silver film. The evolution of optical phases was imaged using a self-interference technique in conjunction with a scanning probe method. The phase relationship of the slit-transmitted

waves with respect to the direct transmission through the thin metal film is quantitatively established. We have investigated negative refraction of visible light that does not involve any negative-index media. The interfacial negative refraction without bulk media, demonstrated in this thesis, offers a promising approach to accessing angular ranges that have not been reachable in conventional optics.

## TABLE OF CONTENTS

<b>PREFACE.....</b>	<b>XIII</b>
<b>1.0 INTRODUCTION .....</b>	<b>1</b>
<b>1.1 OVERVIEW .....</b>	<b>1</b>
<b>1.2 DIELECTRIC CONSTANT OF METALS.....</b>	<b>3</b>
<b>1.3 SURFACE PLASMONS AT METAL SURFACES .....</b>	<b>9</b>
<b>1.4 SUMMARY.....</b>	<b>17</b>
<b>2.0 TRANSMISSION OF LIGHT THROUGH METALLIC NANOSLIT ARRAYS .....</b>	<b>18</b>
<b>2.1 INTRODUCTION.....</b>	<b>18</b>
<b>2.2 FABRICATION AND CHARACTERIZATION.....</b>	<b>20</b>
<b>2.2.1 Holography and E-beam lithography method .....</b>	<b>20</b>
<b>2.2.2 Focused ion beam etching method .....</b>	<b>21</b>
<b>2.3 CHARACTERIZATION AND ANALYSIS OF THE OPTICAL TRANSMISSION SPECTRA .....</b>	<b>27</b>
<b>2.3.1 Arrays of large number (<math>N &gt; 1000</math>) slits .....</b>	<b>27</b>
<b>2.3.2 Single slit and 2 ~ 10 slit arrays .....</b>	<b>36</b>
<b>2.4 SUMMARY.....</b>	<b>39</b>
<b>3.0 BLUESHIFT OF SURFACE PLASMON RESONANCE SPECTRA IN ANNEAL-TREATED SILVER NANOSLIT ARRAYS .....</b>	<b>40</b>
<b>3.1 INTRODUCTION.....</b>	<b>40</b>
<b>3.2 FABRICATION AND CHARACTERIZATION.....</b>	<b>41</b>

3.2.1	Fabrication of the silver nanoslit arrays.....	41
3.2.2	Characterization .....	44
3.3	RESULTS AND DISCUSSION.....	47
3.4	SUMMARY.....	51
4.0	HIGH-SENSITIVITY SURFACE PLASMON RESONANCE SPECTROSCOPY BASED ON A METAL NANOSLIT ARRAYS.....	52
4.1	INTRODUCTION.....	52
4.2	FABRICATION AND CHARACTERIZATION.....	56
4.2.1	Fabrication of the nanoslit arrays .....	56
4.2.2	Characterization .....	56
4.3	RESULTS AND DISCUSSION.....	58
4.4	SUMMARY.....	67
5.0	BLUE-SHIFT OF SURFACE PLASMON RESONANCE IN A METAL NANOSLIT ARRAY STRUCTURE .....	68
5.1	INTRODUCTION.....	68
5.2	CAVITY RESONANCE OF SURFACE PLASMONS IN METAL NANOSLIT ARRAYS .....	72
5.3	MODELING OF SURFACE-PLASMON DISPERSION AND RESONANCE ..	80
5.4	CHARACTERIZATION OF DISPERSION-INDUCED BLUE-SHIFT OF SURFACE-PLASMON RESONANCE.....	87
5.5	SUMMARY.....	90
6.0	NEAR- TO FAR-FIELD IMAGING OF FREE-SPACE AND SURFACE-BOUND WAVES EMANATING FROM A METAL NANOSLIT .....	91
6.1	INTRODUCTION.....	91
6.2	FABRICATION AND CHARACTERIZATION.....	93
6.2.1	Fabrication of single nanoslits using a focused-ion-beam etching technique .....	93

6.2.2	Measurement setup.....	93
6.2.3	Characterization .....	102
6.3	RESULTS AND DISCUSSION.....	109
6.4	SUMMARY.....	115
7.0	NEAR- TO FAR-FIELD IMAGING OF PHASE EVOLUTION OF LIGHT EMANATING FROM A METAL NANOSLIT .....	116
7.1	INTRODUCTION.....	116
7.2	FABRICATION AND CHARACTERIZATION.....	117
7.2.1	Fabrication of single nanoslit using a focused-ion-beam etching technique .....	117
7.2.2	Measurement setup.....	118
7.2.3	Characterization .....	122
7.3	RESULTS AND DISCUSSION.....	125
7.4	SUMMARY.....	134
8.0	NEGATIVE REFRACTION OF LIGHT WITHOUT NEGATIVE-INDEX MEDIA .....	135
8.1	INTRODUCTION.....	135
8.2	DIFFRACTIVE TRANSMISSION AND INTERFERENCE THROUGH AN ARRAY OF VERTICAL NANOSLITS.....	136
8.2.1	Fabrication of vertical and horizontal nanoslit arrays.....	136
8.2.2	Measurement setup.....	138
8.3	THEORY AND CHARACTERIZATION.....	140
8.4	SUMMARY.....	147
9.0	CONCLUSION.....	148
	REFERENCES.....	152
	JOURNAL PAPERS PUBLISHED.....	160

## LIST OF FIGURES

Figure 1.1 Dielectric function of silver in the optical range.....	8
Figure 1.2 Surface plasmon waves on metal surface and the dispersion relations.....	14
Figure 1.3 The calculated SPs propagation length of Ag/air and Ag/quartz interface .....	15
Figure 1.4 Grating coupling between light and SPs .....	16
Figure 2.1 SEM image of a silver 1D grating structure with subwavelength slits formed on a quartz substrate using holographic lithography and electron beam lithography, and angled metal deposition.....	22
Figure 2.2 Schematic process flow forming 1D thick metallic gratings with narrow slits.....	23
Figure 2.3 Schematic drawing of angled-deposition of metal on quartz mesa surface with thermal evaporation.....	24
Figure 2.4 SEM image of a 100-nm-wide slit arrays formed in a 140-nm-thick Ag layer using FIB etching technique.....	25
Figure 2.5 Schematic of process flow forming 1D metallic slit arrays using FIB etching technique.....	26
Figure 2.6 Set-up for optical characterization of Ag subwavelength gratings with narrow slits .	33
Figure 2.7 Transmission spectra of a 1D slit array sample with grating period of 370 nm and with 120 nm or 200 nm thick Ag.....	34
Figure 2.8 Transmission and reflection measured as a function of incidence angle at the wavelength of 633 nm (TM polarized).....	35
Figure 2.9 SEM images of 1 ~ 10 slit arrays formed on a quartz substrate using an electron beam lithography technique and angled metal deposition .....	37
Figure 2.10 The measured transmission spectra through the slits as a function of slits number..	38

Figure 3.1 SEM micrographs of a silver nanoslit array structure formed on a mesa-etched quartz substrate: the effects of annealing on the morphology of metal.....	42
Figure 3.2 Transmission spectra of a silver nanoslit array structure .....	43
Figure 3.3 Surface plasmon band structure calculated for a 1D silver nanoslit array structure with grating period of 400 nm. ....	50
Figure 4.1 Schematic drawing of the fabricated Ag nanoslit array structure (after adsorption of a SAM). ....	54
Figure 4.2 Optical transmission through a Ag nanoslit array: before chemical modification of metal surface and after adsorption of an alkanethiol self-assembled monolayer .....	55
Figure 4.3 Surface plasmon polarization charge distribution on a silver nanoslit array calculated with the finite-difference time-domain analysis at 650 nm wavelength .....	64
Figure 4.4 SP effective index $n_e$ in a silver nanoslit with air gap and $E_x$ field distribution calculated for a Ag slit at 650 nm wavelength .....	65
Figure 4.5 Sensitivity calculated at 680 nm wavelength for different slit width of a silver nanoslit array .....	66
Figure 5.1 A side view of two nanoslits in a metal film on a quartz ( $\text{SiO}_2$ ) substrate.....	71
Figure 5.2 SEM images of three different slit arrays that were fabricated by focused-ion beam etching and a schematic diagram for the method used to measure the transmission spectra.....	77
Figure 5.3 Transmission spectra of Ag nanoslit arrays (the number of slits: 1, 2, 3, 5 and 10)...	78
Figure 5.4 The charge distribution for a resonant surface plasmon polarization, as calculated by FDTD for a 2-slit structure .....	79
Figure 5.5 The calculated wavelength dependence of the SP propagation constant ( $\beta$ ) for various different interfaces.....	85
Figure 5.6 The calculated wavelength dependence of the SP propagation constant ( $\beta$ ) is shown for Au/Si/SiO <sub>2</sub> interfaces .....	86
Figure 5.7 Experimental transmission spectra of Ag or Au nanoslit arrays (before and after chemical modification of metal surface: adsorption of a SAM layer).....	89
Figure 6.1 SEM image of a 100-nm-wide slit formed in a 140-nm-thick Ag layer deposited on a fused silica substrate using a focused-ion-beam etching technique .....	95

Figure 6.2 Schematic process flow of a single nanoslit formed in Ag layer .....	96
Figure 6.3 Schematic of an optical transmission measurement setup using a scanning probe technique.....	97
Figure 6.4 The angular dependence of transmission of a nanoapertured fiber probe.....	98
Figure 6.5 The measurement scanned across a single nanoslit with the nanoprobe aligned perpendicular to the substrate surface .....	99
Figure 6.6 The measurement scanned across a single nanoslit with the 45° tilted probe axis ...	100
Figure 6.7 Linearly scanned along the radial direction in the near- to far-field region with the probe axis tilted parallel to the scan direction .....	101
Figure 6.8 The incidence-angle dependence of the nanoapertured probe transmission .....	105
Figure 6.9 Silver nanoslit radiation profiles scanned along the direction perpendicular to the probe axis.....	106
Figure 6.10 Silver nanoslit radiation profiles scanned across a single nanoslit with the 45° tilted probe axis.....	107
Figure 6.11 Radiation pattern of a silver nanoslit obtained with the probe linearly scanned along the radial direction.....	108
Figure 6.12 FDTD simulation of nanoslit radiation .....	113
Figure 6.13 The radiation intensity plotted as a function of angle for different radial distances: radial distance of 0.65, 1.30, 2.60, 5.20 $\mu\text{m}$ .....	114
Figure 7.1 SEM image of a 80-nm-wide slit formed in a 50-nm-thick Ag layer deposited on a fused silica substrate. A focused-ion-beam etching technique was employed to form the nanoslit structure.....	119
Figure 7.2 Schematic of an optical transmission measurement setup using a scanning probe technique.....	120
Figure 7.3 Schematic drawing of the measurement setup .....	121
Figure 7.4 Scan profiles of the interference pattern of slit-transmitted and direct film-transmitted waves.....	123
Figure 7.5. Near- to far-field imaging of optical wavefronts emanating from a nanoslit formed in a thin Ag film.....	124

Figure 7.6 Interference of slit-transmitted and direct, film-transmitted waves .....	126
Figure 7.7 Comparison between the measured scan profiles and FDTD simulation result.....	132
Figure 7.8 FDTD simulation of phase relationship of slit-transmission and direct film-transmission .....	133
Figure 8.1 SEM image of the vertical and horizontal nanoaperture arrays fabricated using a focused-ion-beam etching technique .....	137
Figure 8.2 Schematic drawing of the measurement setup .....	139
Figure 8.3 FDTD simulation of radiation patterns of three different structures of a single nanoslit formed on a Ag layer .....	142
Figure 8.4 Radiation pattern of a single vertical nanoslit calculated by finite-difference time-domain analysis .....	143
Figure 8.5 Negative refraction of light through a metal film with an array of vertical and horizontal dipole apertures .....	144
Figure 8.6 Schematic drawing of the vertical dipole arrays .....	145
Figure 8.7 Negative refraction angle measured as a function of incident angle.....	146

## PREFACE

This thesis would not have been possible without the generous support, helpful guidance and good wishes from many people. First and foremost, I would like to express my eternal appreciation to my advisor, Dr. Hong Koo Kim. It has been an honor and privilege for me to work with such a talented and pleasant scholar. I am immensely grateful to him for his thoughtful guidance, encouragement, and inspiration throughout my doctoral program. Also I express a sincere gratitude to the members of my dissertation committee, Drs. Joel Falk, William Stanchina, Minhee Yun and Rob Coalson, for their taking time to serve on my committee and giving me invaluable comments and suggestions on this dissertation. I would like to thank my colleagues, Jeff Wuenschell and Yonggang Xi for their FDTD simulation support in this work. Zhijun Sun – Dr. Kim's former doctoral student - also deserves recognition since his thesis provides helpful references to this study.

I would like to thank my wife, Donghee Sinn, for her unfailing love and support in this long journey. She has held me up whenever I encountered frustration and disappointment with myself during my doctoral years. I also thank my lovely son, Tyler (Junwoo) Jung. His existence has made me stand up whenever I felt like collapsing, and his smile has given me the strength. Finally, I would like to thank my parents and family for their never-ending love and support. They have provided great guidance in life and have constantly offered the warmest place to go when difficult times.

## **1.0 INTRODUCTION**

### **1.1 OVERVIEW**

Recently, metal nanostructures have received considerable attention for their ability to guide and manipulate light at the nanometer scale, and the pace of making new discoveries and inventions in this area has been accelerating [1]. One of the common interests in optics research has been miniaturization, and the nano-optics field has been rapidly expanding. As in the case of electronics, scaling down the dimensions of photonic devices is expected to bring numerous benefits in terms of speed, capacity, and energy efficiency in information processing. Surface plasmons, collective oscillation of electrons excited by light, are basically photon waves trapped/squeezed at a metal/dielectric interface [2]. Their reduced size in electromagnetic field distribution offers a potential for nanoscale reduction of photonic devices. The intrinsic coupling between electrons and photons also offers a potential for merging electronics and photonics on the same platform.

Plasmonics forms a major part of the fascinating field of nanophotonics, which explores how electromagnetic (EM) fields can be confined over dimensions on the order of or smaller than the wavelength of light [3]. It is based on interaction processes between electromagnetic radiation and conduction electrons at metallic interfaces or in small metallic nanostructures. Electromagnetic (EM) waves in the form of surface plasmons break some of the rules of classical

optics. Classical optics predicts that light cannot propagate through an aperture much smaller than about half the wavelength – the best it can do is “tunnel” through, which tends to result in weak transmission when the aperture is reasonably long. Experimentally, it has been reported that the wavelength dependence is significantly different than predicted by classical theory. In the case of one-dimensional (1D) slit arrays, near 100% transmission of TM-polarized light has been predicted through a subwavelength aperture array [4].

Near-field optics has progressed rapidly in elucidating the science and technology of such fields. Exploiting an essential feature of optical near fields, i.e. the resonant interaction between electromagnetic fields and matter in nanoscale regions, important applications and new directions such as studies in near-field imaging, spatially resolved spectroscopy, nano-fabrication, nano-photonics devices, ultrahigh-density optical memory, and atom/particle manipulation have been realized and significant progress has been reported [5].

In this thesis, we have designed, fabricated and investigated the plasmonic phenomena occurring in various metallic nano-structures (especially with Ag and Au). Experimentally and theoretically, we have studied their optical properties in the near- to far-fields. Finite-difference time-domain (FDTD) simulations were also performed for numerical analysis of electromagnetic (EM) field distribution. This thesis is structured as follows. Fundamental properties on light interaction with bulk metallic materials are briefly reviewed in Chapter 1. It will be shown in later chapters the optical properties of nano-metallic structures are related to the bulk properties in certain aspects. Chapter 2 describes optical transmission through narrow slit arrays. In Chapter 3, we have investigated the effects of thermal annealing of metal nanoslits on the surface plasmon resonance characteristics of the slit arrays. A transmission SPR sensor based on a metal nanoslit array structure is described in Chapter 4. Chapter 5 describes our observation of blue-

shift of optical transmission spectra and develops a model that explains the spectral shift is caused by the interplay of anomalous dispersion and quadrupolar resonance of surface plasmons in the cavity structure of the slit array. In Chapter 6, we report the radiation pattern (radial and angular distribution of light intensity) of a thick (140 nm thick) Ag nanoslit that was measured in the near- to far-fields by linearly scanning a nanoapertured probe along the radial direction with the probe axis tilted parallel to the scan direction. Also, we report near- to far-field measurement of optical wavefronts emanating from a nanoslit formed in a thin (50 nm thick) Ag film in Chapter 7. Negative refraction of visible light without negative-index media is studied in Chapter 8. Finally, in Chapter 9, we summarize and conclude.

## **1.2 DIELECTRIC CONSTANT OF METALS [6,7]**

Optical response of matter is basically determined by internal electronic processes that involve an interaction with optical fields consistent with both electronic and electromagnetic boundary conditions [8]. The resulting scattered fields reflect the properties of these internal processes in the illuminated objects, especially when they are observed in the near field regime. The scattered fields exhibit an asymptotic behavior in the far-field limit since propagating optical waves carry electromagnetic energy out of the object with a retarded nature. In this case, the optical response of matter can be represented in macroscopic quantities, such as dielectric functions, which enable us to reproduce the macroscopic electromagnetic boundary conditions correctly.

There are two sets of quantities that are commonly used to describe optical properties: the real and imaginary parts of the complex refractive index  $N = n + ik$  and the real and imaginary

parts of the complex dielectric function (or relative permittivity)  $\varepsilon = \varepsilon' + i\varepsilon''$ . These two sets of quantities are not independent. The relations between the two are expressed in the later part of this section (Equation (1.9) and (1.10)). In the classical theory of optical properties, electrons and ions of matter are treated as simple harmonic oscillators (i.e. spring) subject to the driving force of applied electromagnetic fields. In this model, the equation of motion of such an oscillator (with mass  $m$  and charge  $e$ ) driven by optical electric field (assume the matter is non-magnetic) can be described as follow [7]:

$$m\ddot{\bar{x}} + b\dot{\bar{x}} + K\bar{x} = e\bar{E} \quad (1.1)$$

where  $\bar{E}$  is the applied optical electric field,  $K$  is the spring constant,  $\bar{x}$  is the displacement from equilibrium and  $b$  is the damping constant. In Drude theory [9], a free electron is considered as an oscillator and a restoring force  $K\bar{x}$  can be neglected. Then, Equation (1.1) is simplified as follow:

$$m\ddot{\bar{x}} + b\dot{\bar{x}} = e\bar{E} \quad (1.2)$$

Taking the electric field to be time harmonic with frequency  $\omega$  and neglecting the transient response of electrons to the field, Equation (1.2) results in a polarization (dipole moment per unit volume)

$$\bar{P} = -\frac{\omega_p^2}{\omega^2 + i\gamma\omega} \varepsilon_0 \bar{E} \quad (1.3)$$

where  $\gamma = b/m$ , plasma frequency  $\omega_p^2 = Ne^2/m\varepsilon_0$ ,  $N$  is the number of oscillators per unit volume, and  $\varepsilon_0$  is the dielectric constant in vacuum. Equation (1.3) is a particular example of the constitutive relation  $\vec{P} = \varepsilon_0\chi\vec{E}$ . Considering the polarization and applied field for  $\vec{D} = \varepsilon\varepsilon_0\vec{E}$  in Maxwell's equations, then, the dielectric function is

$$\varepsilon = 1 + \chi = 1 - \frac{\omega_p^2}{\omega^2 + i\gamma\omega} \quad (1.4)$$

with real and imaginary parts

$$\varepsilon' = 1 + \chi' = 1 - \frac{\omega_p^2}{\omega^2 + \gamma^2} \quad (1.5)$$

$$\varepsilon'' = \chi'' = \frac{\omega_p^2\gamma}{\omega(\omega^2 + \gamma^2)} \quad (1.6)$$

where  $\chi$  is electric susceptibility.

Excitation of a plasma oscillation is the creation of a plasmon with energy  $\hbar\omega_p$  and lifetime  $\tau = 2/\gamma$ . The damping constant is related to the average time  $\tau$  between collisions by  $\gamma = 1/\tau$ . Collision times are usually determined by interaction of the electrons with lattice vibrations: electron-phonon scattering at ordinary temperatures. For most metals,  $\gamma$  is much less than  $\omega_p$  at room temperature. Plasma frequencies of metals are in the visible and ultraviolet

(UV),  $\hbar\omega_p$  ranges from 3 to 20 eV. Therefore, when  $\omega \gg \gamma$ , a good approximation to the Drude dielectric functions at visible and UV frequencies is

$$\varepsilon' \approx 1 - \frac{\omega_p^2}{\omega^2} \quad (1.7)$$

$$\varepsilon'' \approx \frac{\omega_p^2 \gamma}{\omega^3} \quad (1.8)$$

Although Drude theory is suitable to some metals such as aluminum, it does not accurately describe the optical characteristics of many other metals including silver. Silver, possessing a substantial bound-electron component, appreciably alters the free-electron optical properties. Thus, the dielectric function can be modified as  $\varepsilon = \varepsilon_f + \delta\varepsilon_b$  that includes a contribution  $\delta\varepsilon_b$  from Lorentz's model and a free-electron contribution  $\varepsilon_f$ .

The real and imaginary parts of the complex refractive index  $N = n + ik$  and the real and imaginary parts of the complex dielectric function  $\varepsilon = \varepsilon' + i\varepsilon''$  are often used to describe the optical properties of absorbing media [7]. Since  $\varepsilon = \varepsilon' + i\varepsilon'' = \tilde{N}^2$ , then

$$\varepsilon' = n^2 - k^2, \quad \varepsilon'' = 2nk \quad (1.9)$$

or

$$n = \sqrt{\frac{\sqrt{\varepsilon'^2 + \varepsilon''^2} + \varepsilon'}{2}}, \quad k = \sqrt{\frac{\sqrt{\varepsilon'^2 + \varepsilon''^2} - \varepsilon'}{2}} \quad (1.10)$$

Silver is a favored material for this study because of its high conductivity, relatively small imaginary part dielectric constant  $\varepsilon''$  for lower attenuation and the deep UV bulk plasma frequency ( $\lambda_p \approx 325$  nm) away from visible range. Figure 1.1 shows experimentally obtained optical constants of silver [10].

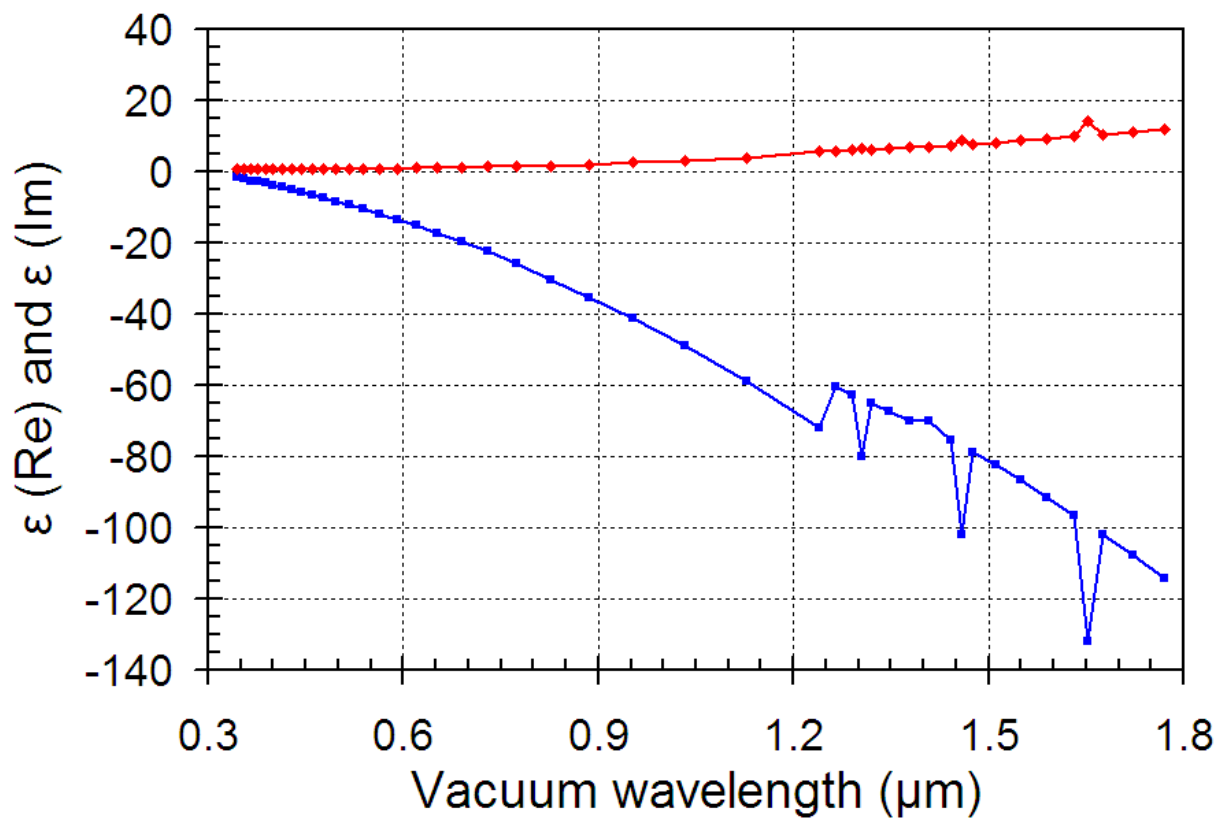


**Figure 1.1** Dielectric function of silver in the optical range. The real (blue) and imaginary (red) parts of the complex dielectric function. The experimental data from Reference [10].

### 1.3 SURFACE PLASMONS AT METAL SURFACES [2,6]

Coherent fluctuations of electron density on a metal surface are called the surface plasma oscillations. An electron density wave is accompanied by electromagnetic fields. The EM field sharply attenuates in the transverse direction, and the wave longitudinally propagates along the metal surface. Traditionally, surface plasmons are studied in two approaches: on the electronic excitation base [11] and on the electromagnetic field and wave base [2]. The first approach is rather complicated because of the difficulty in analyzing the macroscopic experimental results in a quantitative way. Thus, the EM approach is preferred to study optical properties of surface plasmons, and it seems to be effective in interpreting phenomena and performing experiment design.

Figure 1.2(a) shows the charge and the electromagnetic field of SPs at a metal/dielectric interface in  $x$  direction. The field is strongly localized at the interface and it is described by [2]

$$E = E_0^\pm \exp[+i(k_x x \pm k_z z - \omega t)] \quad (1.11)$$

with  $+$  for  $z \geq 0$ ,  $-$  for  $z \leq 0$ , and with imaginary  $k_z$ , which causes the exponential decay of the field  $E_z$ . The wave vector  $k_x = 2\pi/\lambda_p$  lies parallel to the  $x$  direction, where  $\lambda_p$  is the wavelength of the plasma oscillation. Maxwell's equations yield the retarded dispersion relation for the plane surface of a semi-infinite metal with the dielectric function  $(\varepsilon_1 = \varepsilon_1' + i\varepsilon_1'')$ , adjacent to a medium  $\varepsilon_2$  as a dielectric media:

$$D_0 = \frac{k_{z1}}{\varepsilon_1} + \frac{k_{z2}}{\varepsilon_2} = 0 \text{ together with} \quad (1.12)$$

$$\varepsilon_i \left( \frac{\omega}{c} \right)^2 = k_x^2 + k_{zi}^2 \text{ or } k_{zi} = \left[ \varepsilon_i \left( \frac{\omega}{c} \right)^2 - k_x^2 \right]^{1/2}, \quad i=1,2 \quad (1.13)$$

The wave vector  $k_x$  is continuous through the interface. Then, the dispersion relation (Equation (1.13)) can be written as

$$k_x = \frac{\omega}{c} \left( \frac{\varepsilon_1 \varepsilon_2}{\varepsilon_1 + \varepsilon_2} \right)^{1/2} \quad (1.14)$$

If we assume besides a real  $\omega$  and  $\varepsilon_2$  that  $\varepsilon_1'' < |\varepsilon_1'|$ , we obtain a complex  $k_x = k'_x + ik''_x$  with

$$k'_x = \frac{\omega}{c} \left( \frac{\varepsilon_1' \varepsilon_2}{\varepsilon_1' + \varepsilon_2} \right)^{1/2} \quad (1.15)$$

$$k''_x = \frac{\omega}{c} \left( \frac{\varepsilon_1' \varepsilon_2}{\varepsilon_1' + \varepsilon_2} \right)^{3/2} \frac{\varepsilon_1''}{2(\varepsilon_1')^2} \quad (1.16)$$

For real  $k'_x$ , one needs  $\varepsilon_1' < 0$  and  $|\varepsilon_1'| > \varepsilon_2$ , which can be fulfilled in a metal and also in a doped semiconductor near the eigen frequency;  $k''_x$  determines the internal absorption. The dispersion relation, shown in Figure 1.2(b), approaches the light line  $\sqrt{\varepsilon_2} \omega / c$  at small  $k_x$ , but remains

larger than  $\sqrt{\varepsilon_2} \omega / c$ , so that the SPs cannot transform into light: it is a nonradiative SP. At large  $k_x$  or,  $\varepsilon'_1 \rightarrow -\varepsilon_2$  the value of  $\omega$  approaches

$$\omega_{sp} = \sqrt{\frac{\omega_p}{1 + \varepsilon_2}} \quad (1.17)$$

where  $\omega_p$  is the plasma frequency  $\sqrt{4\pi N e^2 / m}$ , with  $N$  the bulk electron density for a free electron gas. With increasing  $\varepsilon_2$ , the value of  $\omega_{sp}$  is reduced. At large  $k_x$  the group velocity goes to zero as well as the phase velocity, so that the SP resembles a localized fluctuation of the electron plasma.

The field amplitude of the SPs decreases exponentially as  $\exp(-|k_{zi}| |z|)$ , normal to the surface. The value of the skin depth at which the field falls to  $1/e$ , becomes

$$\hat{z} = \frac{1}{|k_{zi}|} \text{ or} \quad (1.18)$$

$$\hat{z}_1 = \frac{\lambda_0}{2\pi} \left( \frac{\varepsilon'_1 + \varepsilon_2}{\varepsilon_1'^2} \right) \text{ in the medium with } \varepsilon_1$$

$$\hat{z}_2 = \frac{\lambda_0}{2\pi} \left( \frac{\varepsilon'_1 + \varepsilon_2}{\varepsilon_2^2} \right) \text{ in the medium with } \varepsilon_2 \quad (1.19)$$

The intensity of SPs propagating along a smooth surface decreases as  $e^{-2k_x''x}$  ( $k_x''$  is expressed in Equation (1.16)). The length  $L_i$  after which the intensity decreases to  $1/e$  is given by

$$L_i = (2k_x'')^{-1} \quad (1.20)$$

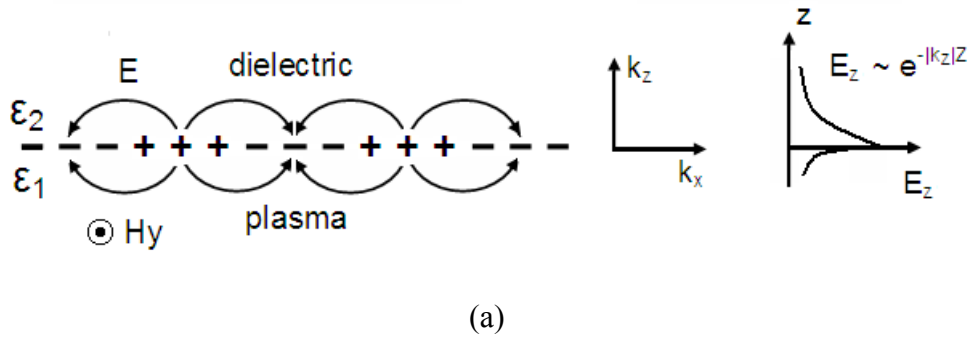
The calculated SPs propagation length of Ag/air and Ag/quartz interface is shown in Figure 1.3.

As shown in Figure 1.2 (b), the dispersion relation of SPs lies in the right side of the light ( $k_x > \omega/c$ ). In order to “transform” the photons into SPs, the wave vector  $\hbar\omega/c$  of a given photon energy  $\hbar\omega$  has to be increased by a  $\Delta k_x$  value. There are two methods for optical excitation of SPs: (1) grating coupler, and (2) attenuated total reflection (ATR) coupler [2]. Here, the grating coupler is our interest in science and technology point of view. If light ( $k = \omega/c$ ) incidents a grating with a grating constant  $d_g$ , at an angle  $\theta_0$  its component in the surface can have wave vectors  $(\omega/c)\sin\theta_0 \pm m \cdot k_g$  with  $m$  an integer and  $k_g = 2\pi/d_g$ . The dispersion relation, Equation (1.14), can then be satisfied by the sum

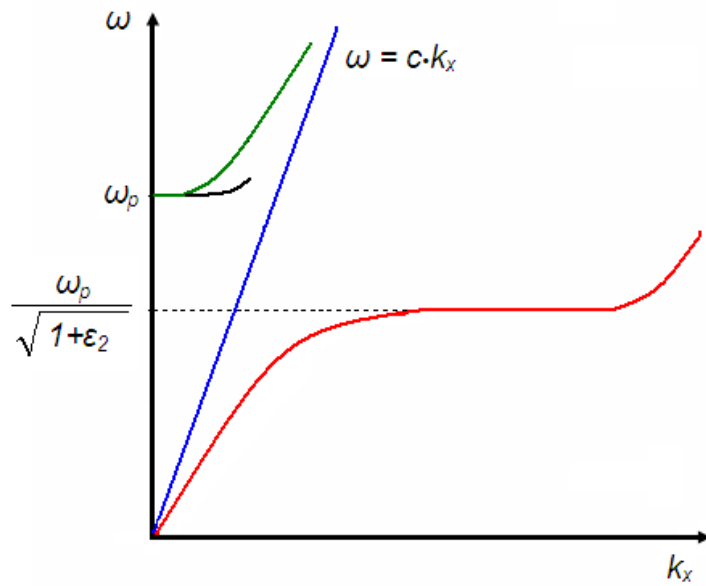
$$k_x = \frac{\omega}{c} \sqrt{\frac{\varepsilon}{\varepsilon+1}} = \frac{\omega}{c} \sin\theta_0 \pm m \cdot k_g = \frac{\omega}{c} \sin\theta_0 \pm \Delta k_x = k_{sp} \quad (1.21)$$

where  $\Delta k_x = m \cdot k_g$  stems from any perturbation in the smooth surface;  $\Delta k_x = 0$  gives no solution of the dispersion relation Equation (1.14).

The reverse takes place too. SPs propagating along a grating or a rough surface can reduce their wave vector  $k_x$  by  $\Delta k_x$  so that the SP is transformed into light, arrow 4  $\rightarrow$  5 in Figure 1.4. This consequence of the photon-SP coupling via roughness (the light emission) plays an important role. Surface plasmons also exist on curved surfaces (e.g., on spheres or cylinders) [2]. In that case, the SPs are coupled and scattered by  $\Delta k_x$  resulting from the curvature. Since the resonant collective oscillation of the conduction electrons is limited to the small object, it is often called a localized plasmon. And the fields are enhanced at the curved surface. Resonance of localized surface plasmon around small cylinders will be discussed in more detail in Chapter 2 as one of the main features of the transmission spectra.



(a)



(b)

**Figure 1.2** Surface plasmon waves on metal surface and the dispersion relations. (a) Schematic illustration of the charges and the electromagnetic field of SPs propagating on a surface in the  $x$  direction. The exponential dependence of the field  $E_z$  is seen on the right.  $H_y$  shows the magnetic field in the  $y$  direction of this p-polarized wave. (b) The dispersion relation of nonradiative SPs (red), right of the light line (blue)  $\omega = c \cdot k_x$ , on a metal surface coated with a dielectric film ( $\epsilon_2$ ). Radiative SPs (black), left of the light line, starts at  $\omega_p$ . The green line, left of the light line (blue), represents the dispersion of light in a metal:  $\omega/k_x = c/|\epsilon_1'|^{1/2}$  or in the case of free electrons  $\omega^2 = \omega_p^2 + c^2 k_x^2$ . From Reference [2].

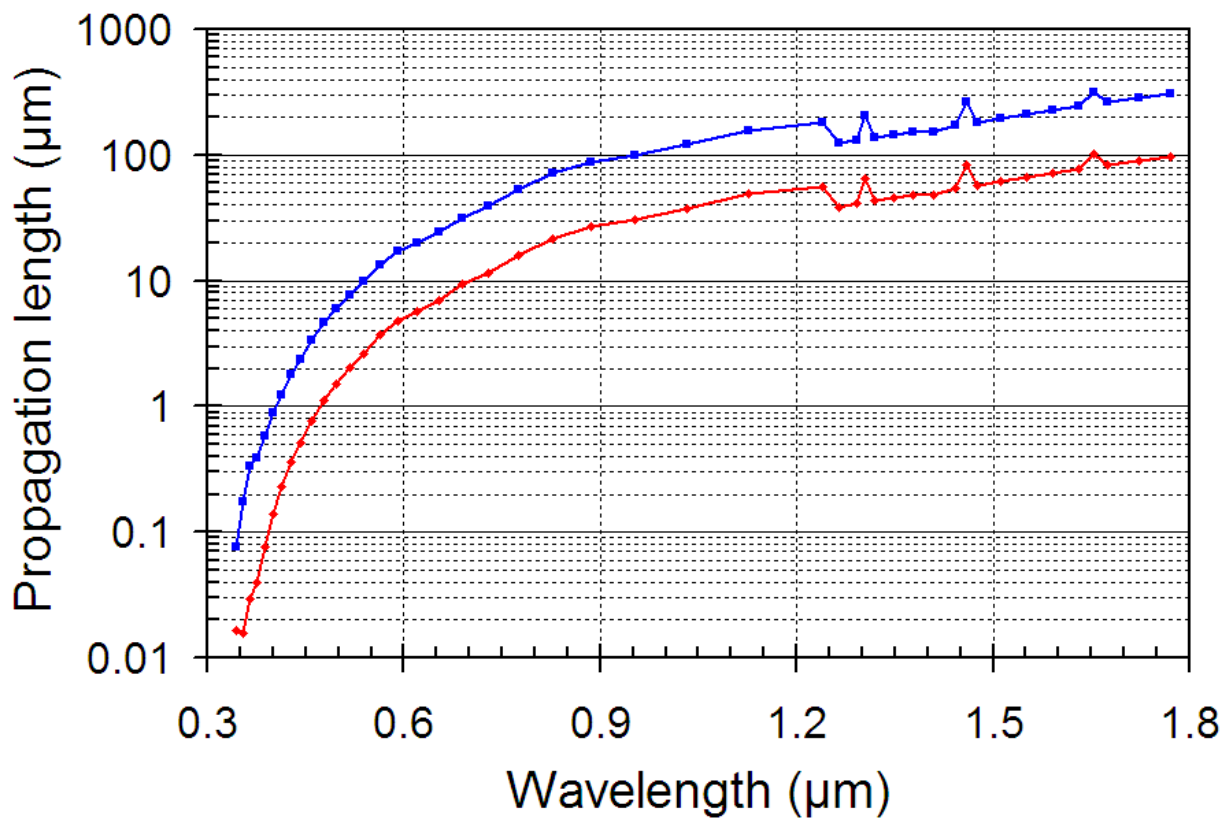


**Figure 1.3** The calculated SPs propagation length of Ag/air (blue) and Ag/quartz (red) interface.  $\epsilon(\text{air}) = 1$  and  $\epsilon(\text{quartz}) = 2.1316$ . Calculated using data from Reference [10].

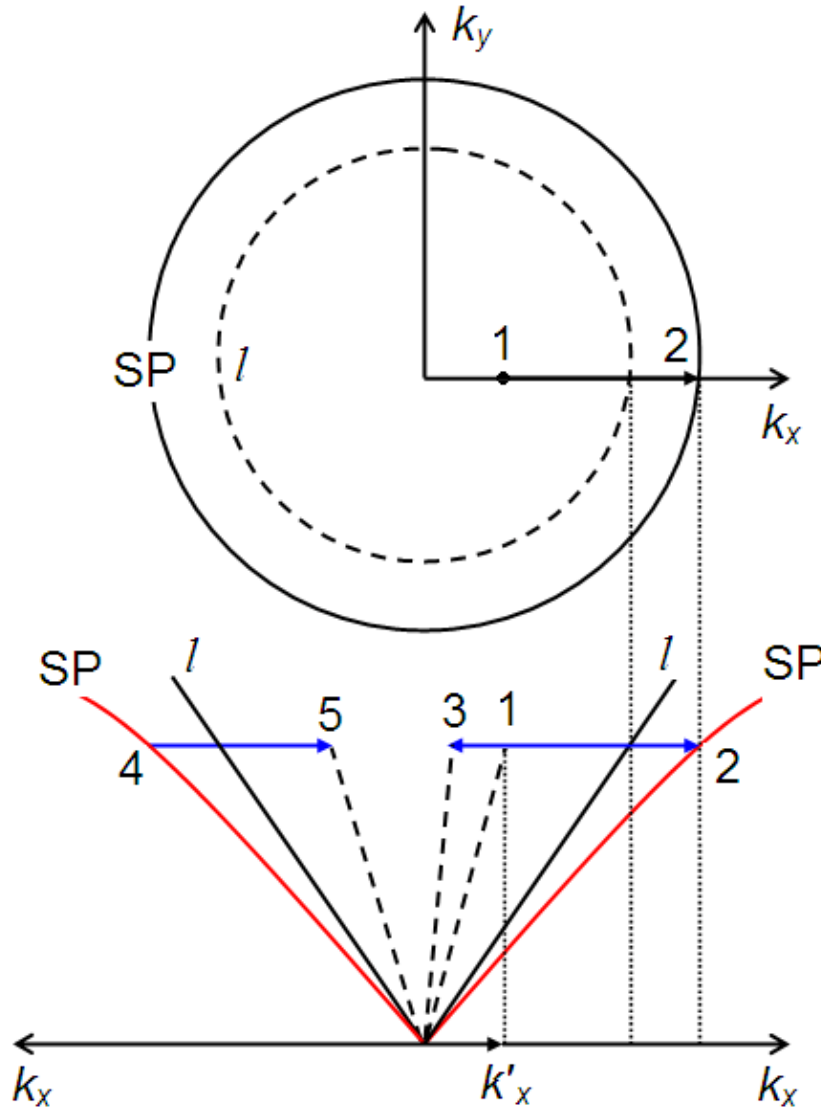


**Figure 1.4** Grating coupling between light and SPs. SP: dispersion relation of SPs,  $l$ : light line. The incoming light, wave vector  $k'_x$ , point (1) is transformed into a SP, point (2), by taking up  $\Delta k_x$ . The interaction  $1 \rightarrow 3$  via roughness leads to light scattered inside the light cone. The process  $4 \rightarrow 5$  describes the decay of a SP into light via  $\Delta k_x$ ; it is the reverse of  $1 \rightarrow 2$ . Upper part: the full circle represents the values of  $|k| = \sqrt{k_x^2 + k_y^2}$  and the light circle (dashed circle) at  $\omega = \text{const.}$  in the two-dimensional space. From Reference [2].

## 1.4 SUMMARY

Physical phenomena occurring in metallic nanostructures offer an interesting potential in that they may allow us to overcome the limits of diffractive optics and to develop new functional devices complementing the dielectric-based conventional optics. Optical excitation of metal usually results in electron charge density oscillation. Due to the strong attenuation of light inside metals, surface plasmons (SPs) are the main feature of metal optics. The spatial extension of SP fields is governed by the size of the nanostructure and can be made much smaller than the wavelength of light. These features are potentially useful in developing ultracompact photonic chips. Near-field optics has progressed rapidly in elucidating the science and technology of such fields. Exploiting an essential feature of optical near fields, i.e. the resonant interaction between electromagnetic fields and matter in nanometric regions, important applications and new directions such as studies in near-field imaging, spatially resolved spectroscopy, nano-fabrication, nano-photonic devices, ultrahigh-density optical memory, and atom/particle manipulation have been realized and significant progress has been reported.

## 2.0 TRANSMISSION OF LIGHT THROUGH METALLIC NANOSLIT ARRAYS

### 2.1 INTRODUCTION

Optical interaction in nano-apertured metal layers has been gaining increasing attention from science and applications aspects since the experimental observation of an extraordinary transmission of light through a two dimensional (2D) array of holes formed in metallic films [12-17]. In exploring mechanisms for such an extraordinary transmission, thick transmission metallic gratings with very narrow slits are mostly studied with simulations and analytical models [18-23]. In the case of one-dimensional (1D) slit arrays, near 100% transmission of TM-polarized light has been predicted through a subwavelength aperture array [20]. Mechanisms of the optical transmission through slit arrays, however, are not clearly understood and have been a subject of debate. While some features of the transmission characteristics of 1D slit arrays can be deduced from the 2D characteristics, 1D slit arrays clearly differ from 2D aperture arrays. For example, propagating modes are supported by a slit structure but not in a hole aperture formed in metal, and this is considered one of the key factors that differentiate their transmission properties. The mechanism proposed in the earlier work with 1D slit arrays is that light transfers from the upper surface to the lower one by the excitation of coupled surface plasmons (SPs) on both surfaces of the metallic grating or by the coupling of incident waves with waveguide resonances located in the slits [20]. Later, Cao and Lalanne have argued that SPs are most

strongly excited near the Wood–Rayleigh anomalies and are most weakly excited at the transmission maxima [22]. They also argued that SPs play a negative role in the transmission anomalies in slit arrays and that the transmission enhancement is due to a combination of strongly excited waveguide and diffraction modes in slit arrays. Treacy has recently argued that the transmission anomalies can be explained in terms of a dynamical diffraction theory, in which SPs are an intrinsic component of the diffracted wave fields. It is argued that both propagating and evanescent modes (traditional surface plasmons) of Bloch waves are strongly excited at both the peak and the minimum transmission conditions [19].

While some of the issues in this debate may sound a matter of semantics, it is evident that the role of surface plasmons in optical transmission remains as the key issue. Most of the reported work regarding the 1D slit arrays are theoretical investigations based on numerical analysis, and there has been lack of experimental work that can directly verify the theoretical predictions or guide theoretical study for new mechanisms that may be involved. This might be partly ascribed to the difficulty in forming very narrow, subwavelength slit arrays in metallic films, especially for the visible or shorter wavelength range [24]. Our experimental study of optical transmission/reflection through 1D slit arrays were reported and the results were compared with theoretical analyses of surface plasmon interactions in nanoapertured metal layers [25]. We identified two different types of surface plasmon (SP) resonances involving different sections of metal surfaces: (1) the SP resonance along the planes that comprise either the metal/air or metal/substrate interfaces, and (2) the SP resonance localized along the periphery of each metal island separated by slits. The measurement result also showed that these SP resonances are responsible for the minima observed in the transmission spectra. We have investigated surface plasmon interactions in a metallic nanoslit array structure that shows

characteristic transmission spectra with well-defined transmission minima and maxima in the visible-to-infrared range.

## **2.2 FABRICATION AND CHARACTERIZATION**

### **2.2.1 Holography and E-beam lithography method**

Figure 2.1 shows scanning electron microscopy (SEM) images of the silver 1D grating structure with narrow slits formed on a quartz substrate. First, a holographic lithography and an electron beam lithography (JEOL 9300 at Cornell NanoScale Science and Technology Facility (CNF)) technique were utilized in defining the 1D grating patterns on Cr-coated (30 nm) quartz substrates. A two-step plasma etching process was then performed to transfer the photoresist and/or PMMA resist grating patterns onto the Cr layer and then onto quartz using the Cr layer as an etch mask. The typical etched depth onto quartz was 250 nm ~ 300 nm. 1D arrays of mesa structure with near-vertical sidewalls were formed on quartz with a plasma etching process. Metal (Ag, Al or Au) was angle-deposited on the mesa surface with thermal evaporation. The metal thickness was varied up to 400 nm. The slit width was in the range of 30 ~ 100 nm, and the grating period was down to 200 ~ 300 nm. In this process were able to control the slit width without changing the metal thickness, by adjusting the deposition angle. Figure 2.2 is a schematic process flow of this technique, and the angle deposition of metal is illustrated in Figure 2.3. Direct etching (plasma or wet) of precious metal (Ag and Au) is known to be difficult. The metal patterning method introduced in this work offers a viable alternative in forming very narrow slits in thick metal layers.

### 2.2.2 Focused ion beam etching method

The advantages of holographic and electron beam lithography method (explained previous section) are that it is easy to form large numbers of slit arrays on quartz substrates and the mesa substrates can be used multiple times without any damage of the samples. However, it is not simple to characterize and analysis the optical properties through the metal slit arrays. As shown in Figure 2.1 (b), the as-formed metal slit arrays on the quartz mesa substrate is not a simple geometric shape (i.e., rectangle, circle or ellipse) because the metal is deposited with angled-deposition method to form the clear opening of slit. To solve the problems, we can form metallic 1D slit arrays on quartz substrate using direct etching of metal layer with a focused-ion-beam (FIB) system. Figure 2.4 shows a scanning electron microscope (SEM) image of a 100-nm-wide 5 and 10 slit arrays formed in a 140-nm-thick Ag layer. First, metal layer (Ag, Al or Au) was deposited on the quartz substrate by thermal evaporation. Slit arrays were then formed in the metal layer using a focused-ion-beam etching technique. Seiko SMI-3050-SE dual beam system was used with Ga ion beam. The great advantages of focused-ion-beam etching technique are the as-formed metal slit arrays is a simple geometric shape (i.e., rectangle) and basically, we could form any kind of metal slit arrays (i.e., type of metal, metal thickness, slit width and period of slits) by controlling of etching condition of the system. However, FIB etching technique is suitable to form arrays with only a limited number of slits. Figure 2.5 is a schematic process flow of this technique.

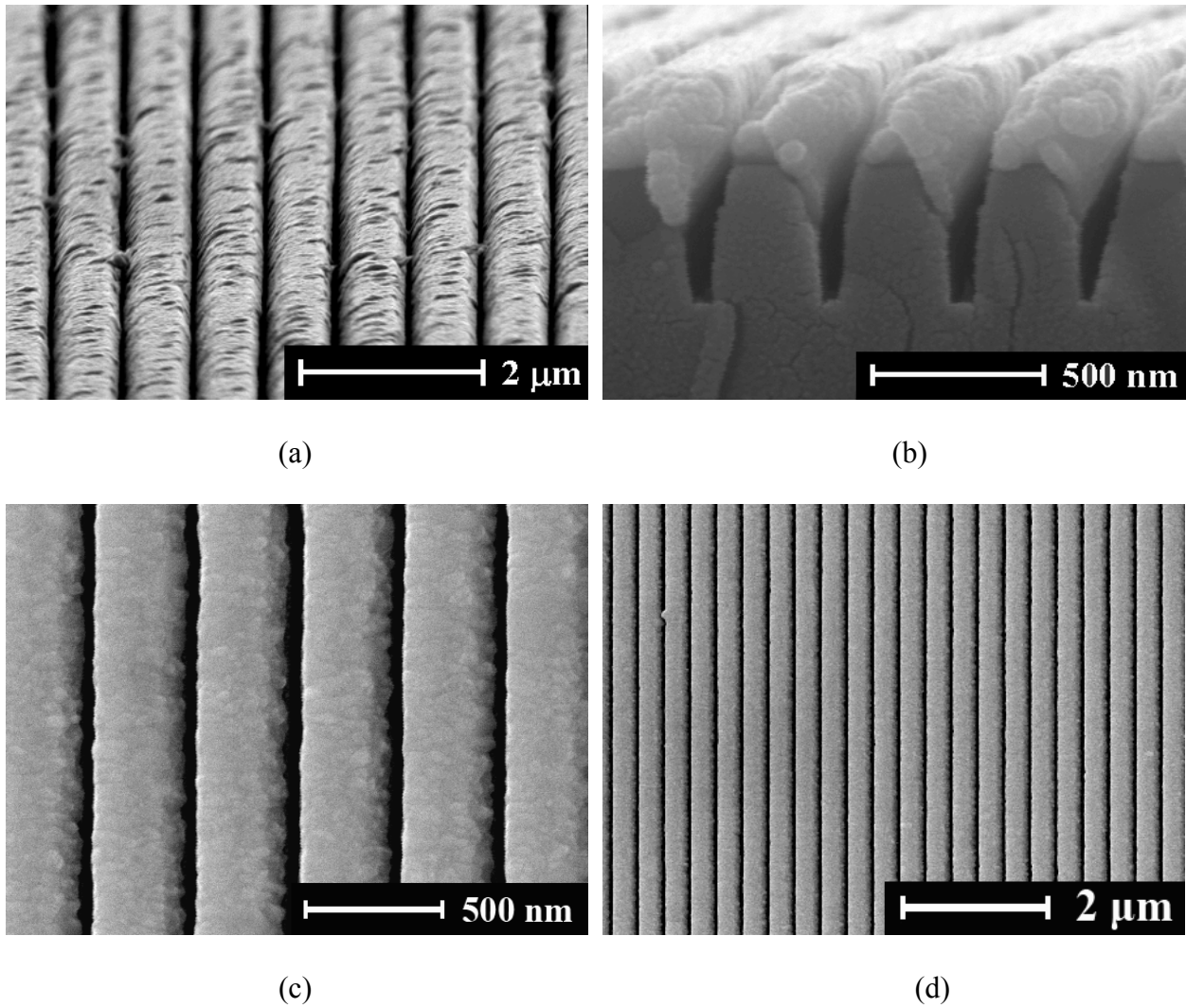


**Figure 2.1** SEM image of a silver 1D grating structure with subwavelength slits formed on a quartz substrate using holographic lithography ((a) and (b)) and electron beam lithography ((c) and (d)), and angled metal deposition. (a) Top view of a Ag 1D slit array with grating period of 780 nm and Ag thickness of 400 nm. (b) Side view of a Ag 1D slit array with grating period of 370 nm and Ag thickness of 250 nm. (c) and (d) Top view of a Ag 1D slit array with grating period of 370 nm and Ag thickness of 250 nm. (c) and (d) Top view of a Ag 1D slit array with grating period of 360 nm and Ag thickness of 140 nm. Opening of slits is clearly revealed with slit width in the range of 30-100 nm along the depth.

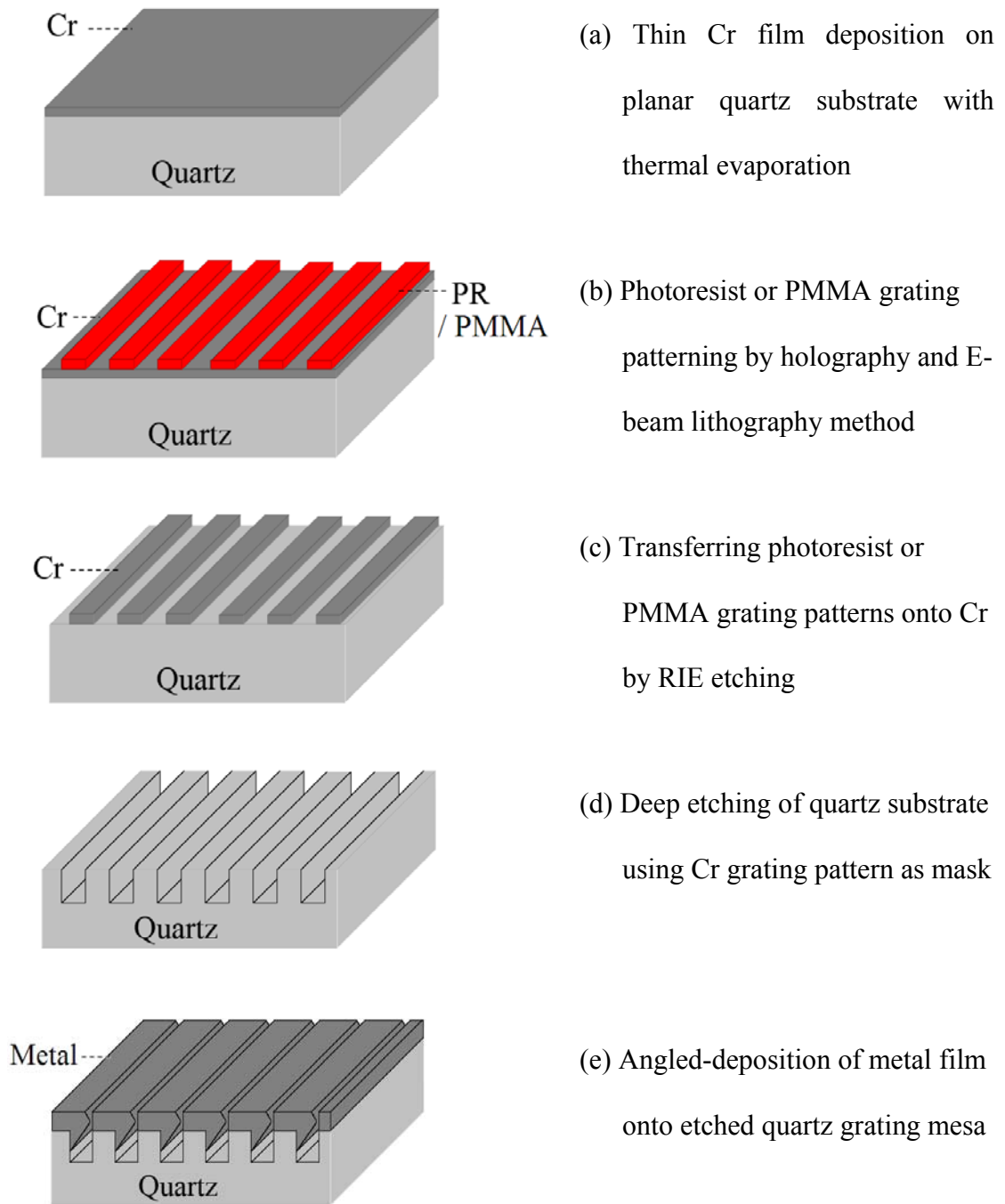


**Figure 2.2** Schematic process flow forming 1D thick metallic gratings with narrow slits. (a)-(b)-(c)-(d)-(e) in sequence.

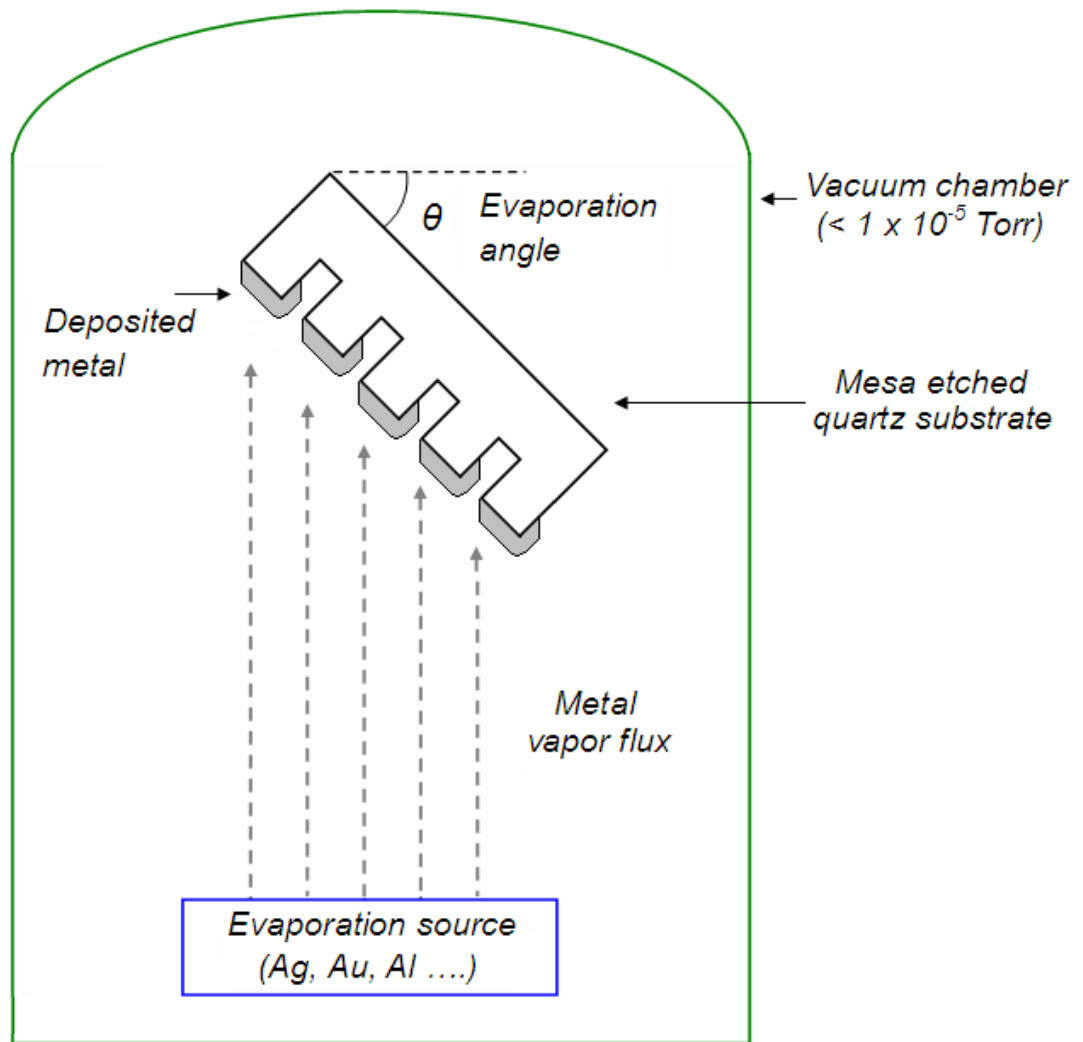
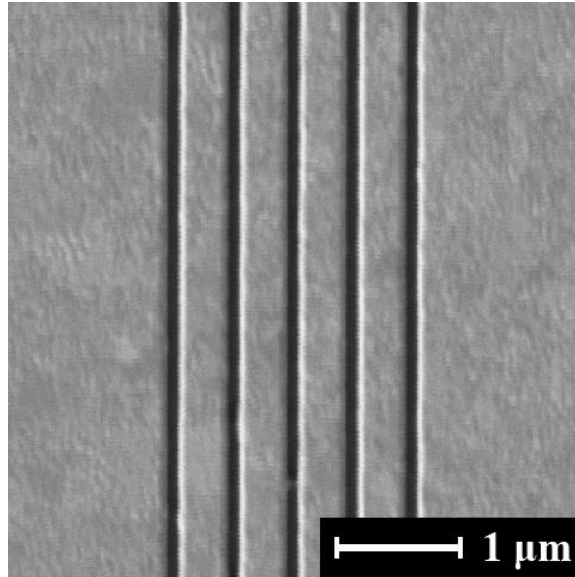
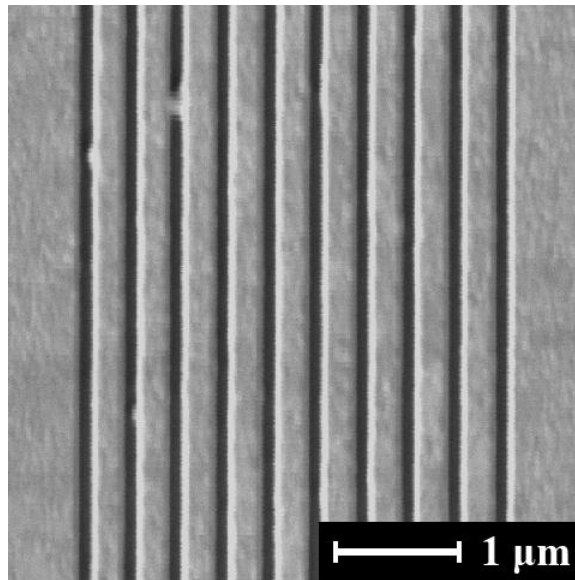


**Figure 2.3** Schematic drawing of angled-deposition of metal on quartz mesa surface with thermal evaporation.

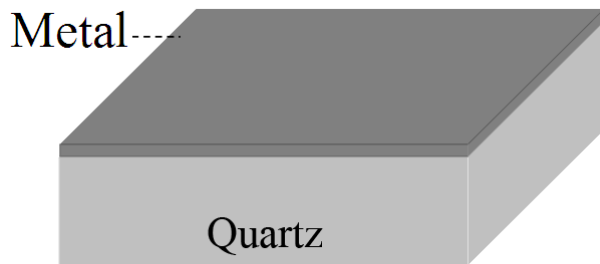


(a)

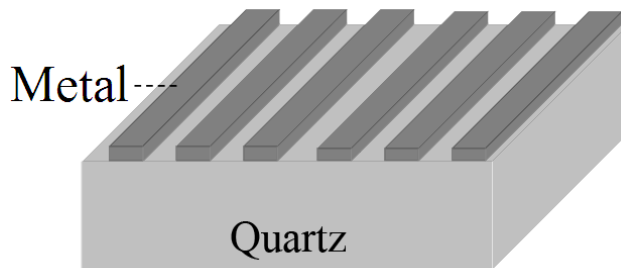


(b)

**Figure 2.4** SEM image of a 100-nm-wide slit arrays formed in a 140-nm-thick Ag layer using FIB etching technique. (a) Top view of 5 slit arrays with grating period of 450 nm. (b) Top view of 10 slit arrays with grating period of 350 nm.



(a) Metal film deposition on planar quartz substrate with thermal evaporation



(b) Forming metallic 1D slit arrays on quartz substrate using direct etching of metal layer with a focused-ion-beam (FIB) system

**Figure 2.5** Schematic of process flow forming 1D metallic slit arrays using FIB etching technique. (a)-(b) in sequence.

## 2.3 CHARACTERIZATION AND ANALYSIS OF THE OPTICAL TRANSMISSION SPECTRA

### 2.3.1 Arrays of large number ( $N > 1000$ ) slits

The optical transmission through the Ag slit arrays was measured at a spectral range of 350 ~ 1750 nm. As shown in Figure 2.6 (a), a beam from a multimode fiber (core diameter of 62.5  $\mu\text{m}$  and a numerical aperture of 0.20) connected to an unpolarized white light source (ANDO, AQ-4303B) was normally incident to a Ag slit array from the quartz substrate side. The zero-order transmission through a slit array was collected with another multimode fiber (core diameter of 62.5  $\mu\text{m}$  and a numerical aperture of 0.20) placed close to the Ag layer surface ( $< 1 \mu\text{m}$  gap), and was then characterized with an optical spectrum analyzer (ANDO, AQ-6315A). The transmission measurement was repeated with a dummy sample that has the same mesa-etched quartz structure but without a Ag layer. The transmission through a Ag slit array was then calculated by dividing the spectrum obtained from a real sample by the one from the dummy, a process designed to avoid (or alleviate) the effects of involving a mesa-etched quartz substrate structure and an optical fiber on the measured transmission spectra. Theoretically, as the wavelength is larger than two times of the mesa grating period, scattering effects of the mesa are very minor.

We also characterized the angular dependence of both transmission and reflection at a fixed wavelength (633 nm) using a He-Ne laser as shown in Figure 2.6 (b). The linearly polarized collimated beam (diameter of  $\sim 1 \text{ mm}$ ) was directly incident on the Ag side. Both transmitted and reflected lights were collected in far field by a Ge detector (power acceptance area diameter of  $\sim 1 \text{ cm}$ ) connected to an optical power meter.

Figure 2.7 shows the transmission spectra of the samples with a grating period of 370 nm and with a 120-nm-thick Ag or with a 200-nm-thick Ag, measured at normal incidence. Peak transmissions of approximately 30% and 15% are observed from the 120- and 200-nm-thick samples, respectively. Considering that the incident beam is unpolarized and the TE polarization component does not transmit through a slit array, the maximum transmission for TM polarization is estimated to be around 60%. This corresponds to  $\sim 500\%$  transmission efficiency, which is defined as the optical power transmitted through a slit divided by the incident power impinging upon the slit area. The main peak shifts from 660 to 690 nm as the Ag layer thickness is increased from 120 to 200 nm. The peak width also noticeably increased with the increased Ag thickness. This behavior, that is, the main peak's red shift and the peak width increase, is the opposite of the 2D aperture arrays case, in which the main peak initially blue shifts with reduced peak-width; the peak position and width then remain constant as the metal thickness is further increased [26,27]. The tendency observed in our work is rather consistent with the simulation results based on the model that involves the propagating modes in a slit in explaining the optical transmission through a slit array [23]. The clear difference between the 1D and 2D aperture arrays characteristics strongly suggests that different mechanisms are involved in transmitting the light through a slit or an aperture.

The transmission spectra in Figure 2.7 show three major dips. The minimum transmission point at around 580 nm tends to stay at nearly the same position for the raised metal thickness. This insensitivity to metal thickness suggests that the phenomenon occurring at this minimum transmission point involves an interaction of light primarily with the top or bottom surfaces of metal but not the sidewalls of slits. The SP resonance along the plane that comprises the metal/substrate interface of each metal island is expected to occur at 600 nm wavelength of light, based on a calculation using the formula

$$\lambda = \frac{L}{m} \sqrt{\frac{\epsilon_d \epsilon_m}{\epsilon_d + \epsilon_m}} \quad (2.1)$$

Here,  $L$  is the grating period,  $m$  is the order of the grating vector involved in SP coupling, and  $\epsilon_m$  and  $\epsilon_d$  are the dielectric constants of metal and adjacent dielectric (i.e., a quartz substrate in this case), respectively. The dielectric constant values of silver are assumed to be  $-12 + i0.9$  at 575 nm and  $-4 + i0.7$  at 400 nm wavelength, and the dielectric constant of quartz to be 2.16 [28]. This number calculated for  $m=1$  reasonably well matches the minima observed in Figure 2.7. Similarly the transmission minimum at around 430 nm well corresponds to the SP resonance at the air/metal interface, which is expected to occur at 430 nm according to the formula above, although an exact position cannot be clearly resolved due to an overlap with the bulk plasmon wavelength ( $\sim 360$  nm) at which a metal film is significantly transparent. It should also be noted that the sample with 120-nm-thick Ag shows a clear, well-defined major dip at around 800 nm, which corresponds to significantly longer wavelength than that of the transmission minima related to the metal/substrate interface. Considering that a slit structure allows propagating modes (or vertical SPs along the slit walls), it would be possible that the SP waves on the top and

bottom surfaces of a metal island couple to each other via the slit's sidewall. The SPs are then expected to resonate along the island surface; that is, the periphery of metal cross section when the following condition is satisfied along the closed loop:

$$\oint k_{sp} \cdot dr = 2\pi m \quad (2.2)$$

Here,  $m$  is an integer, and  $k_{sp}$  is the SP wave vector and can be expressed as

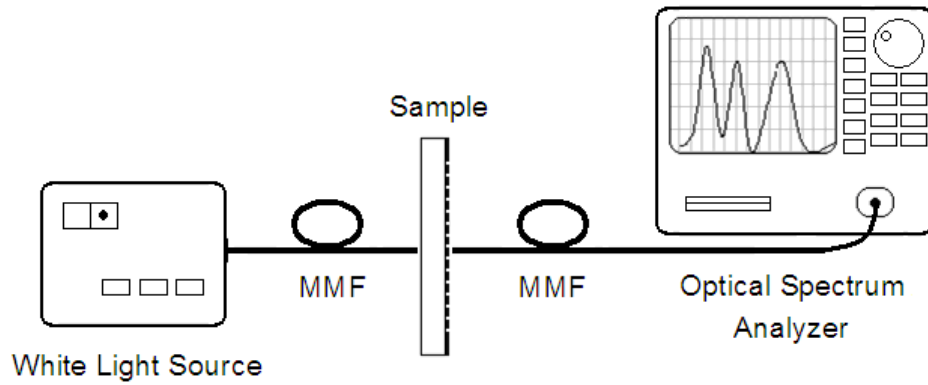
$$k_{sp} = \left( \frac{2\pi}{\lambda} \right) \left( \frac{\epsilon_d \epsilon_m}{\epsilon_d + \epsilon_m} \right)^{1/2} \quad (2.3)$$

where  $\lambda$  is the free-space wavelength of incident light. Along the periphery of metal cross section, the magnitude of the SP wave vector  $k_{sp}$  varies depending on the dielectric material interfacing with a metal; that is, either air or quartz in this case. If we assume a simple geometry of circular cross section with radius  $r_0$  surrounded by a homogeneous dielectric, the resonance condition in equation (2.2) is reduced to  $k_{sp}r_0=m$ . If we take an approximation that  $r_0=110$  nm and 30% of the metal periphery interfaces with silica and the rest with air, the resonance wavelength is calculated to be 820 nm for the dipolar resonance case; that is,  $m=1$  (In this calculation, we assumed the dielectric constant of Ag to be  $-29 + i1.7$  and neglected the plasmon coupling between metal islands). This number closely matches the location of the transmission dip (800 nm) of the sample with 120-nm-thick Ag, as shown in Figure 2.7. The minimum transmission point shifts to longer wavelength as the metal thickness is increased. This behavior is also consistent with the resonance condition discussed earlier. It is important to note that this

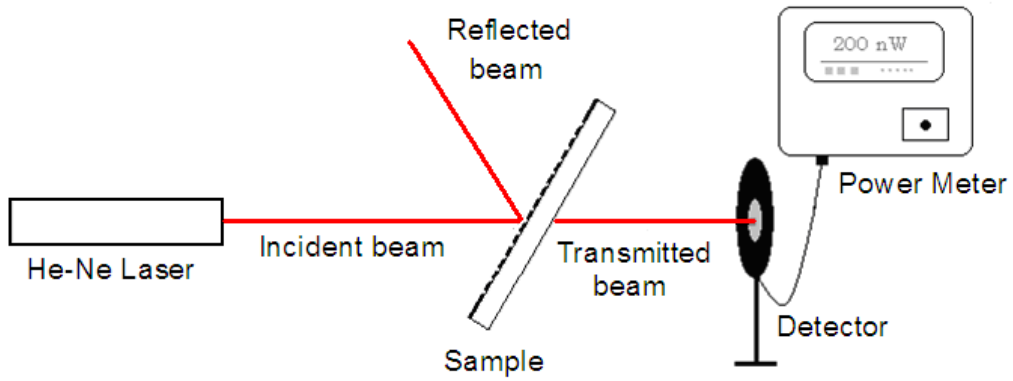
surface plasmon resonance is a phenomenon highly localized at each metal island and differs from the SP resonance that occurs along the planes that comprise either the top or bottom surfaces of an array of metal islands. This localized SP resonance reminiscent of the electron orbital of atoms [29]. Well-defined transmission minima have been observed with metal particles of variable sizes and the anomaly has been ascribed to the localized SP resonance in metal spheres [30]. The transmission dip at  $\sim 870$  nm of the 200-nm-thick sample looks less pronounced, primarily due to the significant decrease of transmission in the long wavelength region. This is ascribed to the enhanced coupling of SPs between metal islands with the reduced slit width.

Overall, the results strongly suggest that the three major transmission minima observed in this work can be ascribed to the SP resonances that involve different sections of the metal surfaces. In order to consolidate this observation, we have characterized the angular dependence of both transmission and reflection at a fixed wavelength (633 nm) using a He-Ne laser. For a TM polarized light at this wavelength, the transmission shows a minimum when the incidence angle is  $45^\circ$  (the blue curve in Figure 2.8). This angular position well matches the value ( $43^\circ$ ) that is calculated from the condition for SP excitation at the plane that comprises the metal/substrate interfaces; that is,  $k_{sp}=k_0 \sin\theta\pm mK_g$ , where  $k_0$  is the wave vector of an incident beam,  $\theta$  is the incidence angle measured from the substrate normal, and  $K_g$  is the grating vector. It is interesting to note that the reflection (the black curve) shows a maximum with a sharp peak profile (with the full width at half-maximum of  $2^\circ \sim 3^\circ$ ) at the same incidence angle. The power loss, calculated as the difference between the incident power and the transmitted plus reflected power, is minimal at the SP resonance point. It might be argued that this result can be attributed to the diffraction-related Wood's anomaly, which occurs at close proximity to the SP resonance

point. The narrow reflection peak observed in this work, however, suggests the dominant role of SP resonance in this transmission/reflection anomaly.



(a)



(b)

**Figure 2.6** Set-up for optical characterization of Ag subwavelength gratings with narrow slits. (a) Characterization of zero-th order transmission spectrum in the wavelength range of 350 ~ 1750 nm. (b) Characterization the angular dependence of both transmission and reflection at a fixed wavelength (633 nm) using a He-Ne laser

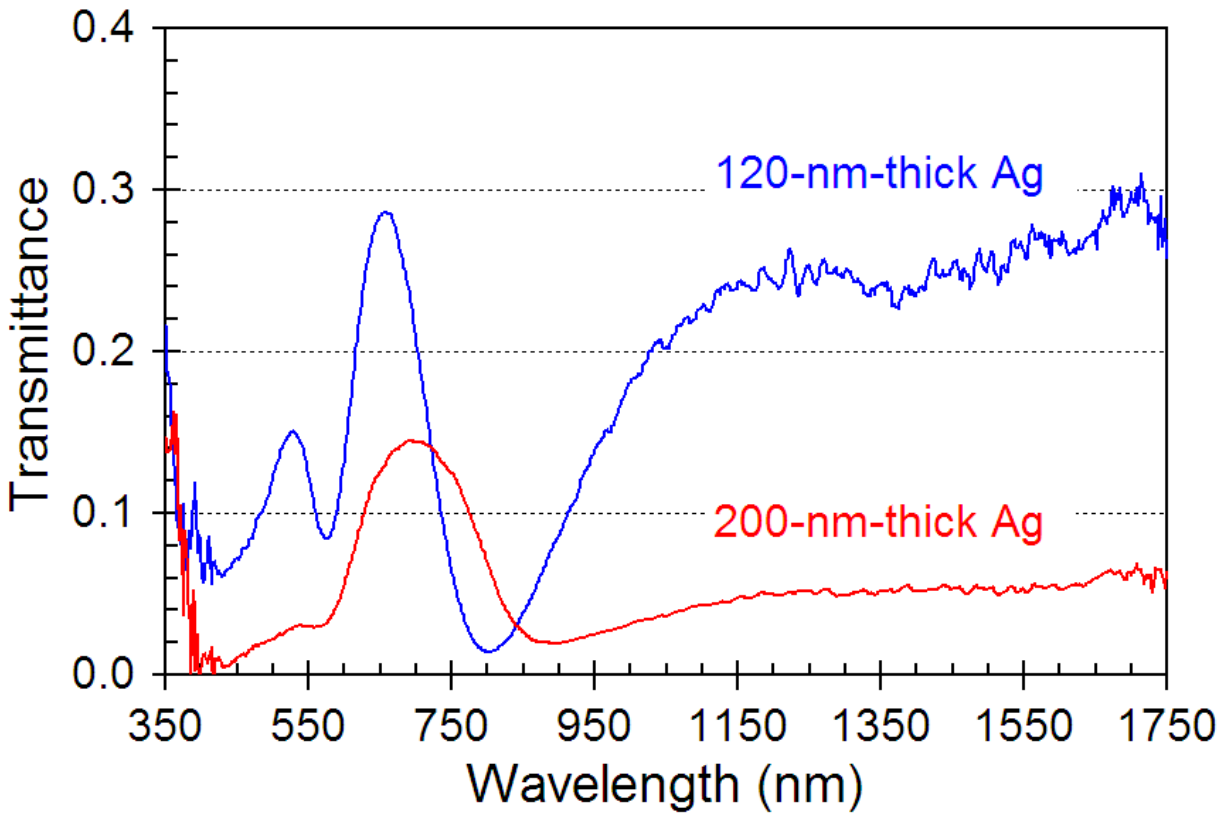


**Figure 2.7** Transmission spectra of a 1D slit array sample with grating period of 370 nm and with 120 nm (blue) or 200 nm (red) thick Ag. The input beam was incident normal to the Ag side surface. Considering that the incident beam is unpolarized and the TE polarization component does not transmit through a slit array, the peak transmission is estimated to be over 60% for TM polarization.

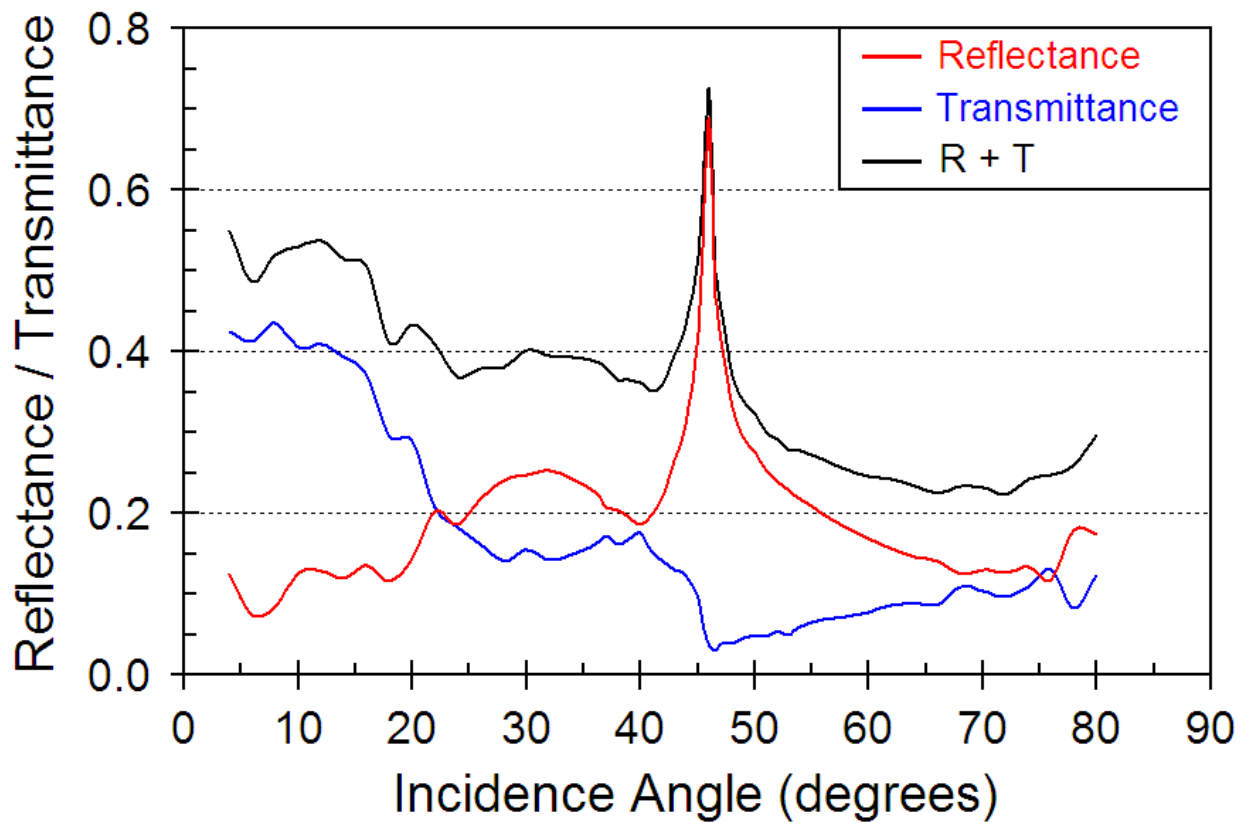


**Figure 2.8** Transmission and reflection measured as a function of incidence angle at the wavelength of 633 nm (TM polarized): the 1D slit array sample with 120-nm-thick Ag shown in Figure 2.7. The transmission profile (blue) shows a minimum at 45°, whereas the reflection (red) shows a maximum at the same incidence angle. The power loss, estimated from the difference between the incident power and the transmitted plus reflected power, is minimal at around the surface plasmon resonance point, as shown in black curve.

### 2.3.2 Single slit and 2 ~ 10 slit arrays

Figure 2.9 shows SEM images of 1 ~ 10 slit array formed on a quartz substrate. The silver nanoslit arrays used in this study were fabricated using an electron beam lithography and plasma etching technique in conjunction with angle deposition ( $45^\circ$ ) of metal (See Chapter 2.2.1 for experimental details.). The slit width was  $\sim 50$  nm with the slits period of 360 nm. The Ag thickness was controlled to be 140 nm. The optical transmission through the Ag slit arrays was measured in the spectral range of 350–1750 nm using unpolarized light at normal incidence. Figure 2.10 shows the measured transmission spectra of the slit arrays as a function of slits number. The transmission spectra of only two-slit arrays reveal basically the same spectral profile as those an infinite grating array discussed in the previous section. The peak profile becomes better defined as the number of slits increases. The peak position remains constant for 2 to 10 slits. The transmission peak of a nanoslit array corresponds to the quadrupolar resonance of surface plasmons on the periphery of individual metal stripe, and details of this correspondence will be discussed in Chapter 5.

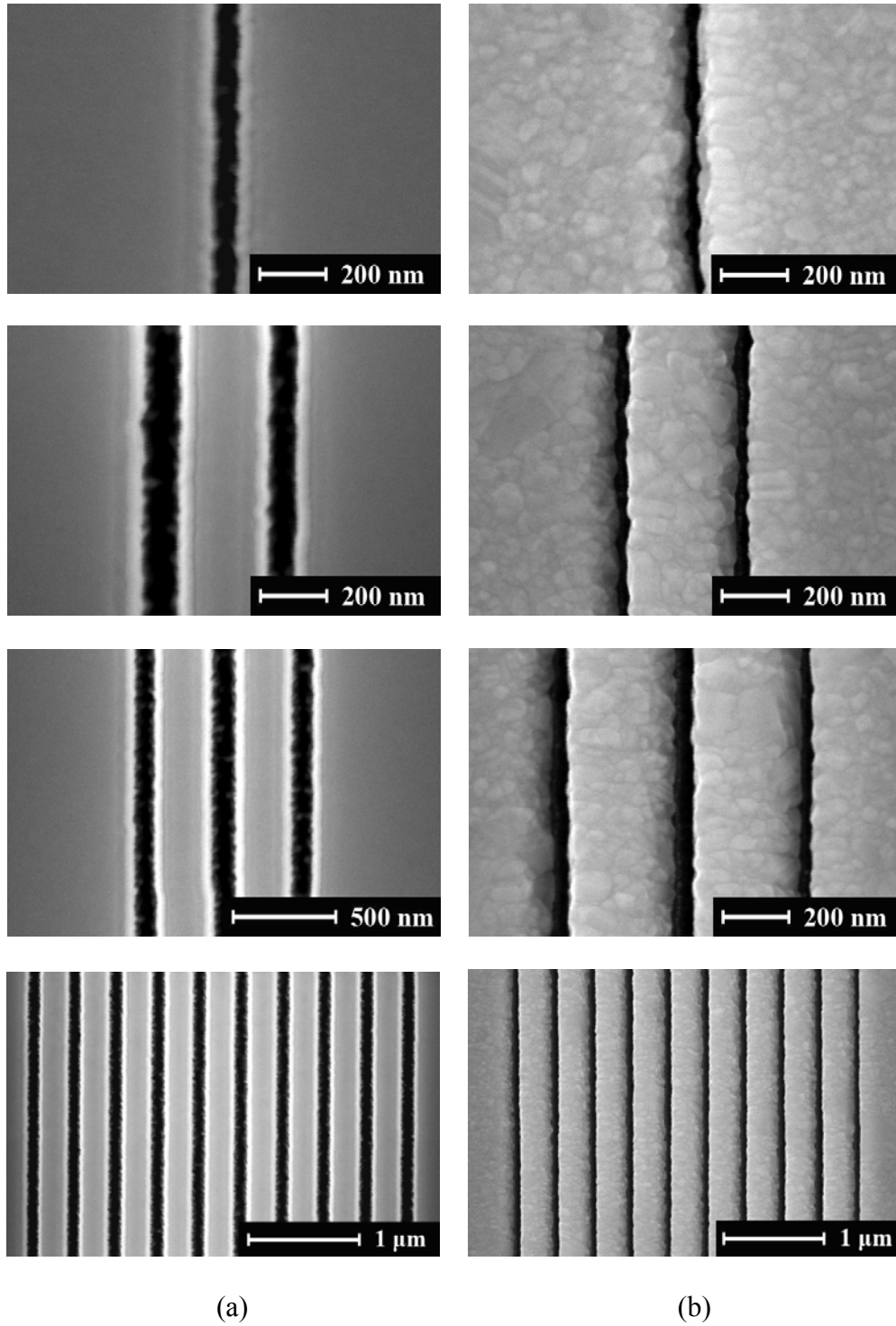
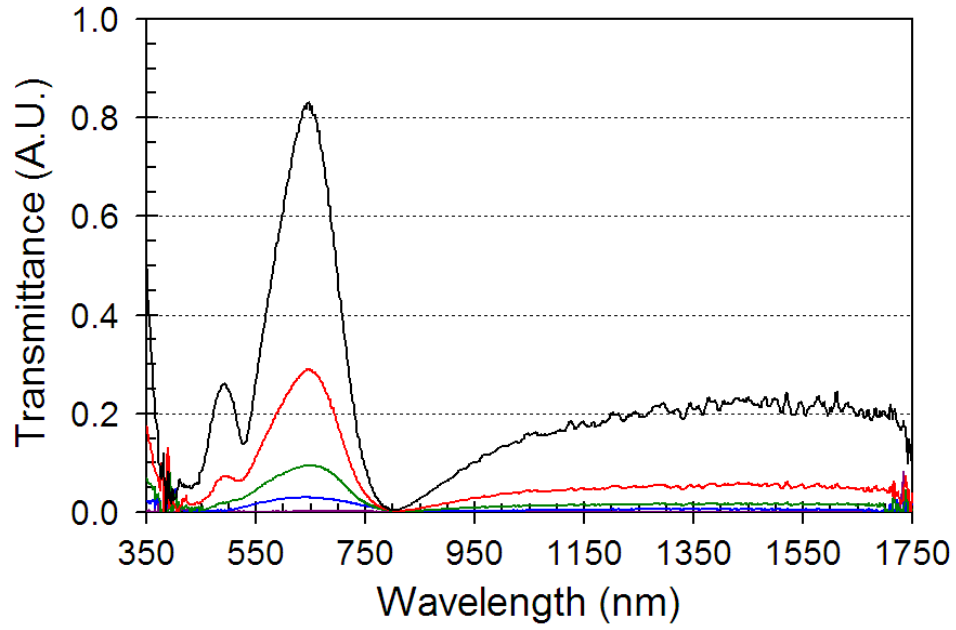
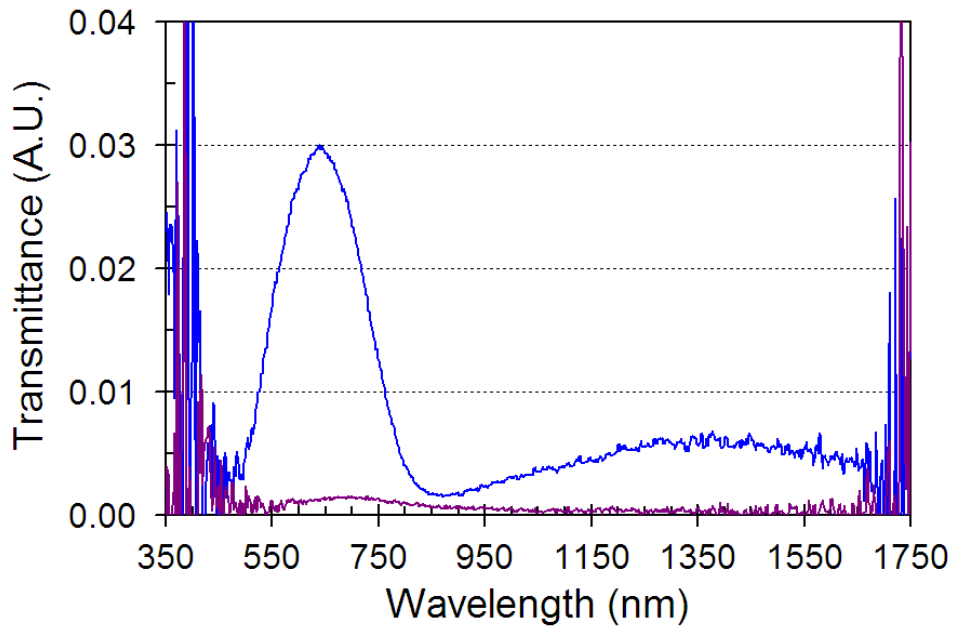


**Figure 2.9** SEM images of 1 ~ 10 slit arrays formed on a quartz substrate using an electron beam lithography technique and angled metal deposition. (a) Top view of slit arrays with grating period of 360 nm without Ag. (b) Top view of slit arrays with grating period of 360 nm and Ag thickness of 140 nm. Opening of slits is clearly revealed with slits of 50 nm along the depth.



(a)



(b)

**Figure 2.10** The measured transmission spectra through the slits as a function of slits number. (a) 10 (black), 5 (red), 3 (green), 2 slits (blue) and single slit (violet) (top down). (b) Magnified plot of 2 slits (blue) and single slit (violet).

## 2.4 SUMMARY

In this study, we have investigated optical transmission through narrow slits in metallic gratings. The surface plasmon resonance is found responsible for the observed transmission minima, involving two different modes of interaction (the in-plane SP resonance along the top or bottom interfaces of a metal layer and the localized SP along the periphery of each metal stripe with the 1D slits arrays). Also, the minimum number of slits to observe localized SP resonance is found to be two. At these resonance points, standing waves develop with their nodal points at the slit corners on the incident or exit side. No net power flows along the metal surfaces and thus there is no funneling of incident power into a slit region. The incident power then strongly reflects back from the metal surface without incurring any major loss of power [19]. For the case of relatively thin metals, the peak transmission of a slit array is found to correspond to the situation that a different type of resonance develops with their nodal points fixed at the slit corners on both incident and exit sides. This particular situation is believed to enable efficient excitation of surface plasmons at the incident corner and also decoupling of the slit transmitted surface plasmons in free-space radiation. [19].

### **3.0 BLUESHIFT OF SURFACE PLASMON RESONANCE SPECTRA IN ANNEAL-TREATED SILVER NANOSLIT ARRAYS**

#### **3.1 INTRODUCTION**

Interactions of light with metal nanoslit arrays produce many interesting phenomena and have been the subject of extensive studies [31-36]. Essential to understanding the overall phenomena is to elucidate the mechanisms of surface plasmon (SP) interactions with the metal structure. Transmission of light through metal nanoslit arrays, for example, shows characteristic spectra with clear peaks and dips. The metal nanoslit array structures support various different modes of surface plasmon resonance involving different sections of metal surfaces [37,38]. The SP resonance points are found to correspond to the dips and peaks of the transmission spectra. The SP waves localized to each metal island can also interact with neighboring ones via near-field coupling across the slit, and this can significantly alter the transmission spectra [37].

In this study, we report our further study of the plasmonic phenomena occurring in silver nanoslit array structures. We have investigated the effects of thermal annealing on the surface plasmon resonance characteristics in the arrays. The spatial extension of SP waves is usually an order of magnitude smaller than the wavelength along the propagation direction [39]. The array structures were designed to span nano- to micrometer length scales in feature sizes, i.e., the slit width of the 10 nm order and the grating period of the 100 nm order. This is to accommodate the

interactions of waves (plasmonic and photonic) with the structure involving different length scales. The metal nanoslit arrays were formed by angle deposition of silver on mesa-etched quartz substrates. Anneal treatment of a deposited metal film is expected to alter the microstructure of metal (such as grain boundaries, surface roughness, etc.) and the size and shape of each metal island separated by slits, and thus the gap between them (i.e., slit width). This annealing-induced change of metal that may occur at nano- to microscale is expected to sensitively affect the SP interactions with the metal.

## **3.2 FABRICATION AND CHARACTERIZATION**

### **3.2.1 Fabrication of the silver nanoslit arrays**

The silver nanoslit arrays used in this study were fabricated using a holographic lithography and plasma etching technique in conjunction with angle deposition of metal (See Chapter 2.2.1 for experimental details.). Grating periods are designed to be 400 nm, and slit width in the range of 50 ~ 120 nm. The metal thickness is controlled to be 200 nm. The Ag-deposited sample was then cut into two pieces and one was anneal-treated in vacuum ( $1 \times 10^{-6}$  Torr) for 30 min at 150 °C.

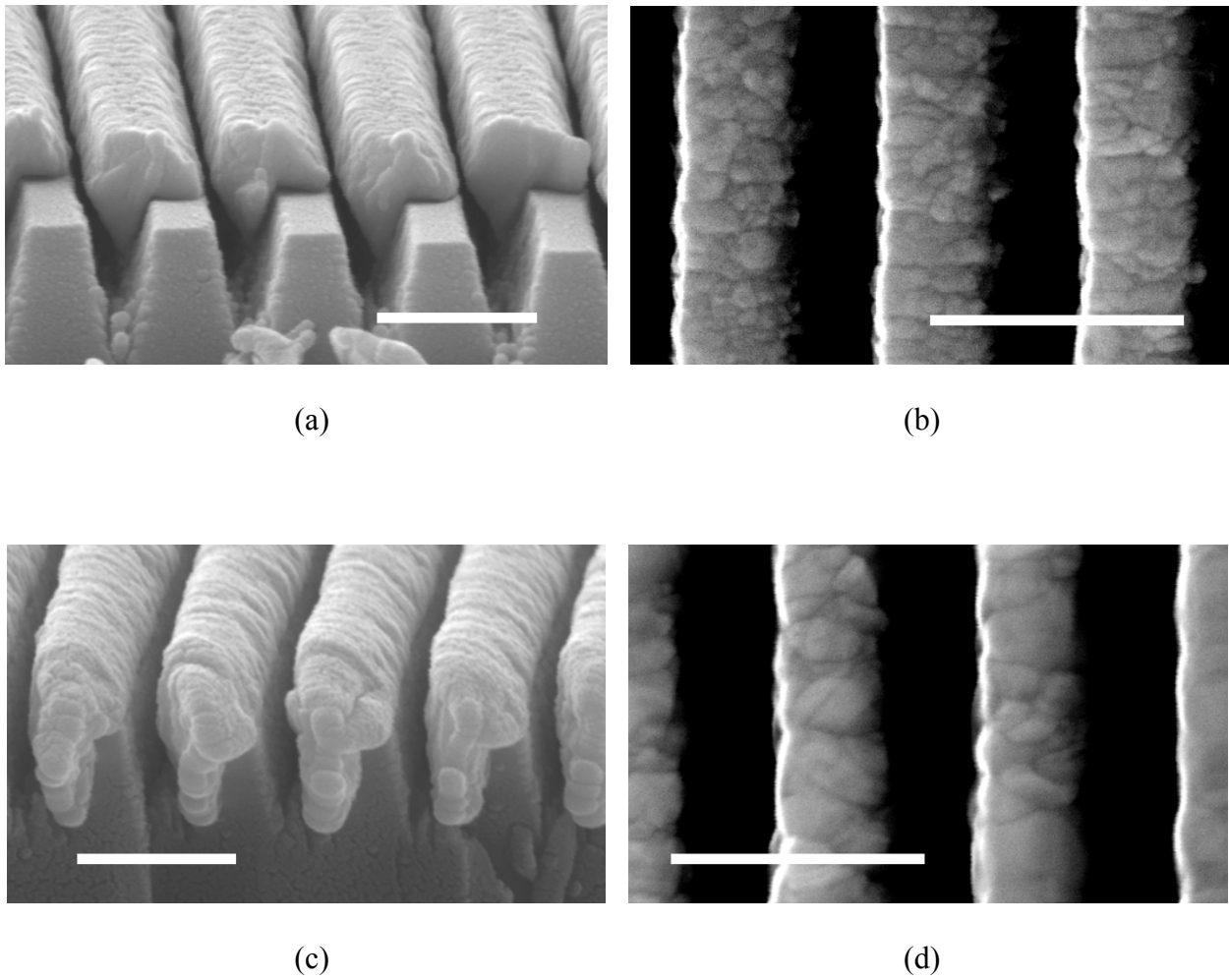


**Figure 3.1** SEM micrographs of a silver nanoslit array structure formed on a mesa-etched quartz substrate: the effects of annealing (at 150 °C in vacuum for 30 minutes) on the morphology of metal. The silver layer was deposited on mesas with an evaporation flux incident from the left-hand side of mesas with tilt angle of 45°. (a) Side view of an as-deposited sample. (b) Top view of an as-deposited sample. (c) Side view of an anneal-treated sample. (d) Top view of an anneal-treated sample. The scale bar is 500 nm.

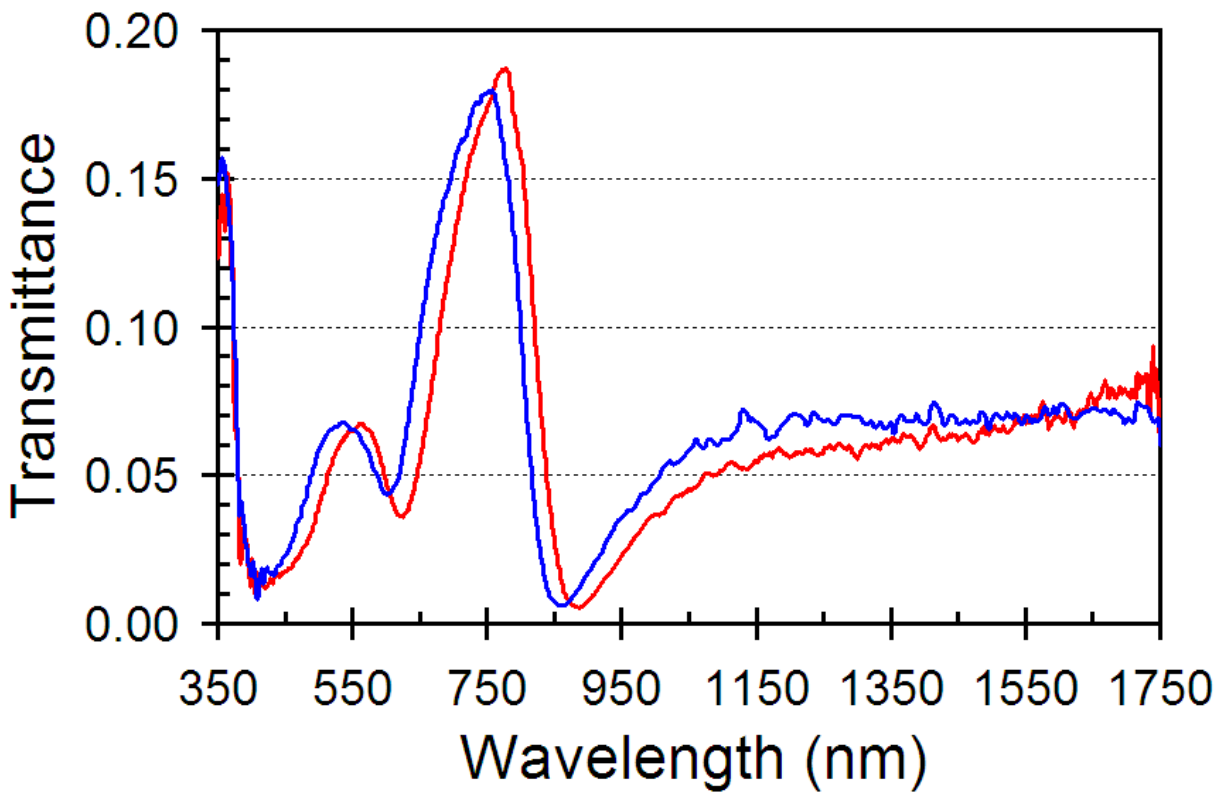


**Figure 3.2** Transmission spectra of a silver nanoslit array structure shown in Figure 3.1: as-deposited (red), and after anneal-treatment in vacuum (blue).

### 3.2.2 Characterization

The optical transmission through the Ag slit arrays was measured in the spectral range of 350–1750 nm using unpolarized light at normal incidence. Details of measurement setup of a silver nanoslit array structure of the same geometry have been described in Chapter 2.3.1. Figure 3.1 (a) and (b) show scanning electron microscope (SEM) images of an as-deposited Ag nanoslit array sample. Well-defined quartz mesas are revealed with sharp edges and flat top and sidewalls profiles. The silver layer was deposited on mesas with an evaporation flux incident from the left-hand side of mesas with tilt angle of  $45^\circ$ . The SEM image shows a conformal profile of Ag surface, i.e., an inverted “L” shape with a relatively sharp edge at the left-hand side of the top surface. The amount of metal deposited on the left sidewall of mesas is nearly the same as that on the mesa top, a result consistent with the angle deposition condition described above. The gap between Ag islands is estimated to be around 30 nm. Figure 3.1 (b) shows a plan-view image of the same sample. The surface morphology of as-deposited Ag reveals many grain boundaries in each metal island (with grain size typically on the order of 10 nm). The granular structure is commonly observed in deposited metal films. The apparent wide opening of the gap between Ag islands in this plan-view image is an artifact caused by the location of the detector to the left of the sample, essentially a shadow effect [40].

Figure 3.1 (c) and (d) shows SEM images of the anneal-treated sample. Annealing of Ag, performed at the relatively mild temperature ( $150^\circ\text{C}$ ), is found to induce significant changes in the morphology of metal. The grain sizes grew to 50 ~ 100 nm range, and some grains are over 200 nm, showing a “bamboo” structure along the mesa (Figure 3.1 (d)). Figure 3.1 (c) shows another major change in the cross-sectional profile: The initially conformal profile of metal surface became round and smooth after annealing. This cross section was obtained by cleaving

the anneal-treated sample. It is interesting to note that the bottom edge of metal deposited on the left-hand sidewall of mesas also became round. This indicates that dewetting of metal on silica surface occurs even at this relatively low temperature of annealing. The Ag layer was deposited with an evaporation flux incident from the left hand of mesas in this image shown in Figure 3.1 (c), and the as-deposited Ag shows extremely small contact angle in the bottom edge as shown in Figure 3.1 (a). Grain growth and dewetting can be explained by the tendency of metal to minimize its surface energies [41]. Grain growth can occur through motion of grain boundaries, which results in the shrinkage and elimination of small grains, and an eventual increase in the average grain size of the remaining grains. Wetting depends on the relative surface and interface energies. Dewetting of a film can occur at the film edges during annealing if the surface energy of a substrate is smaller than the sum of the surface and interface energies of a film.

Diffusivity of material is a strong function of temperature, and as such both grain growth and dewetting processes are expected to show similar dependency. 150 °C anneal temperature corresponds to the homologous temperature of 0.34 K, which is defined as the temperature in degrees K divided by the melting temperature (also in degrees K) of the material under consideration. In thin-film studies of Ag, it has been known that grain boundary motion plays an important role in grain growth even at homologous temperatures as low as 0.2 K [41]. Overall, the densification (resulting from grain growth) and the shape change (round edges and circular cross sections caused by the grain growth and dewetting) increased the slit width to 50 to 80 nm range.

Figure 3.2 shows optical transmission through the Ag nanoslit arrays before and after the anneal treatment. An unpolarized white light was incident normal to the substrate surface. The zero-th order transmission through the Ag nanoslit array was collected and analyzed with an

optical spectrum analyzer. The peak transmission of an unpolarized light is measured to be around 20 %. When normalized for a TM polarized light, the transmission would be two times this value, i.e., 40% transmission for TM polarization. The transmission spectra show a clear blueshift after the anneal treatment, although the transmittance basically remains at the same level. The transmission peak at 780 nm of the as deposited sample, for example, shifted to 760 nm, and a similar amount of shift with the minor peak at 560 nm, and the dips at 620 nm and 890 nm. The transmission dip at around 430 nm is not clearly resolved due to the proximity to silvers' SP resonance at around 350 nm. The transmission minima at around 430 nm or 620 nm correspond to the SP resonances along the planes that are composed of either air-or quartz-side surfaces of metal islands, respectively [37,42,43]. The transmission dip at around 890 nm is ascribed to the SP resonance localized at each metal island, i.e., the resonance along the periphery of metal island surface [37]. The wavelength that corresponds to an in-plane SP resonance can be expressed as follows [39]:

$$\lambda = \frac{d}{m} \operatorname{Re} \left( \sqrt{\frac{\varepsilon_d \varepsilon_m}{\varepsilon_d + \varepsilon_m}} \right) \quad (3.1)$$

where  $d$  is the grating period,  $m$  is the order of the grating vector involved, and  $\varepsilon_m$  and  $\varepsilon_d$  are the dielectric constants of metal and dielectric (air or quartz), respectively. It should be mentioned that this condition is valid for asymptotically small amount of perturbations, for example, infinitesimally shallow corrugations of metal surface or narrow slit width relative to the grating period. The annealing-induced change in the geometry and size of metal islands is expected to alter the SP resonance condition. As the slit width (i.e., air gap) increases for a given period of

grating, the SP waves propagating along either side (air or quartz side) of the periodic structure will have an increasing presence in the air gap region. Since the free-space wave vector is smaller than the SP wave vector along the metal surface, the resonant wavelength is expected to blueshift with the increased air-gap portion. In the case of SP resonance localized to each island, a blueshift is also expected after annealing: The total periphery of each island decreases (as shown in the round cross section of metal islands), therefore, the corresponding resonant wavelength will decrease.

### 3.3 RESULTS AND DISCUSSION

In order to substantiate the observed blueshift, we analyzed the energy band structure of SP waves interacting with the periodic metal/air gap structure. In the case of the in-plane SP waves propagating along the quartz-side surfaces of metal islands, the problem can be reduced to a one-dimensional (1D) periodic bilayer structure. Using the transfer matrix method, the following dispersion relation can be obtained between an in-plane SP wave vector  $k$  and the free-space wavelength  $\lambda_0$  [44].

$$\cos(kd) = \cos(k_0 a) \cos[k_m (d - a)] - \frac{1}{2} \left( \frac{k_0}{k_m} + \frac{k_m}{k_0} \right) \sin(k_0 a) \sin[k_m (d - a)] \quad (3.2)$$

where  $a$  is the slit width (air gap) and  $d$  is the grating period.  $K_0$  is the free-space wave vector,  $2\pi/\lambda_0$ .  $k_m$  is the SP wave vector in the metal region, expressed as follows:

$$k_m = \text{Re} \left( \sqrt{\frac{\varepsilon_d \varepsilon_m}{\varepsilon_d + \varepsilon_m}} \right) k_0 \quad (3.3)$$

Regimes where  $|\cos(kd)| \leq 1$  correspond to real  $k$  and thus to propagating Bloch waves: when  $|\cos(kd)| > 1$ , however,  $k$  has an imaginary part so that the Bloch wave becomes evanescent, i.e., entering into a forbidden band regime. Figure 3.3 shows the band structure,  $\lambda_0$  versus  $\text{Re}(k)$ , calculated for grating period  $d$  of 400 nm, and slit width  $a$  of 80 nm (solid curve) or 120 nm (dashed curve). The dielectric constants of Ag and quartz used in this simulation are from Ref. 15. The slit width was chosen in this range based on the SEM cross-sectional images shown in Figure 3.1. Due to the rather complex geometry of the metal's cross-section, it is not straightforward to read the slit width, and this number is considered effective slit width measured at the metal/quartz interfaces. A clear opening of band gap is observed at the wavelength around 600 nm. As the slit width increases, the band-gap blue shifts (with the longer wavelength edge moving from 630 nm to 610 nm). At this wavelength range, the light incident normal to the slit array surface excites SP waves, assisted by the first-order grating vectors ( $\pm 2\pi/d$ ). The in-plane SP waves propagating the opposite directions resonantly couple to each other, assisted by the second-order grating vectors available in the same structure. A resonant interaction between the two counter-propagating SP waves results in the formation of standing waves along the in-plane propagation direction. There are two possible standing waves with different energies so that there is an energy gap in the modal dispersion [46]. One may anticipate observing another band gap at around 1200 nm wavelength. This band-gap regime, however, cannot be reached in this experiment, since a beam normally incident to a grating (of period  $d$ ) cannot excite the desired SP wave vectors ( $\pm 2\pi/d$ ). Overall, this band structure calculation confirms that the in-plane SP

resonance point corresponds to the minimal point of far-field transmission of light through the slit array and also that the amount of blue shift observed in the transmission spectrum of an annealed sample is reasonable compared to the slit width increase observed with SEM.

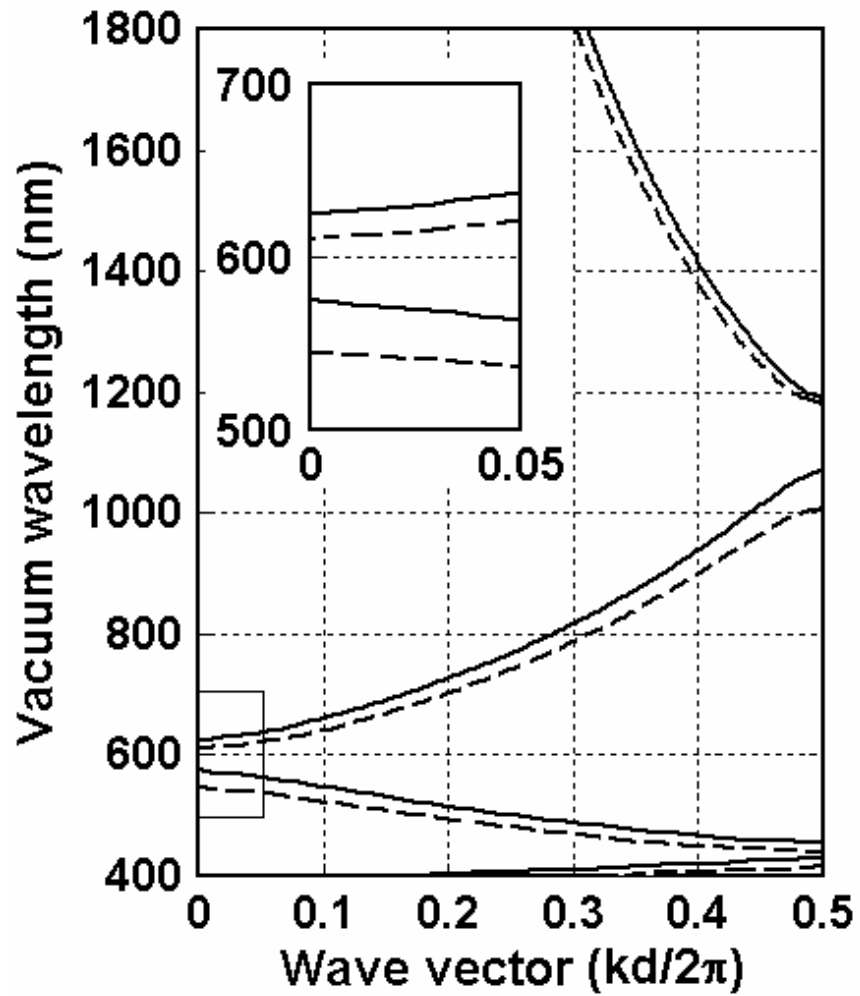


**Figure 3.3** Surface plasmon band structure calculated for a 1D silver nanoslit array structure with grating period of 400 nm: slit width of 80 nm (solid curve) and 120 nm (dashed curve). The inset shows a magnified view of the bandgap opening around 600 nm wavelength.

### 3.4 SUMMARY

We have anneal-treated silver nanoslit arrays in a vacuum and investigated its effects on the surface morphology of silver and the surface plasmon resonance characteristics. Optical transmission through nanoslit arrays shows a distinctive change in the spectral profiles after annealing: a clear blueshift (20 nm) of transmission spectra was observed after annealing at 150 °C. The observed blueshift correlates well with the geometrical and dimensional changes of silver islands and slits as revealed by SEM analysis: increased grain sizes, smooth, and round surface profiles of metal, and increased slit width after the anneal treatment. This study offers an interesting approach to altering surface plasmon resonance characteristics and thus optical transmission properties of metal nanoslit arrays.

## **4.0 HIGH-SENSITIVITY SURFACE PLASMON RESONANCE SPECTROSCOPY BASED ON A METAL NANOSLIT ARRAYS**

### **4.1 INTRODUCTION**

Surface plasmon resonance (SPR) spectroscopy is widely used in chemical and biological sensing [47]. The SPR technique senses the integral changes in the dielectric ambient in the vicinity of the metal surface that supports the surface plasmon waves. In other versions of surface plasmon sensing based on the Kretschmann configuration [48], the intensities of scattered and transmitted fields are used to determine the thickness and dielectric constant of an unknown coating [49]. At a planar metal/dielectric interface, the plasmon fields evanescently extend into the dielectric with 200 ~ 300 nm depth and into the metal with 20–30 nm depth [48]. In the case of metal particles or thin metal island films, the plasmonic fields can be more narrowly confined to the metal surface with 10 ~ 30 nm penetration depth to adjacent dielectric [50]. Strong confinement of plasmonic fields near the metal surface can be utilized for the benefit of enhancing plasmonic interactions with an analyte layer and thus for efficient transduction and sensing of surface binding events. Recently there has been a growing interest in SPR sensing of biochemicals using a nanostructured metal layer (nanoparticle or nanohole) [50-54]. Nanostructure-based SPR sensing can also operate in the transmission configuration, thereby simplifying the optical arrangement and requiring small amounts of analyte.

In this study, we report a transmission SPR sensor based on a metal nanoslit array structure. Optical transmission through metal nanoapertures has recently been a subject of great interest, primarily because of the plasmonic phenomena that result in strong confinement of light and its funneling into subwavelength channels [55]. Biochemical sensing based on an array of subwavelength holes has been reported, demonstrating a beneficial use of strong confinement of light in nanoapertures [52,53]. Despite the simple geometry, a nanoslit array offers unique properties that cannot be attained with nanohole arrays [56-58]. A metal nanoslit, for example, supports guided modes without cutoff wavelength, whereas optical transmission through a metal nanohole array is critically limited by the hole size and metal thickness [55-58]. This feature suggests that metal nanoslit arrays may be intrinsically more suitable for transmission-mode SPR sensing.

Optical transmission through metal nanoslit arrays shows characteristic spectra involving surface plasmon resonances that occur at various sections of the metal surfaces. We have chemically modified metal nanoslit array surfaces with alkanethiol self-assembled monolayers, and have characterized the resulting spectral shift of optical transmission. Adsorption of a self-assembled monolayer (1.5-nm thick) on a silver nanoslit array (slit width of 30-50 nm and grating period of 360 nm) is found to cause an 11 nm red-shift of the main transmission peak. Analysis of the plasmonic fields and charge distributions shows that the strong confinement of optical fields in the narrow slit region allows sensitive transduction of surface modification into a shift of surface plasmon resonance wavelength. The nano-slit-array-based surface plasmon spectroscopy is amenable to ultracompact miniaturization of instruments for biochemical sensing.

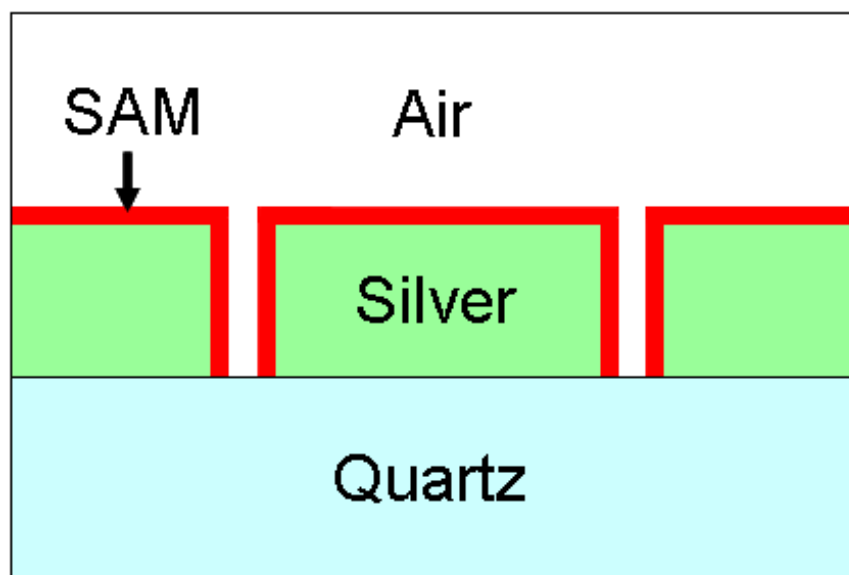


**Figure 4.1** Schematic drawing of the fabricated Ag nanoslit array structure (after adsorption of a SAM).

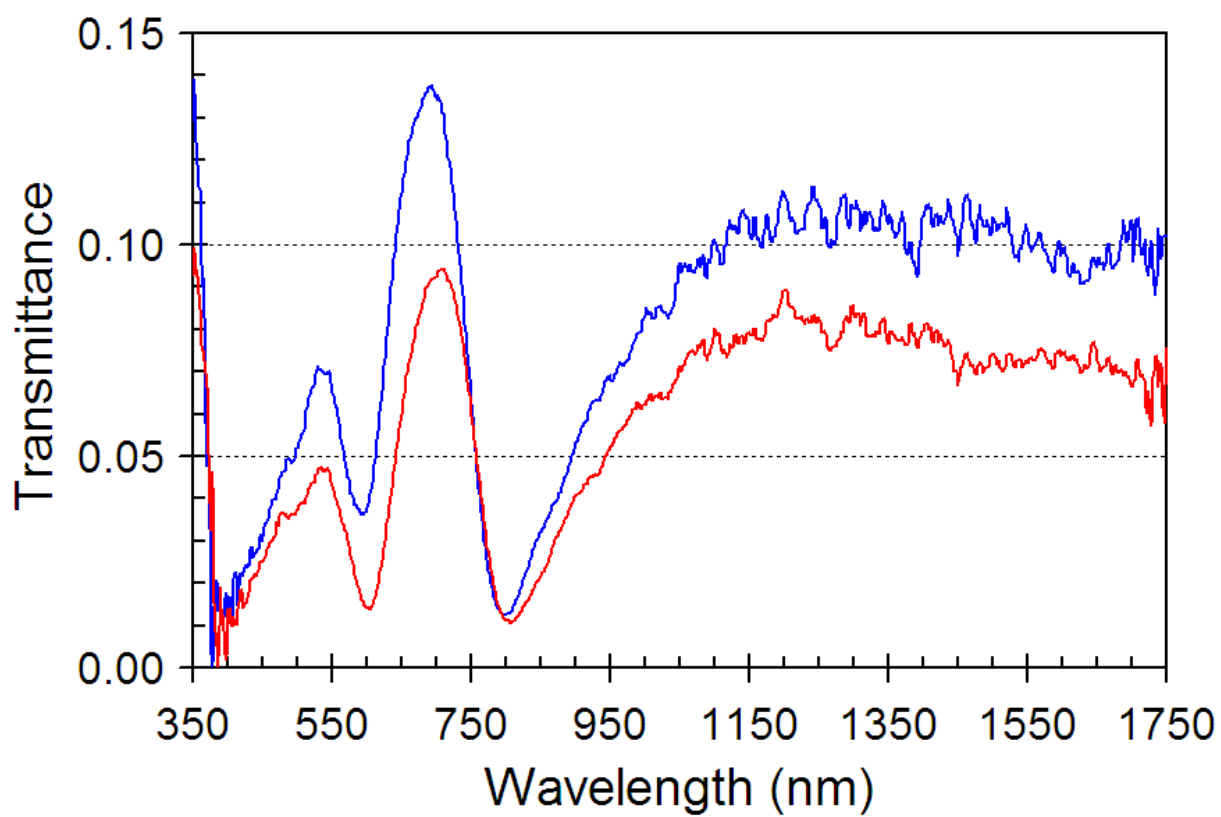


**Figure 4.2** Optical transmission through a Ag nanoslit array: before chemical modification of metal surface (blue) and after adsorption of an alkanethiol self-assembled monolayer (red).

## 4.2 FABRICATION AND CHARACTERIZATION

### 4.2.1 Fabrication of the nanoslit arrays

The nanoslit arrays used in this study were fabricated using a holographic lithography and/or E-beam lithography methods, and plasma etching technique in conjunction with angle deposition of metal. Details of fabrication of a silver nanoslit array structure have been described in Chapter 2.2.1. In this work, we have used a 190-nm-thick silver slit array. The slit width is designed to be in the range of 30-50 nm, and the grating period is 360 nm. The sample was then chemically treated to coat the metal surface with an alkanethiol self-assembled monolayer (SAM) [HS(CH<sub>2</sub>)<sub>7</sub>COOH]. Alkanethiols on Ag is one of the most widely-used SAMs with well-established chemistry. They form dense, well-ordered, tightly-bonded films on Ag, and the SAM can be easily tailored to incorporate a variety of molecular recognition elements designed for specific binding [59].

### 4.2.2 Characterization

The optical transmission through the Ag slit arrays was measured in the spectral range of 350–1750 nm using unpolarized light at normal incidence. Details of measurement setup of a silver nanoslit array structure of the same geometry have been described in Chapter 2.3.1

Figure 4.1 shows a schematic drawing of the silver nanoslit array structure studied in this work. A 190-nm-thick Ag slit array was formed on a quartz substrate. The slit width is designed to be in the range of 30–50 nm, and the grating period is 360 nm. The sample was then chemically treated to coat the metal surface with an alkanethiol self-assembled monolayer

(SAM) [HS(CH<sub>2</sub>)<sub>7</sub>COOH]. Alkanethiols form dense, well-ordered, tightly bonded films on Ag, and the SAM can be easily tailored to incorporate a variety of molecular recognition elements designed for specific binding [59]. Optical transmission through the Ag nanoslit array was then characterized in the spectral range of 350 – 1750 nm, using unpolarized light at normal incidence. The as-deposited nanoslit array shows a characteristic transmission spectrum with clear peaks defined by transmission minima (the blue curve) in Figure 4.2. Light which is incident on the nanoslit array excites surface plasmons (SPs) on the nanoapertured metal surface, and the SP waves are funneled into and propagate through each slit. Part of the SPs emerging from the slits couples into the SP waves propagating laterally towards the neighboring slits, while some decouples into radiation modes. The laterally propagating SPs encounter a periodic perturbation introduced by the slit array and form Bloch waves. The SPs' periodic interaction with the media results in formation of plasmonic band gap around the resonance point, similar to the dielectric-based photonic crystal's case [60,61]. The transmission dip at 400 nm corresponds to the in-plane SP resonance at the metal/air interface and the transmission dip at 600 nm corresponds to the metal/quartz interface [58]. The dip at 800 nm corresponds to the surface plasmon resonance localized around each metal island.

Adsorption of a SAM causes a redshift of the transmission spectrum (the red curve in Figure.4.2). The amount of redshift measured with the main transmission peak at around 690 nm is 11 nm. The thickness of the SAM is estimated to be 1.5 nm. The sensitivity of this response, defined as the ratio of the transmission spectral shift to the adsorbed analyte layer thickness, is calculated to be 7. In the case of nano-hole-array-based SPR sensing, a sensitivity of 2.5 was reported: 4 nm spectral shift for adsorption of a 1.7-nm-thick SAM on Ag nano-holes, measured with similar analyte/ambient dielectric contrast, i.e.,  $\epsilon_a/\epsilon_d = 2.1/1.0$  [53]. In order to better

understand this nano-slit-array-based SPR sensor's response to analyte coverage, we have analyzed the plasmonic interaction of an incident light wave with an adsorbed analyte layer.

### 4.3 RESULTS AND DISCUSSION

Figure 4.3 shows the finite-difference time-domain (FDTD) analysis of the SP polarization charge distribution on a metal surface calculated at 650 nm wavelength, which is close to the peak transmission point. The blue and red colors represent negative and positive polarity of the charges, respectively [62]. The polarization charges show a quadrupolar distribution along the periphery of each metal island separated by slits [62]. A single period of charge oscillation spans one plasmonic wavelength, and the plasmon wavelength depends on the nature of metal/dielectric interface. From the quadrupolar resonance condition, the optical wavelength at the transmission peak can be expressed as follows [58]:

$$\lambda = \frac{1}{2}L_1 \text{Re}(n_{e1}) + \frac{1}{2}L_2 \text{Re}(n_{e2}) + L_3 \text{Re}(n_{e3}) \quad (4.1)$$

Here  $L_1$  is the length of the top surface section (air side) of a metal island,  $L_2$  the length of the bottom surface (substrate side), and  $L_3$  the height of metal side-walls, i.e., slit depth.  $n_{ei}$  ( $i=1, 2,$  or  $3$ ) is defined as the SP wave vector normalized by the free-space propagation constant  $k_0$ , and corresponds to the effective index of the metal/dielectric interface being considered. The effective index  $n_e$  is, in general, a complex number, having both propagation and attenuation components. In the case of Ag, SP wave vectors are propagation dominant in the visible to near-

infrared range. In this work with a submicron-period slit array, therefore, we neglect the imaginary part of the effective indices. Along the transverse direction, the SP fields evanescently extend into both metal and dielectric regions. The effective index value reflects the integral effects resulting from interactions of a plasmon wave with the media over the entire extension of the fields. Chemical modification of each metal surface is expected to alter the effective index  $n_{ei}$  in that section, by an amount commensurate with the change in the plasmonic fields in the dielectric ambient, causing a resonant wavelength shift. The dispersion property of materials (especially the wavelength dependence of metal's dielectric function) in conjunction with a spectral shift also contributes to the effective index change. Taking into account these two contributing factors and also the fact that chemical modification was made on the top surface of metal ( $L_1$ ) and the side walls of slits ( $L_3$ ), but not on the quartz/metal interface ( $L_2$ ), we can express the total wavelength shift as follows.

$$\Delta\lambda = \frac{\frac{1}{2}L_1\left(\frac{dn_{e1}}{d\varepsilon_d}\right)\Delta\varepsilon_d + L_3\left(\frac{dn_{e3}}{d\varepsilon_d}\right)\Delta\varepsilon_d}{1 - \frac{1}{2}L_1\left(\frac{dn_{e1}}{d\lambda}\right) - L_3\left(\frac{dn_{e3}}{d\lambda}\right)} \quad (4.2)$$

The effective index changes caused by chemical modification are expected to be different for the top surface of a metal island and the slit sidewalls. Hence they will show different sensitivities to an adsorbed analyte layer, because of the different distribution of plasmonic fields along the transverse direction. To find the effective index change for the top surface section, we model it as a planar metal/dielectric interface with semi-infinite extension of dielectric. The effective index for SPs on that surface can be expressed as  $n_{e1} = [(\varepsilon_m\varepsilon_d)/(\varepsilon_m + \varepsilon_d)]^{1/2}$ , and the

dispersion term  $(dn_{e1}/d\lambda)$  is determined as  $(1/2)n_{e1}^3 \varepsilon_m^{-2} (d\varepsilon_m/d\lambda)$ . Imagine that an analyte layer of thickness  $d$  and dielectric constant  $\varepsilon_a$  is adsorbed on the metal surface. Assume that the analyte layer thickness is much smaller than the plasmon field extension (i.e., the penetration depth in dielectric). The SP effective index change caused by analyte adsorption,  $(dn_{e1}/d\varepsilon_d)\Delta\varepsilon_d$  can be expressed as:

$$\left(\frac{dn_{e1}}{d\varepsilon_d}\right)\Delta\varepsilon_d = \frac{\pi |\varepsilon_m|^{3/2} \varepsilon_d^{1/2}}{\lambda (\varepsilon_m + \varepsilon_d)^2} \left(1 - \frac{\varepsilon_d}{\varepsilon_a}\right) d \quad (4.3)$$

$\Delta\varepsilon_d$  is determined from a formula that equates the total amount of polarization charge change induced by analyte adsorption to that with a uniform increment of ambient dielectric constant:

$$\int_0^\infty \varepsilon_0 (\tilde{E} - E) dz = \int_0^\infty \Delta\varepsilon_d \varepsilon_0 E dz . \quad \varepsilon_0 \text{ is the free-space permittivity. } E \text{ and } \tilde{E} \text{ are the electric fields}$$

(the normal component to the metal surface) in the dielectric region before and after analyte adsorption, respectively. The electric field in the analyte layer is  $(\varepsilon_d / \varepsilon_a)$  times the electric field in the ambient dielectric and assumed to be constant across the analyte layer thickness,  $d$ .

Assuming negligible perturbation of the fields outside the analyte region,  $\Delta\varepsilon_d$  is calculated as

$$d\gamma_d(1 - \varepsilon_d)/\varepsilon_a . \quad \gamma_d \text{ is the decay constant in the ambient dielectric and is expressed as}$$

$$k_0 n_{e1} \varepsilon_d^{1/2} |\varepsilon_m|^{-1/2} .$$

The index change in the slit requires more development. In the case of a metal slit of width  $w$ , propagation of a plasmon wave along the slit is governed by the following dispersion relation [63,64]:

$$\frac{\gamma_m}{\varepsilon_m} + \frac{\gamma_d}{\varepsilon_d} \frac{1 - e^{-\gamma_d w}}{1 + e^{-\gamma_d w}} = 0 \quad (4.4)$$

Here,  $\gamma_d = (k_{sp}^2 - \varepsilon_d k_0^2)^{1/2} = k_0(n_{e3}^2 - \varepsilon_d)^{1/2}$  is the decay constant of plasmon fields inside the slit region, and describes the evanescent profile in the dielectric gap. The decay constant in the metal region, given by  $\gamma_m = (k_{sp}^2 - \varepsilon_m k_0^2)^{1/2} = k_0(n_{e3}^2 - \varepsilon_m)^{1/2}$ , determines the penetration depth in metal. Figure 4.4 (a) shows the effective index  $n_{e3}$  (both the real and imaginary parts) calculated for a silver nanoslit with air gap by solving the dispersion relation at three different wavelengths, 450, 650, and 800 nm. As assumed before, the imaginary part remains small compared to the real part so that SP attenuation would be insignificant for the slit dimensions being considered. The effective index monotonically increases as the slit width decreases. For the case of a 40 nm slit width, the effective index is calculated to be 1.5 at 650 nm. Figure 4.4 (b) shows the  $E_x$  field distribution (the  $E$ -field component normal to metal surface) calculated for the same slit structure. Note that the electric field at the dielectric side of the interface is  $|\varepsilon_m/\varepsilon_d|$  times greater than that at the metal. The field remains nearly constant across the gap region, whereas it quickly decays in the metal with a penetration depth of  $\sim 30$  nm. For narrow slits ( $\gamma_d w \ll 1$ ), the dispersion relation can be simplified as follows:

$$\frac{\gamma_m}{\varepsilon_m} + \frac{\gamma_d}{\varepsilon_d} \frac{\gamma_d w}{2} = 0 \quad (4.5)$$

Taking differentiation of Equation (4.5) with respect to  $\lambda$ , we obtain an expression for  $(dn_{e3}/d\lambda)$  as follows.

$$\frac{dn_{e3}}{d\lambda} = \frac{k_0^2 \varepsilon_d \left( \frac{d\varepsilon_m}{d\lambda} - \frac{k_0}{\pi} \varepsilon_m \right) + \frac{d\varepsilon_m}{d\lambda} \gamma_m \gamma_d^2 w - \frac{k_0^3}{\pi} \varepsilon_m \varepsilon_d \gamma_m w}{2n_{e3} k_0^2 (\varepsilon_d + \varepsilon_m \gamma_m w)} + \frac{n_{e3} k_0}{2\pi} \quad (4.6)$$

The effective index change induced by analyte adsorption can be expressed as  $(dn_{e3}/d\varepsilon_d)\Delta\varepsilon_d$ .  $\Delta\varepsilon_d$  represents the change of dielectric ambient in the slit region caused by adsorption of analytes on slit walls. For the case of analytes of dielectric constant  $\varepsilon_a$  and thickness  $d$  on each sidewall,  $\Delta\varepsilon_d$  can be expressed as  $2(\varepsilon_a - \varepsilon_d)(\varepsilon_d/\varepsilon_a)(d/w)$ .  $\Delta\varepsilon_d$  is determined from a formula that equates the total amount of polarization charge change induced by analyte adsorption to that with a uniform increment of ambient dielectric constant in the gap region:

$$\int_0^w \varepsilon_0 (\tilde{E} - E) dx = \int_0^w \Delta\varepsilon_d \varepsilon_0 E dx. \quad \text{The electric field } E \text{ is assumed to be constant in the gap region.}$$

$dn_{e3}/d\varepsilon_d$  can be derived from the dispersion relation, Equation (4.5), by taking differentiation of the equation with respect to  $\varepsilon_d$ . Combining the two, the effective index change in the slit region can be expressed as,

$$\left( \frac{dn_{e3}}{d\varepsilon_d} \right) \Delta\varepsilon_d = \frac{1}{n_{e3}} \left( \frac{\frac{1}{2} k_0 \varepsilon_m w - (n_{e3}^2 - \varepsilon_m)^{1/2}}{k_0 \varepsilon_m w + \varepsilon_d (n_{e3}^2 - \varepsilon_m)^{-1/2}} \right) \left( 1 - \frac{\varepsilon_d}{\varepsilon_a} \right) \frac{2d}{w} \quad (4.7)$$

Given these expressions for the effective index changes and the dispersion effects, we can calculate the wavelength shift from the different regions. Calculation shows that the dispersion effect on the top surface of metal is negligible, i.e.,  $L_1(dn_{e1}/d\lambda) \ll 1$ , in the first term of the denominator of Equation (4.2). Substituting  $(dn_{e1}/d\varepsilon_d)\Delta\varepsilon_d$  in Equation (4.2) with the expression

in Equation (4.3), and  $(dn_{e3}/d\lambda)$  in Equation (4.2) with Equation (4.6), we can calculate the wavelength shift of the transmission peak caused by analyte adsorption on the top surface of the metal. Similarly substituting  $(dn_{e3}/d\varepsilon_d)\Delta\varepsilon_d$  in Equation (4.2) with Equation (4.7), we can calculate the wavelength shift caused by adsorption in the slit region. Equations (4.6) and (4.7) involve the effective index in the slit region,  $n_{e3}$ , and we obtain its value referring to Figure 4.4 (a), which shows  $n_{e3}$  values calculated for a broad range of slit width. For the given structure and materials system characterized in this work, we assume  $L_1 = 300$  nm,  $L_3 = 150$  nm,  $w = 40$  nm,  $\lambda = 680$  nm,  $d = 1.5$  nm,  $\varepsilon_a = 2.1$ ,  $\varepsilon_d = 1.0$ ,  $\varepsilon_m = -19.1 + i1.2$ , and  $d\varepsilon_m/d\lambda = -0.068$  [65]. Calculation shows that the slit region contributes 13 nm to the wavelength shift of the transmission peak while the top surface contributes 0.3 nm to the shift. The total shift of 13.3 nm calculated from this formula is in reasonable agreement with the measurement (11 nm) shown in Figure 4.2. The analysis clearly reveals that the slit region provides efficient transduction of ambient index change into a spectral shift of optical transmission, while the planar top surface of metal makes a very minor contribution. Sensitivity of this nano-slit-based SPR sensing can be further enhanced by reducing the slit width (Equation (4.7)) and/or by increasing the slit depth (Equation (4.2)). Figure 4.5 shows the sensitivity calculated at 680 nm wavelength for different slit width of a Ag nanoslit array (with grating period of 360 nm and slit depth of 190 nm). Here the sensitivity is defined as the ratio of the wavelength shift to the analyte layer thickness. In this calculation, the analyte layer's dielectric constant is assumed to be 2.1, and the gap ambient is either air ( $\varepsilon_d = 1.0$ ) or water ( $\varepsilon_d = 1.77$ ).

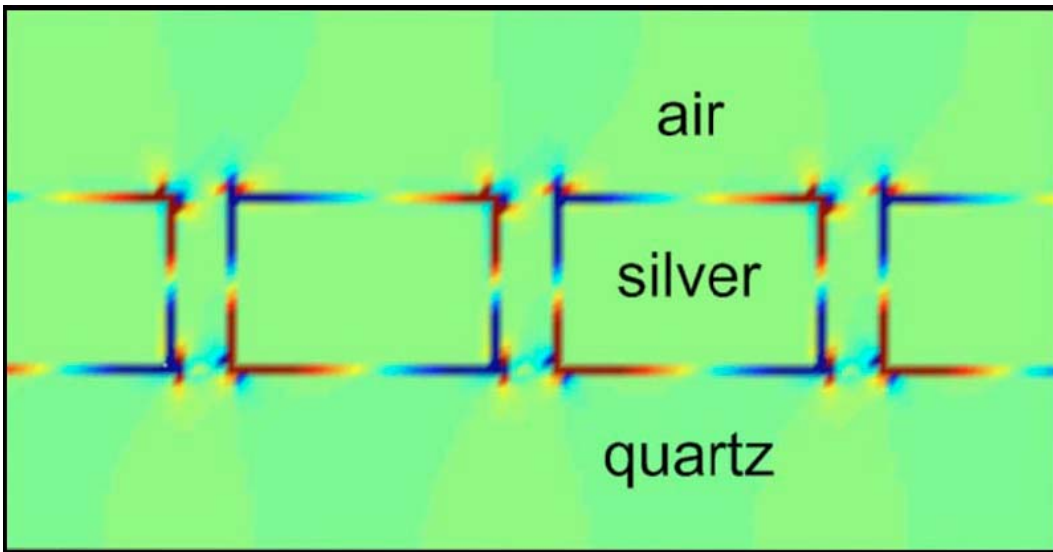


**Figure 4.3** Surface plasmon polarization charge distribution on a silver nanoslit array (370 nm period, 180 nm thickness, and 80 nm slit width) calculated with the finite-difference time-domain (FDTD) analysis at 650 nm wavelength, which corresponds to the peak transmission point.

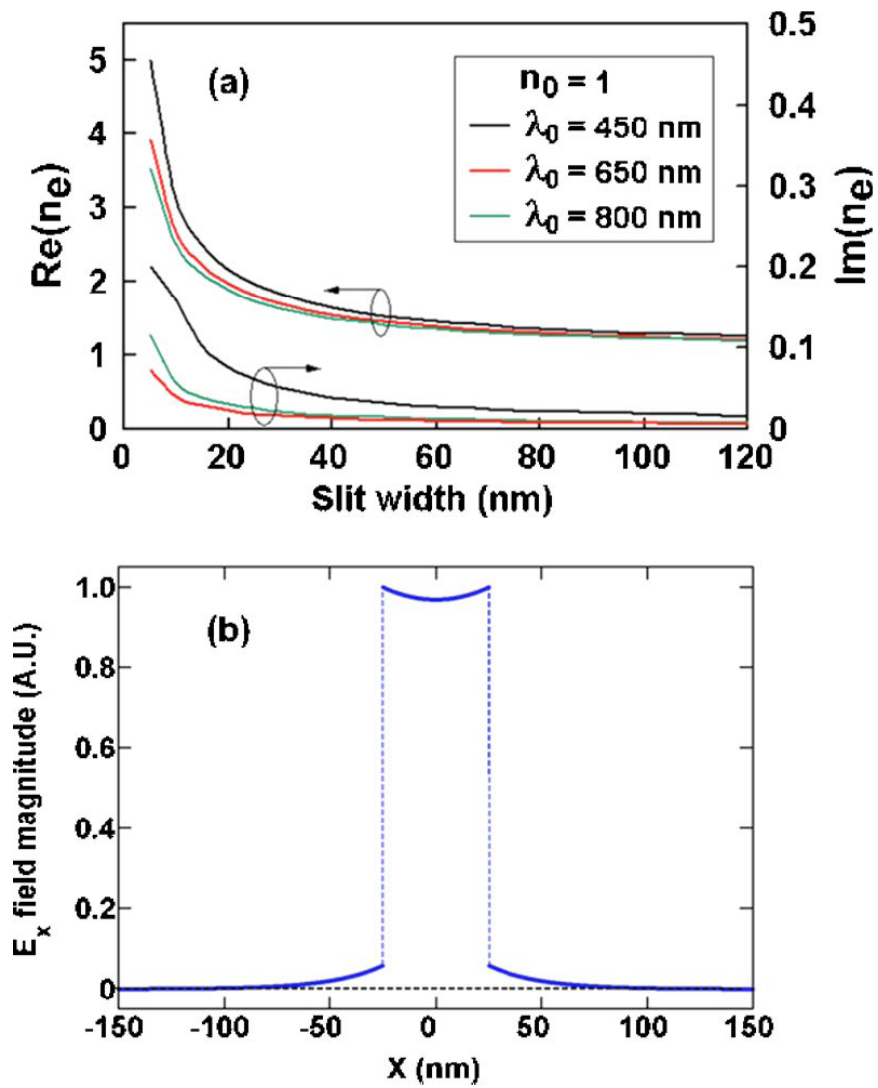


**Figure 4.4** (a) SP effective index  $n_e$  in a silver nanoslit with air gap calculated at 450, 650, and 800 nm wavelengths for various different slit widths: Both the real and imaginary parts are shown. (b)  $E_x$  field distribution (the  $E$ -field component normal to metal surface) calculated for a Ag slit with 50-nm air gap at 650 nm wavelength.

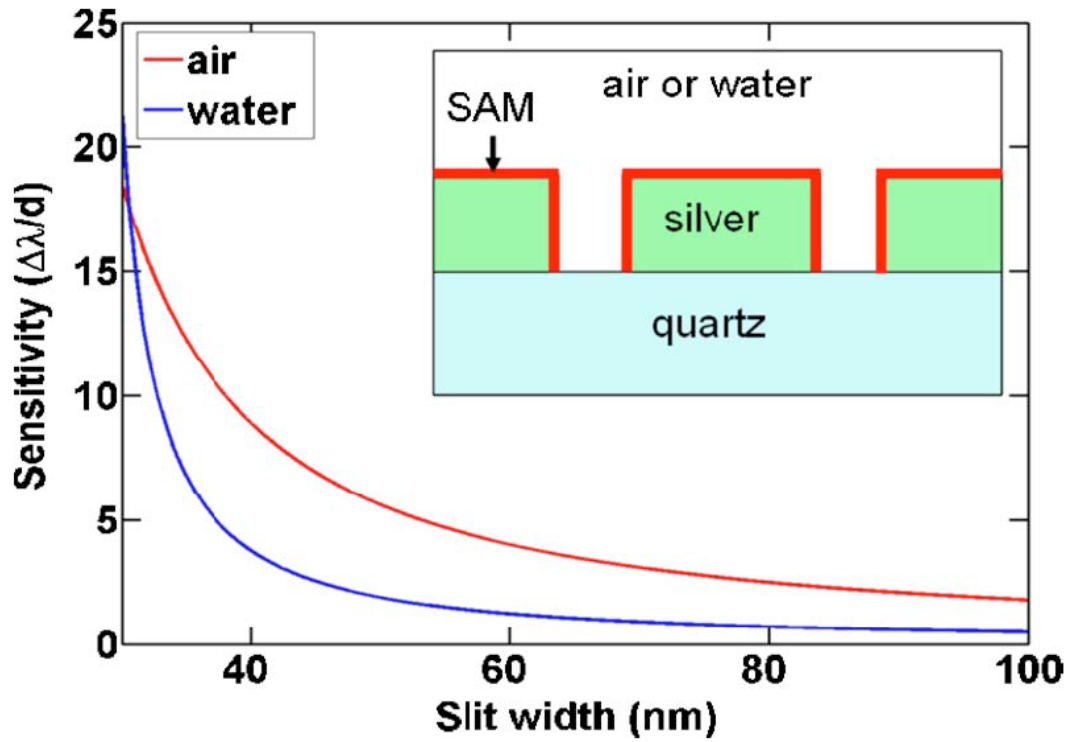


**Figure 4.5** Sensitivity calculated at 680 nm wavelength for different slit width of a silver nanoslit array (grating period of 360 nm and slit depth of 190nm). The gap ambient is assumed to be either air ( $\epsilon_d = 1.0$ ) or water ( $\epsilon_d = 1.77$ ). The sensitivity is defined as a ratio of the amount of wavelength shift to the analyte layer thickness. The analyte layer's dielectric constant  $\epsilon_a$  is assumed to be 2.1.

#### 4.4 SUMMARY

Nano-slit-array-based SPR sensing offers greater flexibility than nano-hole-array-based SPR sensing. In the latter case, the hole diameter cannot be designed too small and/or the hole depth cannot be increased too high, otherwise an extremely poor transmission will result because of cutoff wavelength of waveguide modes. A related and alternative approach to utilizing highly confined plasmonic fields for SPR sensing has also been reported. Instead of confining plasmonic fields into a physically defined region (i.e., the narrow slits), nano-particles are used to confine the evanescent field region in the dielectric. Depending on the particle size, the field extension can be made as small as 10 ~ 20 nm, and high sensitivity SPR sensing has been reported with nano-particle-based structures. In summary, chemical modification of nanostructured metal surfaces that allow nanoscale confinement of plasmonic fields is a promising approach to developing a new class of SPR sensors that will enable high sensitivity sensing and extremely small miniaturization of SPR devices.

## 5.0 BLUE-SHIFT OF SURFACE PLASMON RESONANCE IN A METAL NANOSLIT ARRAY STRUCTURE

### 5.1 INTRODUCTION

Anomalous dispersion ( $dn/d\omega < 0$ ) of light in dispersive media has drawn particular interest because it causes a number of counter-intuitive phenomena [66,67]. The group velocity ( $v_g = c/[n + \omega(dn/d\omega)]$ ) of a light pulse, for example, can exceed the speed of light or even be negative if the dispersion is sufficiently steep ( $\omega|dn/d\omega| > n$ ). Anomalous dispersion usually implies strong absorption of light (evident from the Kramers-Kronig relations), and the opacity of conventional passive media renders the study of such phenomena difficult. By contrast, an atomic resonance can display a steep dispersion even with modest absorption, providing a ‘transparent’ anomalous dispersive medium over narrow frequency ranges. Since the first observation of superluminal propagation based on excitonic absorption in a solid-state medium, most experiments have exploited atomic gaseous media involving gain doublets or electromagnetically induced absorption [68-71].

Surface plasmons (SPs) offer an interesting avenue for studying phenomena that involve anomalous dispersion in the optical frequency range. An example of particular interest is organic monolayer assemblies containing dye molecules [72-75]. The coupling of excitonic states of dye molecules to the surface plasmons is known to cause an anomalous dispersion of

the surface-bound waves. While the anomalous dispersion originates from the dye layer's resonant absorption, we also note that the surface plasmons on a planar interface without any adsorbed layer (i.e., SPs on the metal/air interface) show an anomalous behavior around its intrinsic resonance wavelength. In contrast to these conventional assemblies, this work studies the interaction of light with a metal nanoslit structure that can excite plasmon waves traveling on the metal surface, for which the dispersion can accumulate throughout the propagation [76,77]. Because surface plasmons can decouple into free-space radiation via nanoscale features on the metal surface, these near-field phenomena of the metal surface can affect the far-field radiation. In addition, the SPs' dispersion characteristic is affected by altering the dielectric environment near the interface [72-79]. This serves as an important basis for surface plasmon resonance (SPR) spectroscopy, which is commonly used in sensing and monitoring molecular adsorption on a metal surface.

This study investigates how the transmission spectra of nanostructured metal films depend on the interactions of surface plasmons in a dispersive resonant-cavity structure. In these structures (see Figure 5.1), the surface of individual metal stripes of a nanoslit array is treated as a cavity and the metal stripes periphery is used to define the cavity length, hence the resonance condition. In this work the surface plasmon dispersion characteristics are altered by use of thin dielectric layers that do not have resonant absorption bands in the spectral range of interest but modify the dispersion characteristics of the cavity such that a net negative dispersion occurs in the wavelength range of the cavity resonance. Two different dielectric materials are used for this purpose: 1) a high-index dielectric layer (amorphous Si; ~10 nm thickness) that is used to shift the anomalous dispersion regime to a desired spectral range and to reduce the attenuation loss in the SP resonance band, and 2) a monolayer organic film (thiol-based self-assembled monolayer;

~1.5 nm thickness) that is designed to alter the effective index of surface plasmons without modifying the dispersion profile. The latter material would correspond to an analyte layer when the array operates as a sensor. In this work, we show that the interplay of anomalous dispersion and cavity resonance can cause a blue-shift of the optical transmission with adsorption of a non-absorbing monolayer on the array surface.

This chapter is structured as follows. First we show that the transmission peak through a nanoslit array corresponds to the quadrupolar resonance of surface plasmons on the periphery of an individual metal stripe. Using this insight, a simple model is developed to predict the wavelength shift and its sign. Next we use this model to predict how a high-index, thin dielectric layer between the metal and substrate can alter the surface-plasmon dispersion characteristic and we compare these predictions with experiments.

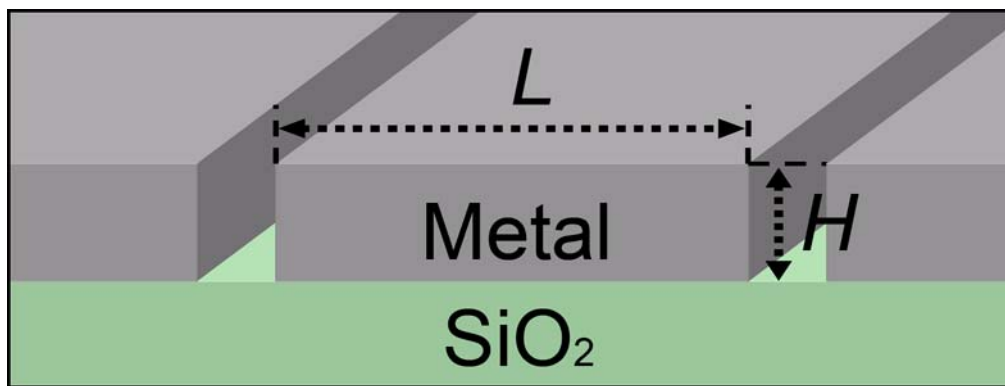


**Figure 5.1** This figure shows a side view of two nanoslits in a metal film (thickness  $H$ ) on a quartz ( $\text{SiO}_2$ ) substrate. The two slits define a metal slab in the center which has a thickness  $H$ , a width  $L$ , and is 'infinitely' long in the other dimension. This metal slab, or island, provides a resonant cavity for surface plasmons about its periphery.

## 5.2 CAVITY RESONANCE OF SURFACE PLASMONS IN METAL NANOSLIT ARRAYS

Being a surface-bound wave at a metal/dielectric interface, a surface plasmon's dispersion characteristics are governed by the dielectric response of both the metal and the dielectric  $\epsilon_d$ . The dielectric response of noble metals  $\epsilon_m(\omega)$  in the optical frequency range are mainly determined by two types of transitions, one within the conduction band (as described by the Drude model of free electrons) and the other involving interband transitions (bound-electron contributions, modeled with Lorentzian oscillators) [80,81].

$$\epsilon_m(\omega) = 1 - \frac{\omega_{pe}^2}{\omega^2 + i\gamma_e\omega} + \sum_j \frac{\omega_{pj}^2}{\omega_j^2 - \omega^2 - i\gamma_j\omega} \quad (5.1)$$

where  $\omega_{pe}$  and  $\gamma_e$  are the characteristic frequency and damping rate for the Drude electron response and  $\omega_{pj}$  and  $\gamma_j$  are the frequency and damping rate for the transition  $j$ . The thresholds for direct excitation of  $d$ -band electrons to the conduction band are in the UV/visible range (3.9, 2.4, or 2.1 eV for Ag, Au, or Cu, respectively). The interband transitions have a major influence on plasmon energies, shifting the volume (bulk) plasmon frequency ( $\omega_p$ ) from 9 eV - 12 eV (the value estimated from the free-electron only model) to 2 eV - 4 eV range (close to the  $d$ -band transition energies). For a metal of finite extent and juxtaposed with a dielectric, another type of plasmon, called a surface plasmon, can be supported at the metal/dielectric interface. Surface plasmons are a divergence-free ( $\nabla \cdot D = 0$ ) transverse electromagnetic mode associated with charge density oscillations at the interface. The resonance condition of this surface-bound wave

is sensitive to the size and geometry of the metal and its surrounding dielectric. In the case of a planar metal/dielectric interface, SPs experience a medium with an effective dielectric constant,  $\varepsilon_m \varepsilon_d / (\varepsilon_m + \varepsilon_d)$ , and the surface plasmon resonance frequency  $\omega_{sp}$  is determined from the condition,  $\varepsilon_m(\omega_{sp}) + \varepsilon_d(\omega_{sp}) = 0$  [80]. The presence of the dielectric material causes the SP resonance frequency ( $\omega_{sp}$ ) to be red-shifted from that of the bulk plasmon frequency ( $\omega_p$ ). In general,  $\varepsilon_m$  is a complex quantity and a resonance feature is observed at the frequency where  $|\varepsilon_m(\omega) + \varepsilon_d(\omega)|$  displays a minimum. The SP resonance gives rise to anomalous dispersion and an accompanying strong absorption, a characteristic signature that can be predicted from the Lorentz oscillator model associated with the interband transitions [Equation (5.1)]. This work considers how the SP dispersion characteristic is modified by introducing a high-index, thin dielectric layer between the metal and substrate; the findings show that the attenuation loss is significantly reduced (for longer interaction lengths on the metal surface) and the anomalous dispersion regime is broadened and shifted to longer wavelength.

Consider a single, rectangular metallic stripe (of length  $L$  and thickness  $H$ ) within a larger grating structure, that is, a nanoslit array structure (Figure 5.1). From the perspective of a surface plasmon wave propagating on the metal surface, sharp discontinuities exist at the corners of the rectangular stripe and they can form the fixed points of standing waves. For example, one could envision a standing wave associated with just the top (or bottom) face of the metal and having zeroes for the charge displacement at the corners. Assuming narrow slits (i.e.,  $L \sim$  grating period), a resonance condition can be derived for such a mode, namely

$$m\lambda_0 \approx N_{top(bottom)}L \quad (5.2)$$

where  $\lambda_0$  is the wavelength of the incident light,  $N_{top(bottom)}$  is the effective index, and  $m$  is an integer [82-84]. By approximating the top (bottom) face as an isolated, single interface, we can write the effective index as

$$N_{top(bottom)} \approx \sqrt{\frac{\epsilon_m \epsilon_{d,top(bottom)}}{\epsilon_m + \epsilon_{d,top(bottom)}}} \quad (5.3)$$

Likewise, a resonant mode that is associated with the stripe periphery exists when the SP's round-trip phase shift is equal to  $2\pi m$ , or equivalently when the following phase matching condition is met,

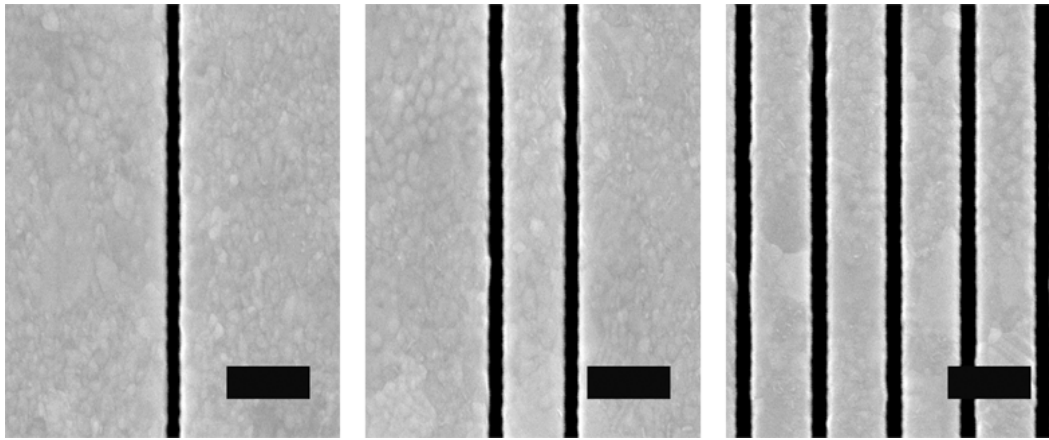
$$m\lambda_0 = (N_{top} + N_{bottom})L + 2N_{slit}H \quad (5.4)$$

The quantity  $N_{slit}$  is the effective index of surface plasmons in the slit region, and it can be calculated from the dispersion relation of a slit waveguide structure [85]. It has been proposed that a quadrupolar ( $m = 2$ ) resonant mode occurs at the peak transmission of light in this type of slit array structure [77]. We note that the phase accumulation over SP propagation on a metal surface plays an essential role for the resonance condition, and this fact is distinctly different from the conventional localized-SP-resonance case; the latter occurs in the quasi-static regime, for which the physical size of metal islands (or particles) is significantly smaller than the wavelength and therefore the phase retardation effect across the island is negligible [80,86].

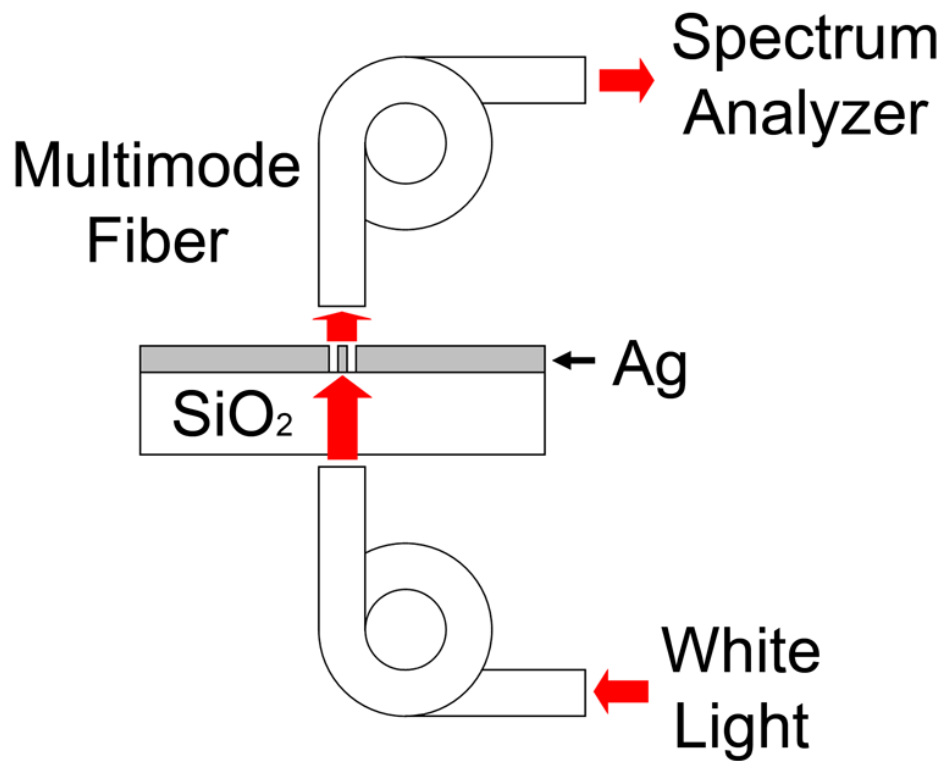
In order to verify the resonant interaction of surface plasmons with individual metal stripes, we have fabricated a Ag nanoslit array structure whose slit number varies from 1 to 10

(Figure 5.2 (a)). First a 100-nm-thick Ag layer was deposited on a fused silica substrate by thermal evaporation of Ag. Single nanoslit and 2-to-10-slit arrays (90-nm slit width and 500  $\mu\text{m}$  length) were formed in the Ag layer using a focused-ion-beam etching technique (Seiko SMI-3050-SE dual beam system: 30-keV Ga ion beam; 10-pA beam current). The typical etch depth for the nanoslits was 200 nm. The grating period of 2-to-10-slit arrays was 450 nm. The optical transmission through the slit arrays was measured in the spectral range of 350 ~ 1750 nm. A beam from a multimode fiber (core diameter of 62.5  $\mu\text{m}$  and a numerical aperture of 0.20) that was connected to an unpolarized white light source (Ando AQ-4303B) was normally incident to a slit array from the silica substrate side. The zero-order transmission through a slit array was collected with another multimode fiber placed close to the Ag layer surface ( $< 1 \mu\text{m}$  gap), and was characterized with an optical spectrum analyzer (Ando AQ-6315A) (Figure 5.2 (b)). The measured optical transmission spectra clearly reveal a passband in the visible range for the case of arrays with two or more slits, whereas the single slit structure does not show any such peak profile (Figure 5.3). Since a metal stripe is physically defined by two slits, the distinctly different transmission spectra from the single slit versus two- or more- slit arrays can be understood to arise from the SP resonance localized on an individual stripe. The sharpening of the transmission with the number of slits results from the interaction between the metal islands and the period of the slit structure, analogous to that observed for annular aperture arrays [87]. The peak transmission occurs at fixed wavelength (620-640 nm), independent of the number of slits (for 2 or greater). The measured peak position shows good agreement with the resonant wavelength ( $\sim 610$  nm) estimated from the quadrupolar resonance condition [ $m = 2$  in Equation (5.4)] [88].

In order to substantiate the correspondence of quadrupolar resonance and peak transmission, a finite-difference time-domain (FDTD) calculation was performed for the nanoslit array structure. Figure 5.4 shows the SP polarization charge distribution calculated at the peak transmission wavelength. The calculation was performed in a  $2\ \mu\text{m} \times 3\ \mu\text{m}$  region centered on the double-slit (divided up into a mesh with a 2.5-nm square grid spacing), with absorbing perfectly-matched-layer (PML) boundary conditions [91]. A 650-nm wavelength plane wave was excited at the top– the ‘air’/metal interface and propagated through the slits and the silica substrate. After roughly twice the time required for the wave to propagate across the metal stripe of thickness  $H$  the polarization charge distribution on the double slit appeared to be in steady state – oscillating with a roughly quadrupolar distribution, as shown. The SP polarization’s charge distribution that is obtained by a finite-difference time-domain (FDTD) calculation for this peak transmission wavelength clearly confirms the quadrupolar nature of the resonance (see Figure 5.4). It is interesting to note that the antinodes of the SP charge distribution are located around the slit corners for both the entrance and the exit sides of the structure. The dipolar nature of the resonance’s charge displacement on each side of the metal island likely facilitates both the SP excitation (at the entrance side) and decoupling into free-space radiation (at the exit side). This SP distribution enables maximum transmission of incident light through the nanoslit.



(a)



(b)

**Figure 5.2** (a) SEM images of three different slit arrays that were fabricated by focused-ion beam etching (1 slit, 2 slits, and 5 slits) are shown. The scale bar is 500 nm. (b) A schematic diagram for the method used to measure the transmission spectra is shown.

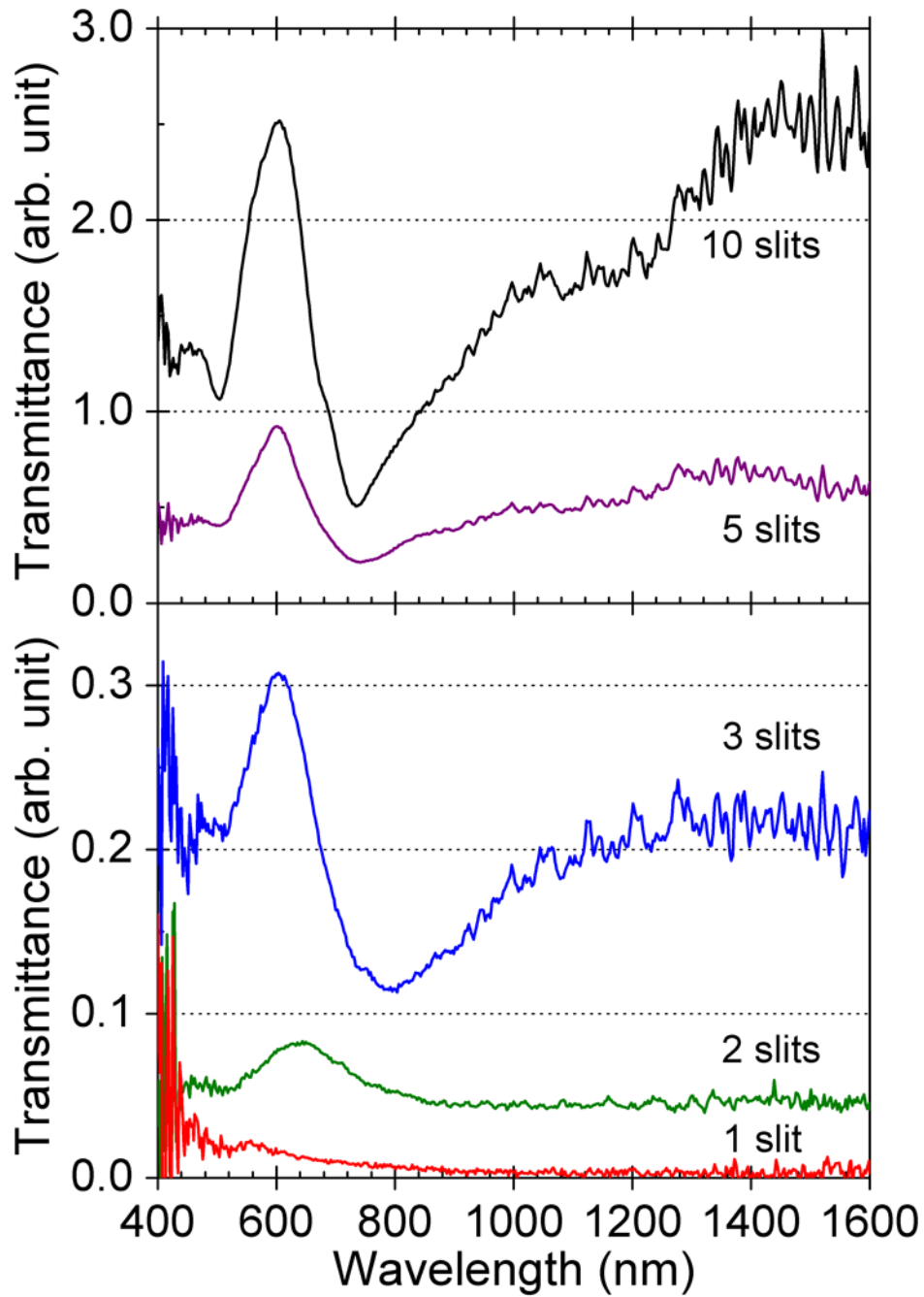


**Figure 5.3** Transmission spectra of Ag nanoslit arrays (slit width: 90 nm; grating period: 450 nm; Ag thickness: 100 nm). The number of slits varies from 1, 2, 3, 5 to 10.

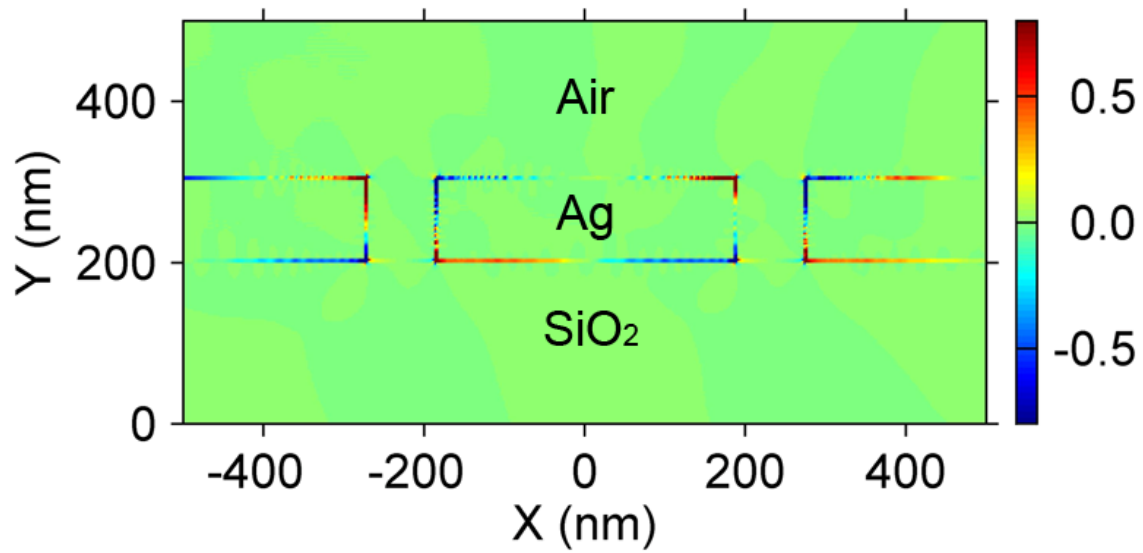


**Figure 5.4** The image shows the charge distribution for a resonant surface plasmon polarization, as calculated by FDTD for a 2-slit structure. A quadrupolar resonance is observed along the periphery of the metal island at the peak transmission wavelength.

### 5.3 MODELING OF SURFACE-PLASMON DISPERSION AND RESONANCE

Here we develop a simple model to account for the shift in the resonance wavelength of a metal slit array with a change in the ambient's dielectric constant. Suppose that a transmission peak of a grating structure is caused by a particular SP resonance and consider the wavelength shift  $\delta\lambda_0$  that is caused by a small modification of the metal surface, such as adding a self-assembled monolayer (SAM) whose dielectric constant is different from the ambient dielectric on the top surface and/or slit wall surface of the metal islands [92]. To account for the wavelength dependence,  $\lambda_0$ , of the metal's dielectric constant and the dependence on the ambient's dielectric constant,  $\varepsilon_d$ , we write the effective index as a function of  $\lambda_0$  and  $\varepsilon_d$ :  $N(\lambda_0, \varepsilon_d)$ . A simple variational analysis on Equation (5.4) yields:

$$m \cdot \delta\lambda_0 = \left[ \left( \frac{\partial N_{top}}{\partial \lambda_0} + \frac{\partial N_{bottom}}{\partial \lambda_0} \right) \mathbf{L} + 2 \frac{\partial N_{slit}}{\partial \lambda_0} \mathbf{H} \right] \cdot \delta\lambda_0 + \left( \frac{\partial N_{top}}{\partial \varepsilon_{d,top}} \right) \mathbf{L} \cdot \delta\varepsilon_{d,top} + 2 \left( \frac{\partial N_{slit}}{\partial \varepsilon_{d,slit}} \right) \mathbf{H} \cdot \delta\varepsilon_{d,slit} \quad (5.5)$$

For the case of quadrupolar resonance ( $m = 2$ ), the following expression is obtained for the wavelength shift:

$$\delta\lambda_0 = \frac{\frac{1}{2} \left( \frac{\partial N_{top}}{\partial \varepsilon_{d,top}} \right) \mathbf{L} \cdot \delta\varepsilon_{d,top} + \left( \frac{\partial N_{slit}}{\partial \varepsilon_{d,slit}} \right) \mathbf{H} \cdot \delta\varepsilon_{d,slit}}{1 - \left( \frac{\partial N_{slit}}{\partial \lambda_0} \right) \mathbf{H} - \left( \frac{\partial N_{top}}{\partial \lambda_0} + \frac{\partial N_{bottom}}{\partial \lambda_0} \right) \frac{\mathbf{L}}{2}} \quad (5.6)$$

Here  $\delta\epsilon_{d,top}$  and  $\delta\epsilon_{d,slit}$  indicate the change in the effective dielectric constant of SPs (on the top surface of a metal stripe and in the slit (or wall) region, respectively) that arises from the surface modification. It is assumed that the bottom surface of the metal island is supported by a dielectric substrate (e.g., quartz) and the surface modification is made only on the top surface or in the slit region. Consequently, the effective index of SPs on the bottom surface can be changed only via the dispersion effect ( $\partial N / \partial \lambda_0$ ) induced by a resonant wavelength shift. Equation (5.6) can be recast in terms of the propagation constant  $\beta (= 2\pi N(\lambda_0, \epsilon_d) / \lambda_0)$  rather than the effective index to obtain

$$\delta\lambda_0 = - \frac{\frac{1}{2} \left( \frac{\partial\beta_{top}}{\partial\epsilon_{d,top}} \right) L \cdot \delta\epsilon_{d,top} + \left( \frac{\partial\beta_{slit}}{\partial\epsilon_{d,slit}} \right) H \cdot \delta\epsilon_{d,slit}}{\frac{\partial\beta_{slit}}{\partial\lambda_0} H + \left( \frac{\partial\beta_{top}}{\partial\lambda_0} + \frac{\partial\beta_{bottom}}{\partial\lambda_0} \right) \frac{L}{2}} \quad (5.7)$$

Equations. (5.6) and (5.7) can be shown to be identical by way of the following relations:

$$\frac{\partial\beta}{\partial\epsilon_d} = \frac{2\pi}{\lambda_0} \frac{\partial N}{\partial\epsilon_d}, \quad \frac{\partial\beta}{\partial\lambda_0} = \frac{2\pi}{\lambda_0} \left( \frac{\partial N}{\partial\lambda_0} - \frac{N}{\lambda_0} \right),$$

and the quadrupolar resonance condition [ $m = 2$  in Equation (5.4)]. The eigenvalue equation for SPs in the slit region is also used to find exact expressions for the partial derivatives in Equations. (5.6) and (5.7) [85].

The The wavelength shift in Equations. (5.6) and (5.7) can be either positive or negative. If dispersion effects are ignored, the denominator in Equation (5.6) becomes unity and we obtain the approximate relation,  $\delta\lambda_0 \approx \frac{1}{2} \left( \frac{\partial N_{top}}{\partial\epsilon_{d,top}} \right) L \cdot \delta\epsilon_{d,top} + \left( \frac{\partial N_{slit}}{\partial\epsilon_{d,slit}} \right) H \cdot \delta\epsilon_{d,slit}$ . In this limit, the total peak shift should be positive (i.e., a red-shift occurs) after adsorption of a SAM layer. This red-shift arises because the derivative of the effective index with respect to the dielectric constant on the

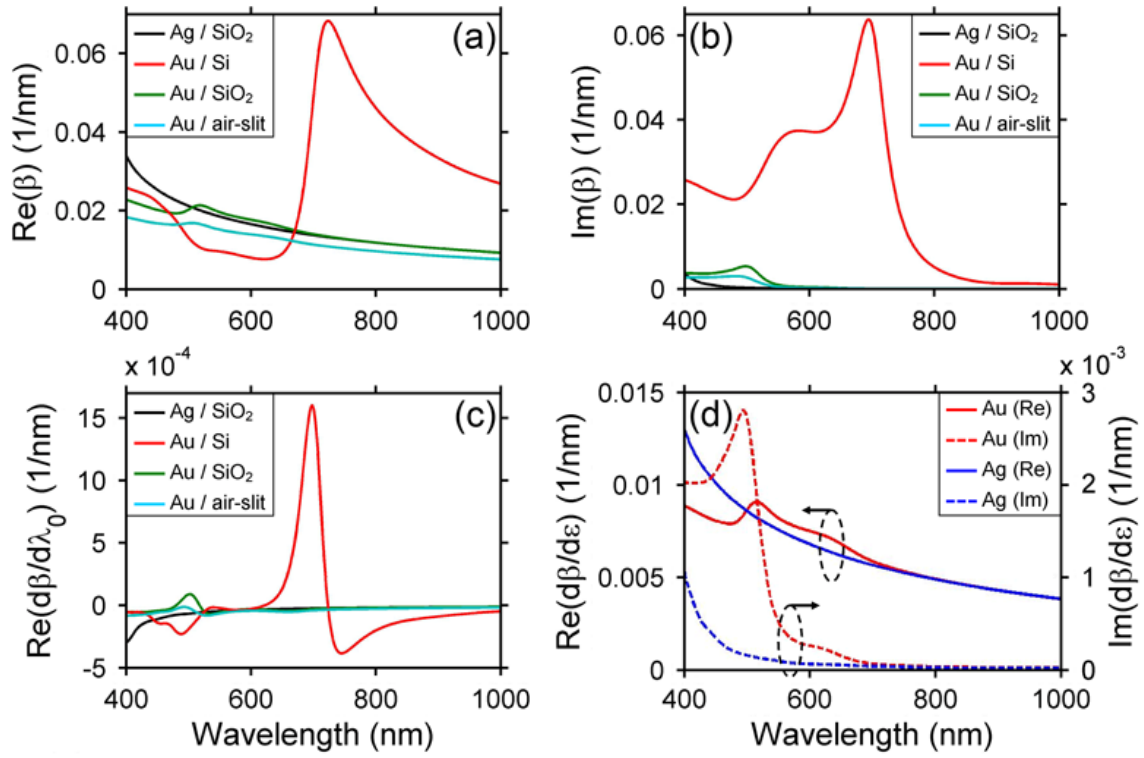
insulator side ( $\partial N/\partial \epsilon_d$ ) is positive, and the effective change in the dielectric constant on the insulator side ( $\delta \epsilon_d$ ) is also positive, assuming that the dielectric constant of the adsorbed SAM layer is higher than that of the ambient (e.g., air). In the case that all surfaces have normal dispersion ( $\partial N/\partial \lambda_0 < 0$ ), Equation (5.6) still predicts a red-shift. If some surface regions show anomalous dispersion ( $\partial N/\partial \lambda_0 > 0$ ) and those sections are sufficiently long, then the accumulation of the anomalous dispersion can dominate over the normal dispersion terms so that the denominator of Equation (5.6) becomes negative. The consequence would be a blue-shift that results from the surface modification. From Equation (5.7) the requirements for a blue-shift translate into the condition that some surfaces show  $\frac{\partial \beta}{\partial \lambda_0} = \frac{2\pi}{\lambda_0} \left( \frac{\partial N}{\partial \lambda_0} - \frac{N}{\lambda_0} \right) > 0$ , that is, anomalous dispersion of at least  $N/\lambda_0$  and a sufficient accumulation of phase. It is important to note that the cumulative nature of SP dispersion is intrinsic to the distributed resonant cavity structure studied here, and it enables one to observe dispersive behaviors even in the case of reasonably weak dispersive media.

The dispersion characteristics of SPs on a resonant structure like that defined in Figure 5.1 were further examined by the use of Equation (5.7) for the peak shift. The real and imaginary parts of the SP propagation constant and the relevant first-derivatives are plotted in Figure 4 for some different metal/dielectric interfaces: Ag or Au films in contact with air, SiO<sub>2</sub> or Si [93]. The SP resonance of the Ag/air interface occurs in the UV range, whereas the Au/SiO<sub>2</sub> interface and the Au/air slit show a resonance in the middle of the visible range (~510 nm) (Figure 5.5 (a)). Compared to the Ag case, the Au/air and Au/SiO<sub>2</sub> interfaces show a much reduced resonance. When juxtaposed with a high-dielectric-constant material (Si), however, the Au shows a dramatically enhanced resonance occurring at a significantly red-shifted location

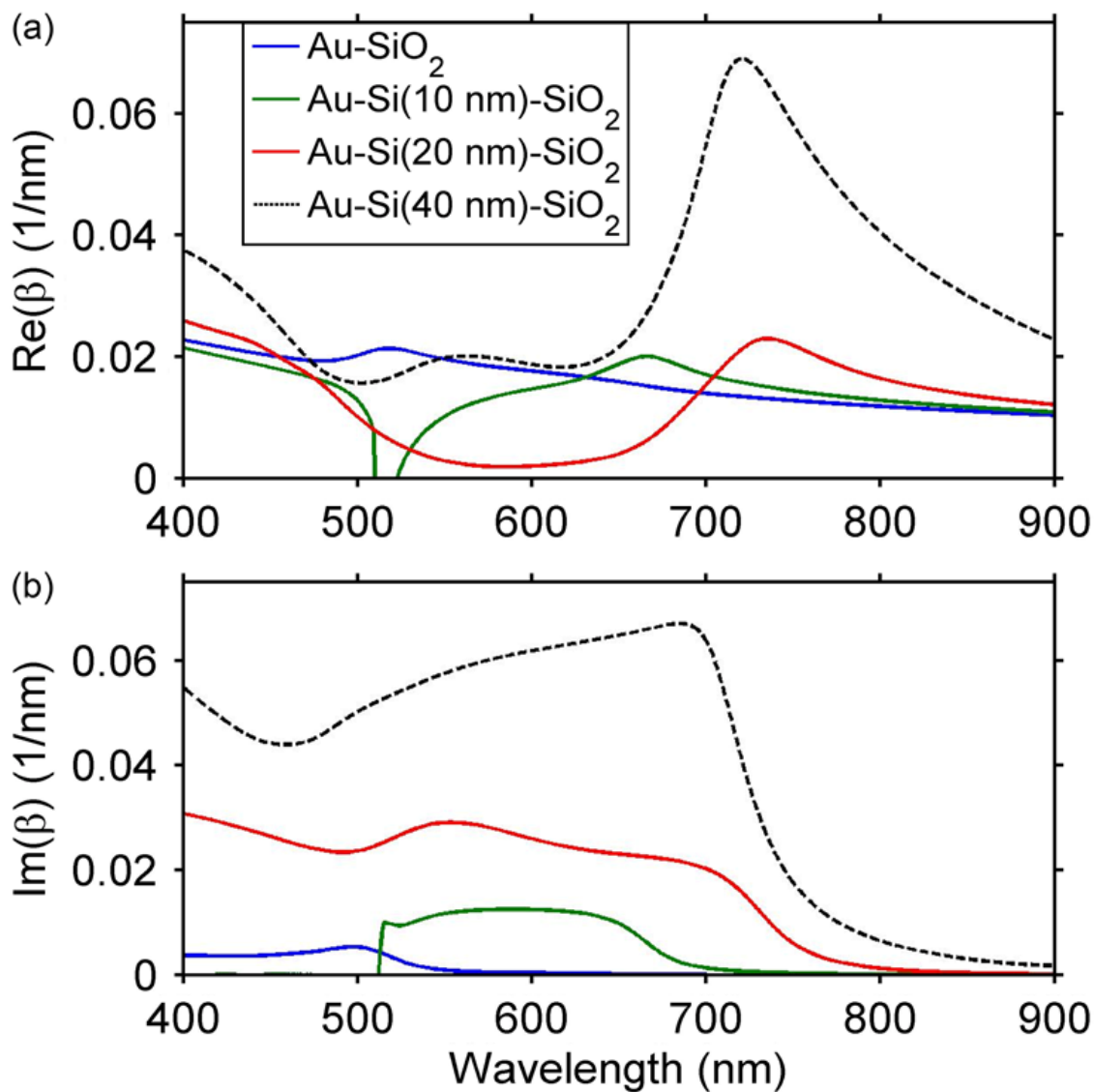
(~730 nm). This major change in dispersion characteristic is ascribed to the fact that the Au dielectric function has a relatively large imaginary part compared to its real part at around 500 nm, and this fact significantly changes in the longer wavelength region ( $\epsilon_{Au}$ :  $-4.1+i2.6$  at 510 nm and  $-18.9+i1.4$  at 730 nm).<sup>22</sup> In a narrow band around the SP resonance, the derivative of the propagation constant with respect to the free-space wavelength ( $\partial\beta/\partial\lambda_0$ ) becomes positive and shows peak values of  $1.8 \times 10^{-3} \text{ nm}^{-2}$  for Ag/SiO<sub>2</sub>,  $1 \times 10^{-4} \text{ nm}^{-2}$  for Au/SiO<sub>2</sub>, and  $1.5 \times 10^{-3} \text{ nm}^{-2}$  for the Au/Si interface (Figure 5.5 (c)). The derivative displays a much smaller negative value on the longer wavelength side of the band. The derivative of the propagation constant with respect to the ambient dielectric constant ( $\partial\beta/\partial\epsilon_d$ ) is positive for both the Au and Ag cases (Figure 5.5 (d)). Overall this analysis shows that the metal nanoslit array on a high-index substrate is a promising structure for observing a blue-shift of optical transmission in the visible/near-infrared spectral range, because the strong negative dispersion on the high-index metal/dielectric interface dominates over the positive dispersion on the metal/air interface. Here it should be noted that the above discussion assumes a lossless system, *i.e.*, dielectric functions that are purely real [all  $\gamma$ -terms in Equation (5.1) are zero]. Under this assumption, the SP resonant peak would be infinitely sharp, and the spectral shift (red or blue) as predicted by Equation (5.6) would show a singular behavior as the denominator approaches zero. In a system with loss, the resonance profile becomes less sharp, and the amount of peak shift remains finite.

Figure 5.5 shows that the Au/Si substrate exhibits a pronounced resonance in the visible wavelength region (500 – 800 nm). While the strong dispersion can easily satisfy the requirement for a blue-shift, it also incurs strong attenuation of the surface plasmon propagation. The imaginary part of the propagation constant at the Au/Si interface shows a peak value of  $0.06 \text{ nm}^{-1}$ , which corresponds to a propagation depth of ~17 nm (Figure 5.5 (b)). Considering the

dimension of the metal island (~200 nm), the lossy SPs on the island periphery are not expected to display a clear resonance. To achieve a reasonably-strong negative dispersion yet manage the loss, the Au grating structure was modified by placing a thin layer of amorphous silicon between the Au and silica substrate. Figure 5.6 shows the wavelength dependence of the propagation constant (both the real and imaginary parts) over a range of Si film thickness (0-40 nm). Consider the case of a Au grating on a 10-nm-thick Si layer that is deposited on a silica substrate. It is apparent from Figures 5.5 and 5.6 that the dispersion associated with the substrate-side of the interface will dominate over that on the air side. While the Au/SiO<sub>2</sub> and Au/Si exhibit anomalous dispersion only in a narrow spectral region around 500 nm and 700 nm, respectively, the effect of introducing a “composite” substrate acts to spread the anomalous dispersion over a much broader wavelength range. For example, a 10-nm-thick Si film gives a positive slope of the propagation constant from roughly 520 nm to 680 nm (Figure 5.6 (a): green curve), thereby enhancing the range of wavelengths over which a blue-shift can occur. Another important benefit of using this composite substrate is that the imaginary part of the SP propagation constant is now reduced to about 0.01 nm<sup>-1</sup> (Figure 5.6 (a): green curve), giving rise to a 100-nm propagation length. The observed dispersion-modification is mainly ascribed to the dielectric nature of the thin amorphous Si layer; its dielectric function does not exhibit any resonance absorption band in this spectral range, and its high-index low-loss nature (e.g., 17.3+i3.0 at 650 nm) is maintained. Rather, the thin layer dielectric shifts the SP resonance point (anomalous dispersion regime) to longer wavelength, according to the SP resonance condition discussed above, that is, at resonance  $|\varepsilon_m(\omega) + \varepsilon_d(\omega)|$  displays a minimum.



**Figure 5.5** The calculated wavelength dependence of the SP propagation constant ( $\beta$ ) is shown for various different interfaces [Ag/SiO<sub>2</sub>, Au/SiO<sub>2</sub>, Au/Si, and Au/air-slit(100-nm width)]. (a)  $\text{Re}(\beta)$ , (b)  $\text{Im}(\beta)$ , (c)  $\partial \text{Re}(\beta)/\partial \lambda_0$ , and (d)  $\partial \beta/\partial \epsilon_d$  (both the real and imaginary parts). In (a)-(c), black: Ag/SiO<sub>2</sub>; red: Au/Si; green: Au/SiO<sub>2</sub>; cyan: Au/air-slit. In (d), red: Au; blue: Ag; solid: real part; dashed: imaginary part. The dielectric functions of Ag, Au and SiO<sub>2</sub> are from Ref. [87].



**Figure 5.6** The calculated wavelength dependence of the SP propagation constant ( $\beta$ ) is shown for Au/Si/SiO<sub>2</sub> interfaces where the Si thickness ranges from 0, 10 nm, 20 nm to 40 nm. (a)  $\text{Re}(\beta)$  and (b)  $\text{Im}(\beta)$ .

## 5.4 CHARACTERIZATION OF DISPERSION-INDUCED BLUE-SHIFT OF SURFACE-PLASMON RESONANCE

Figure 5.7 shows the optical transmission spectra measured before and after a SAM layer (1.5-nm-thick alkanethiol film) treatment of the Ag or Au nanoslit array samples that were formed with various different substrate materials and structures: Ag/SiO<sub>2</sub>, Au/SiO<sub>2</sub>, Au/Ag(10-nm)/SiO<sub>2</sub>, and Au/Si(10-nm)/SiO<sub>2</sub>. For fabrication of large-number-slit arrays an electron beam lithography technique (JEOL 9300) was utilized in defining the one-dimensional grating patterns in an e-beam resist (PMMA) layer that is coated on Cr-deposited (30 nm thickness) fused silica substrates. A two-step plasma etching process was performed in order to transfer the e-beam-resist grating patterns onto the Cr layer and then onto fused silica using the Cr layer as an etch mask. The typical etch depth onto fused silica was 350 nm. A metal (Ag or Au) layer was angle-deposited on the mesa surface with thermal evaporation. Prior to this metal layer deposition, an amorphous silicon layer that goes in between the metal and substrate was deposited by radio-frequency magnetron sputtering of a silicon target. The Ag sample reveals a strong red-shift (20 - 30 nm) over the entire spectral range tested (550 - 850 nm) (Figure 5.7(a)).

This red-shift is expected, because the Ag surfaces (both the air and SiO<sub>2</sub> sides) show only normal dispersion in this spectral range (Figure 5.5). The Au/SiO<sub>2</sub> sample shows a tendency to blue-shift, but not that strong (Figure 5.7 (b)). This slight blue-shift is ascribed to the relatively-weak negative dispersion at the substrate-side interface with Au. The mild, negative dispersion of Au/SiO<sub>2</sub> is clearly confirmed when a thin (10-nm thick) Ag layer is introduced in between the Au and the SiO<sub>2</sub> substrate. The SP fields on the metal side are now mostly confined to the Ag layer, and therefore the dispersion on the bottom surface is mainly determined by the Ag/SiO<sub>2</sub> characteristic. Thus the overall dispersion is governed by

contributions from the Au/air and Ag/SiO<sub>2</sub>, which cancel each other (Figure 5.7 (c)). When the Ag is replaced with a thin layer (10-nm thickness) of Si, a clear blue-shift (~15 nm) is observed at around 600 - 700 nm (Figure 5.7 (d)). This reversal of spectral shift clearly confirms the negative dispersion of surface plasmons at the Au/Si/SiO<sub>2</sub> interface and their crucial role in the quadrupolar resonance along the metal stripe periphery.

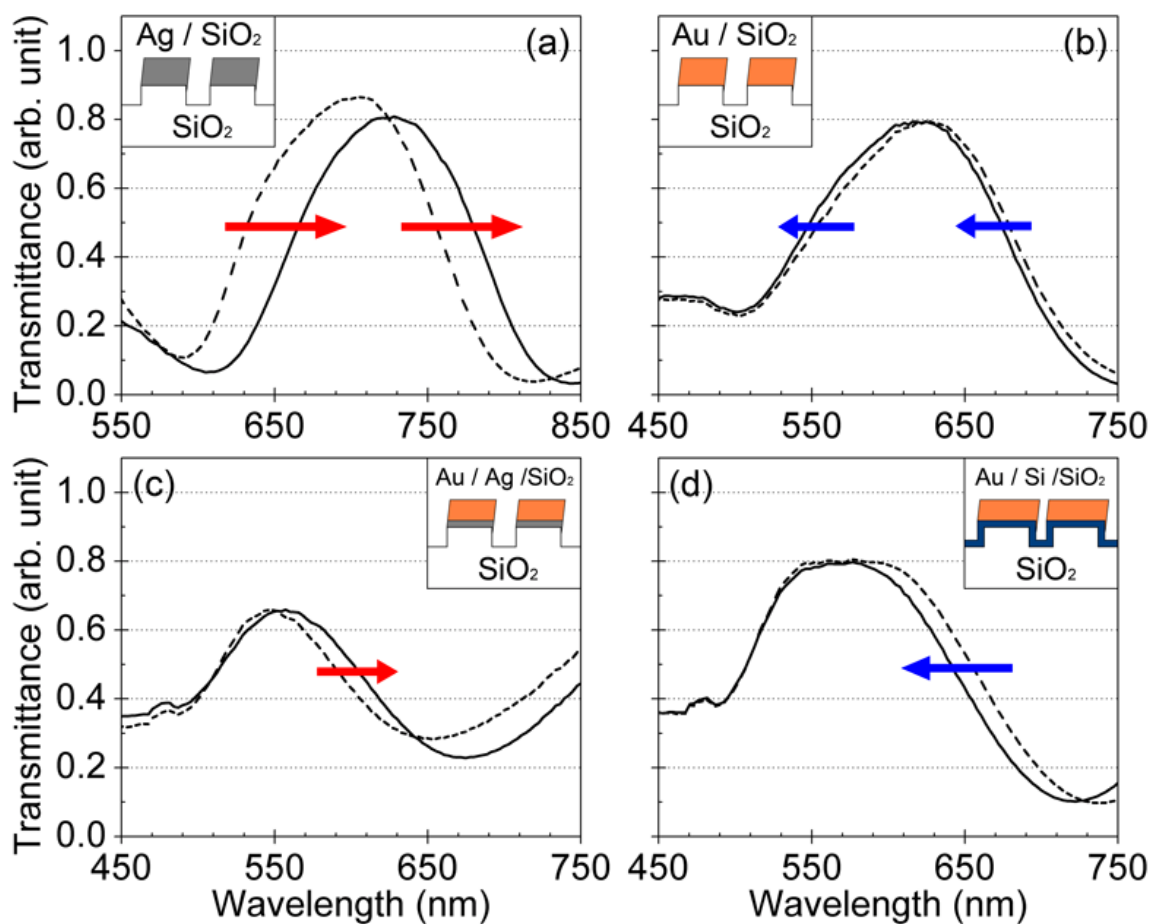


**Figure 5.7** Experimental transmission spectra of Ag or Au nanoslit arrays: dashed (before chemical modification of metal surface: adsorption of a SAM layer) and solid (after the modification). (a) Ag/SiO<sub>2</sub>, (b) Au/SiO<sub>2</sub>, (c) Au/Ag(10-nm thick)/SiO<sub>2</sub>, and (d) Au/Si(10-nm thick)/SiO<sub>2</sub>. Grating period: 370 nm for (a) and 300 nm for (b)-(d).

## 5.5 SUMMARY

We have investigated the anomalous behavior of surface plasmons that are excited in a resonant cavity structure of a metal nanoslit array. We show that the modification of a metal nanoslit array by a SAM film can give rise to either a red-shift or a blue-shift in the peak transmission wavelength. The sign of the wavelength shift depends on the surface-plasmon dispersion characteristics in the resonant cavity structure that corresponds to the stripe periphery of a nanoslit array, and they can be controlled by the composition of the metal film and the substrate that supports it. A simple model was developed to predict the wavelength shift and its sign. We show that the blue-shift of the transmission peak's wavelength, observed with adsorption of a SAM film on the metal surface, is caused by the interplay of anomalous dispersion and quadrupolar resonance of surface plasmons in the cavity structure.

## **6.0 NEAR- TO FAR-FIELD IMAGING OF FREE-SPACE AND SURFACE-BOUND WAVES EMANATING FROM A METAL NANOSLIT**

### **6.1 INTRODUCTION**

Transmission of light through a slit is a subject of study possessing a venerable history. Manifesting the wave nature of light through diffraction and/or interference, the subject research had made a major contribution to establishing a solid foundation of optics [94]. Recently there have been renewed interests in metal nanoapertures, primarily stimulated by the development of near-field scanning optical microscopy and an observation of extra-ordinary transmission of light through a metal nanoaperture array [95-98]. Despite the simple geometry, the radiation pattern of a metal nanoslit could be complicated by possible interactions of the radiation with screen material. For example, a metal surface responds to incident radiation by generating surface currents and charges [99]. Through this induction process, the metal surface can make a total reflection of the incident wave, as in the case of a perfect conductor. Through an exact balancing act between the incident and reflected waves, the tangential component of the electric field on the metal surface remains zero. As a result the cylindrical wavefronts emanating from the slit remain perpendicular on the metal surface. The degree of this perfection, however, depends on the metal's conductivity, i.e., dielectric constant [100]. The dielectric function of real metal is usually a complex number of finite value in the optical frequency range, and the metal surface

may even support tangential electric fields of non-negligible strength [101]. The electromagnetic wave emerging from a slit can also excite electron density fluctuations at the metal surface, i.e., a surface bound electromagnetic wave, called surface plasmon (SP) [102]. SPs behave differently from the free-space radiation component, and are expected to alter the diffraction pattern near the metal surface [103-106]. The finite size of slit width may also affect the radiation pattern, causing a deviation from that of an ideal line source.

Diffraction of light from a slit formed on an opaque screen can be understood by radiative propagation of the wavelets emanating from the aperture region, as explained by Huygens and Fresnel [107]. The radiation pattern of a slit with infinitesimally small width should show a uniform angular distribution of intensity with  $1/r$  radial dependence. While this simple picture well portrays the region far from the screen, the area close to it can be complicated by interactions of the screen material with the radiation from the slit [94]. Despite the recent advance in imaging optical fields, the overall picture of the radiation pattern emanating from a nanoaperture remains incomplete, mainly due to a lack of clear understanding of the transition between the near- and far-field regimes [103,108-111]. We report the radiation pattern (radial and angular distribution of light intensity) of a silver nanoslit measured in the near- to far-fields by linearly scanning a nanoapertured probe along the radial direction with the probe axis tilted parallel to the scan direction. In most of the far-field regime the  $1/r$  dependence is clearly observed. In the glancing angle regime, the radiation pattern is found to be significantly affected by the presence of surface plasmons, showing higher intensity closer to the metal surface. In the near- to intermediate regime where the finite aperture sizes of the slit and the probe have an effect of destructive interference, the intensity profiles fall off faster than the  $1/r$  dependence.

## 6.2 FABRICATION AND CHARACTERIZATION

### 6.2.1 Fabrication of single nanoslits using a focused-ion-beam etching technique

Figure 6.1 shows a scanning electron microscope (SEM) image of a 100-nm-wide single nanoslit formed in a 140-nm-thick Ag layer. Ag nanoslits were formed on a fused silica substrate (Corning 7980: 500  $\mu\text{m}$  thick; double-side polished). First, a 140-nm-thick Ag layer was deposited on the substrate by thermal evaporation of Ag (Alfar, 4N8 purity). Single nanoslit (100 nm width and 500  $\mu\text{m}$  length) was then formed in the Ag layer using a focused-ion-beam etching technique and the etching depth of a nanoslit was 170 nm. Seiko SMI-3050-SE dual beam system was used with Ga ion beam (beam current of 10 pA). Figure 6.2 is a schematic process flow of this technique.

### 6.2.2 Measurement setup

Figure 6.3 shows the intensity profile measurements setup using a nanoaperture probe. A nanoapertured fiber probe (Veeco Aurora NSOM probe 1720-00: 100-nm-thick Al coated; 80-nm diameter aperture; formed on a tapered, single-mode silica fiber with core diameter of 4  $\mu\text{m}$  and NA of 0.11; 1400  $\mu\text{m}$  total length of the tapered section coated with Al; full tapered angle of  $4^\circ$ ) was used in this work. Also, the probe transmission was characterized with a He-Ne laser (633 nm wavelength; 10 mW; 1 mm beam diameter; 1 mrad beam divergence). To characterize the angular dependence of transmission of a nanoapertured fiber probe itself, a TM- or TE-polarized laser light was directly incident to the nanoapertured probe with varying incidence angles in the range of  $-90^\circ$  to  $+90^\circ$  as shown in Figure 6.4 (a). In the case of the scanning probe

experiments, a TM-polarized laser beam was incident to the substrate side, and the radiation pattern from the nanoslit was scanned on the metal side using the nanoapertured probe. The probe output was measured with a photomultiplier tube (Hamamatsu H7468-20). The scanning probe experiments were carried out with a home-built scanning stage setup (PI E-621.1CD for nanopositioning and E-665.CR for servo control) interfaced with LabView 7.0 (National Instruments).

Figure 6.5 (a) shows the schematic drawing of the measurement scanned across a single nanoslit with the nanoprobe fiber aligned perpendicular to the substrate surface. The scan range used in this work was  $10\ \mu\text{m} \times 10\ \mu\text{m}$ , with a step size of 50 nm in the horizontal direction and 133 nm in the vertical direction. In another scan mode tested in this study, the probe axis was tilted to  $45^\circ$  and linearly scanned along the direction perpendicular to the probe axis at various different radial distances (Figure 6.6 (a)). Ideally a radiation pattern of a nanoslit can be directly obtained by making an angular scan at a fixed radial distance from the slit. From the instrumentation point of view, however, making angular scans at a sub-wavelength radial distance with nanometer scale precision is a challenging task. In this work, we have developed an alternative method to obtain nanoslit radiation patterns. The probe is linearly scanned along the radial direction in the near- to far-field region with the probe axis tilted parallel to the scan direction as shown in Figure 6.7.

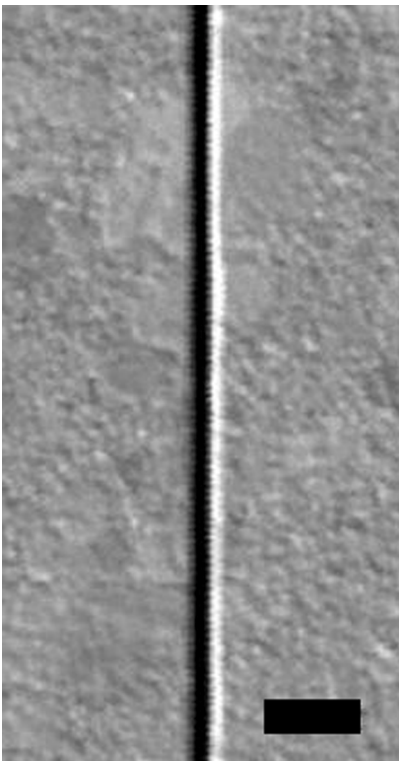
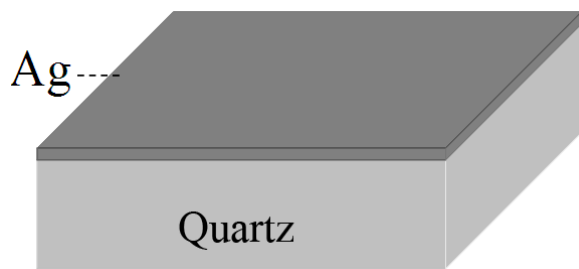
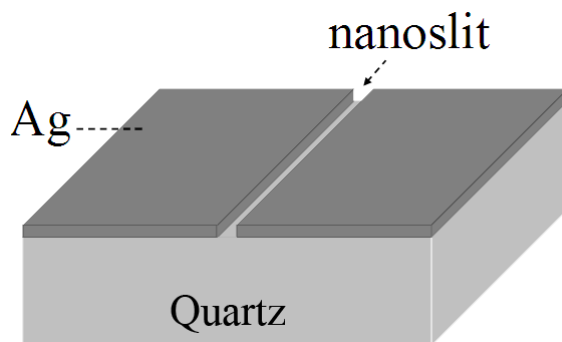


**Figure 6.1** SEM image (Top view) of a 100-nm-wide slit formed in a 140-nm-thick Ag layer deposited on a fused silica substrate using a focused-ion-beam etching technique (scale bar, 500 nm).



(a) Ag film deposition on planar quartz substrate with thermal evaporation



(b) Forming a single nanoslit on a quartz substrate using direct etching of Ag with a focused-ion-beam (FIB) system

**Figure 6.2** Schematic process flow of a single nanoslit formed in Ag layer. (a)-(b) in sequence.

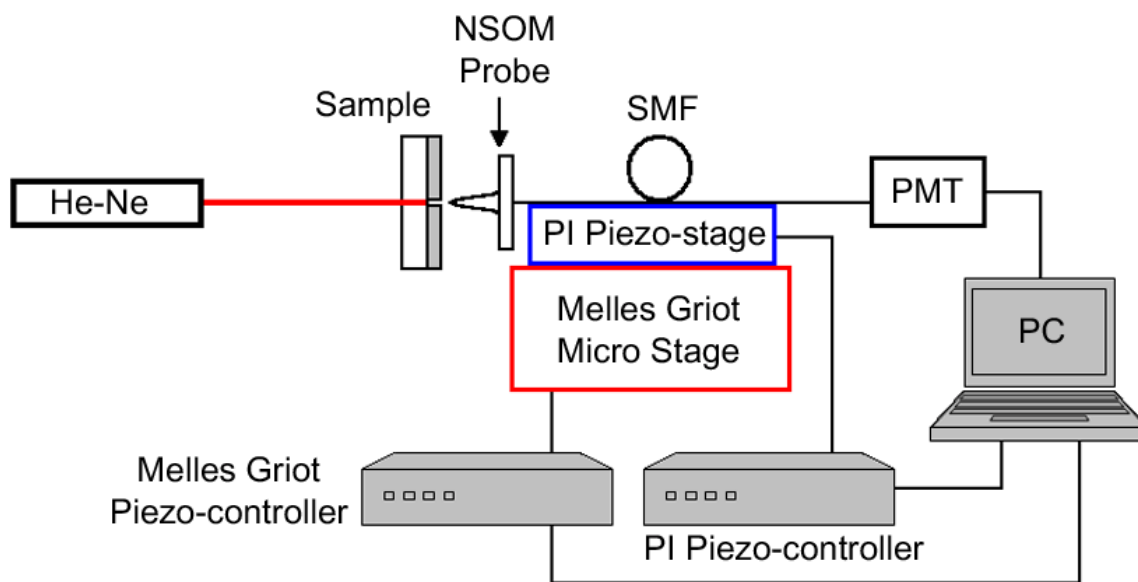
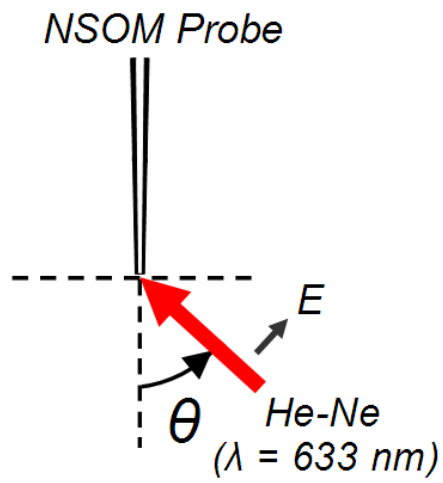
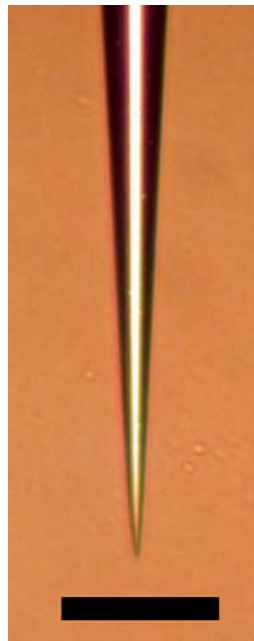


**Figure 6.3** Schematic of an optical transmission measurement setup using a scanning probe technique.

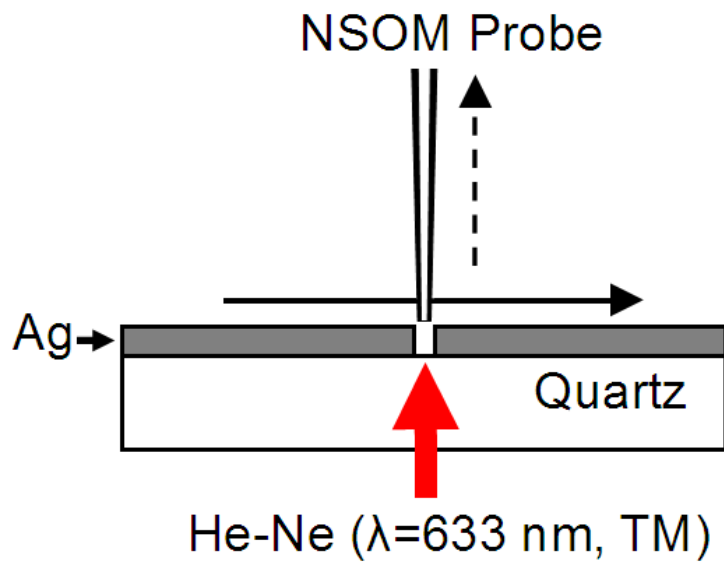


(a)

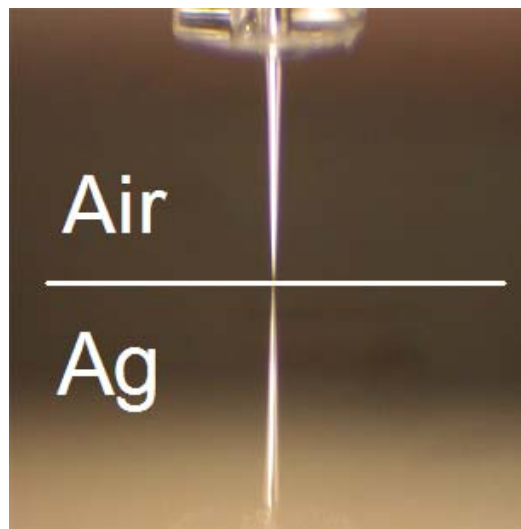


(b)

**Figure 6.4** The angular dependence of transmission of a nanoapertured fiber probe. (a) Schematic of measurement setup. (b) Microscopic image of nanoapertured probe (scale bar, 50  $\mu\text{m}$ ).

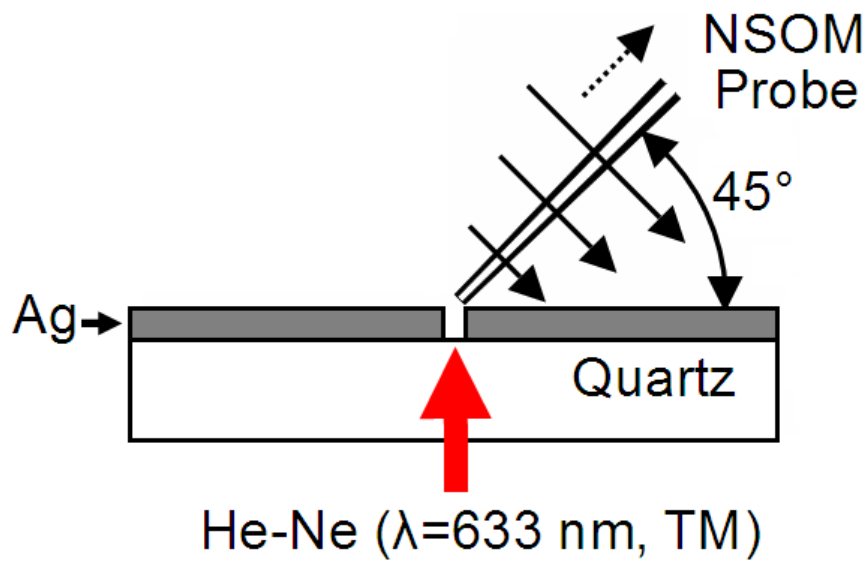


(a)

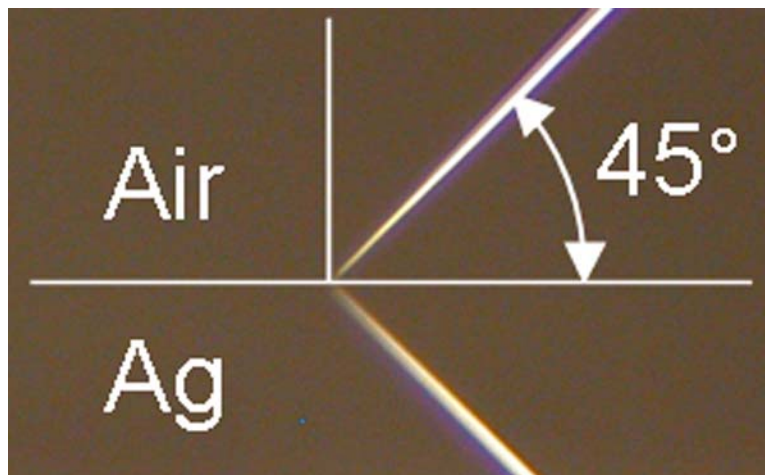


(b)

**Figure 6.5** The measurement scanned across a single nanoslit with the nanoprobe aligned perpendicular to the substrate surface. (a) Schematic drawing of the measurement setup. (b) A microscopic image of the nanoapertured probe aligned normal to metal surface (A mirror image of the probe is seen in the bottom side.).

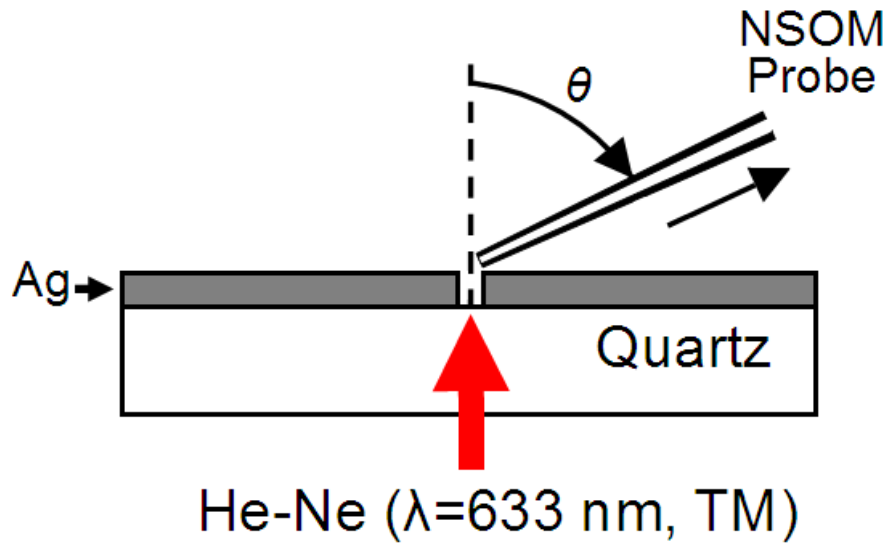


(a)

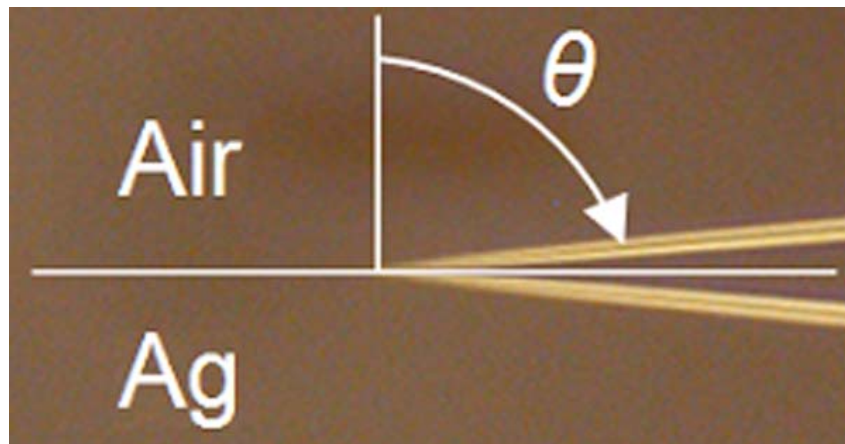


(b)

**Figure 6.6** The measurement scanned across a single nanoslit with the 45° tilted probe axis. (a) Schematic drawing of the measurement setup. (b) A microscopic image of a nanoprobe aligned close to metal surface with 45° tilt angle (A mirror image of the probe is seen in the bottom side.).



(a)



(b)

**Figure 6.7** Linearly scanned along the radial direction in the near- to far-field region with the probe axis tilted parallel to the scan direction. (a) Schematic drawing of the measurement setup. The probe tip is initially aligned close to a nanoslit with various tilt angles (0-85°) and is then scanned along the radial direction. (b) Microscopic image of the nanoapertured probe aligned close to metal surface with 85° tilt angle (A mirror image of the probe is seen in the bottom side.).

### 6.2.3 Characterization

One of the challenges in profiling radiation patterns with a near-field scanning optical microscope stems from the fact that most scanning probe systems are designed to make linear scans whereas radiation patterns are directly obtainable from the angular scans made at constant radial distances. When a probe makes a linear scan across an aperture, the incidence angle of light to the probe axis continuously varies. As the incidence angle deviates from zero (i.e., from normal incidence), the probe output falls off sharply even though the incident light intensity remains unchanged. This strong angular dependence of probe transmission hinders direct imaging of radiation patterns. In the present work a nanoapertured scanning probe technique was employed with a modified operating scheme such that a diffraction pattern (angular and radial dependence) of a nanoslit can be obtained at near- to far-fields without resorting to angular scans, without being governed by the probe's angular dependence.

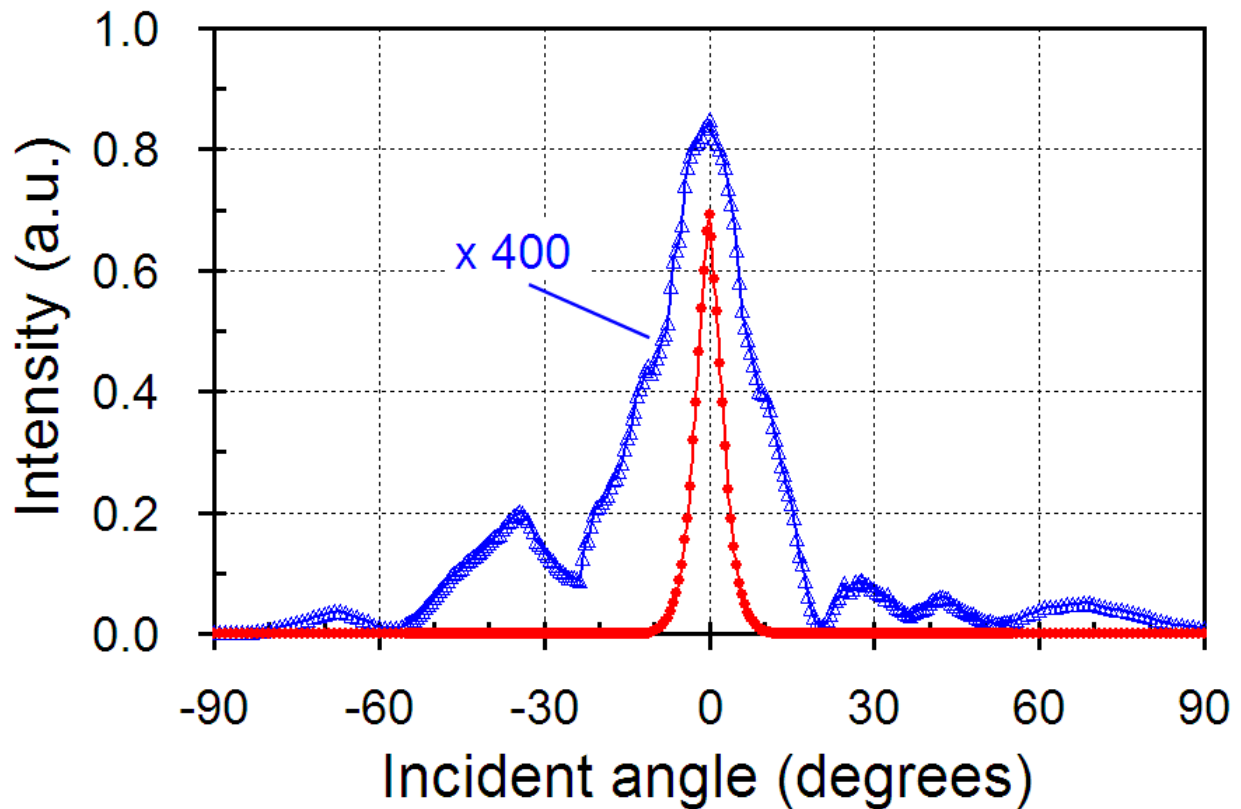
First we characterized the angular dependence of transmission of a nanoapertured fiber probe itself (80-nm diameter aperture, 100-nm-thick Al coated). A transverse magnetic (TM) polarized laser light was directly incident to the nanoapertured probe with varying incidence angles in the range of  $-90^\circ$  to  $+90^\circ$ . For a TM-polarized, 633-nm wavelength laser light (1-mm beam diameter and beam divergence of 1 mrad), the probe transmission shows the full-width-half-maximum (FWHM) of  $\sim 20$  degrees as shown in Figure 6.8. The probe functions via exciting surface plasmons at its aperture and subsequently coupling them into guided modes of the optical fiber through the tapered section [112].

Figure 6.9 shows the radiation intensity profiles scanned across a single nanoslit (a 100-nm-wide slit formed in a 140-nm-thick Ag layer deposited on a fused silica substrate) with the nanoprobe fiber aligned perpendicular to the substrate surface. A well-defined, single peak is

observed for each scan profile measured in the near- to far-field regime. The peak width (as measured with the base width) progressively increases from  $0.8 \mu\text{m}$  to  $3.5 \mu\text{m}$  for  $z = 0.13 \mu\text{m}$  to  $4.67 \mu\text{m}$ . When converted to the angular domain, the peak width converges to  $\sim 20^\circ$ . This well matches the angular profile of the probe transmission itself as shown in Figure 6.8. Figure 6.10 shows the scan profiles obtained for radiation angle of  $45^\circ$ . The probe axis was tilted to  $45^\circ$  and linearly scanned along the direction perpendicular to the probe axis at various different radial distances. Again all scanned profiles show a well-defined single peak centered at the  $45^\circ$  angular location. This clearly demonstrates that the scan profiles are predominantly governed by the probe characteristic itself, not by the radiation pattern being probed.

Ideally a radiation pattern of a nanoslit can be directly obtained by making an angular scan at a fixed radial distance from the slit. From the instrumentation point of view, however, making angular scans at a sub-wavelength radial distance with nanometer scale precision is a challenging task. In this work, we have performed an alternative method to obtain nanoslit radiation patterns. The probe is linearly scanned along the radial direction in the near- to far-field region with the probe axis tilted parallel to the scan direction (Figure 6.7). From these linear-scan profiles measured at various tilt angles, we compiled information of radiation patterns. Figure 6.11 (a) shows the log-log scale plots of the radial scan profiles ( $r = 0.13$  to  $9 \mu\text{m}$ ) obtained with tilt angles of  $0^\circ$ ,  $40^\circ$ , and  $85^\circ$ . The profiles show  $1/r$  dependence in the far-field region ( $r$ :  $2\text{-}9 \mu\text{m}$  for  $\theta = 0^\circ$ ,  $5\text{-}9 \mu\text{m}$  for  $\theta = 40^\circ$ , and  $0.8\text{-}2 \mu\text{m}$  for  $\theta = 85^\circ$ ), consistent with the cylindrical wavefronts expected from a line source. In the near- to intermediate region, the intensity significantly falls off from the inverse relationship. In the case of glancing angles (for example,  $\theta = 85^\circ$ ), the intensity in the far field is significantly higher than the inverse relationship. By mapping the linear-scan data onto polar coordinates, the angular dependence of

radiation was obtained at various different radial distances. Figure 6.11 (b) shows the radiation patterns compiled for radial distances,  $r = 0.13, 0.53, 1.07, 2.40, 3.47,$  and  $4.54 \mu\text{m}$ . The angular range covered in this work is 0 to 85 degrees. In the large angle regime (i.e., glancing angles), the radiation intensity consistently increases as the angle approaches  $90^\circ$ . Overall the radiation pattern shows a significant deviation from the simple picture, i.e., the  $1/r$  dependence with a uniform angular distribution.



**Figure 6.8** The incidence-angle dependence of the nanoapertured probe transmission. For a TM-polarized laser beam (633 nm wavelength) incident to the probe tip, the probe transmission shows strong angular dependence with an acceptance angle of approximately  $\pm 20$  degrees. Side lobes appear in the transmission characteristic, which is ascribed to the interference between different modes supported by the tapered section, a phenomenon known as Talbot effect [112,113]. The slight asymmetry observed with the transmission is ascribed to an irregular geometry that may be present at the probe tip. The transmission of the same single mode fiber as the probe but without a tapered section is also shown for comparison (red:  $\sim 400$  times stronger transmission than the nanoprobe's).

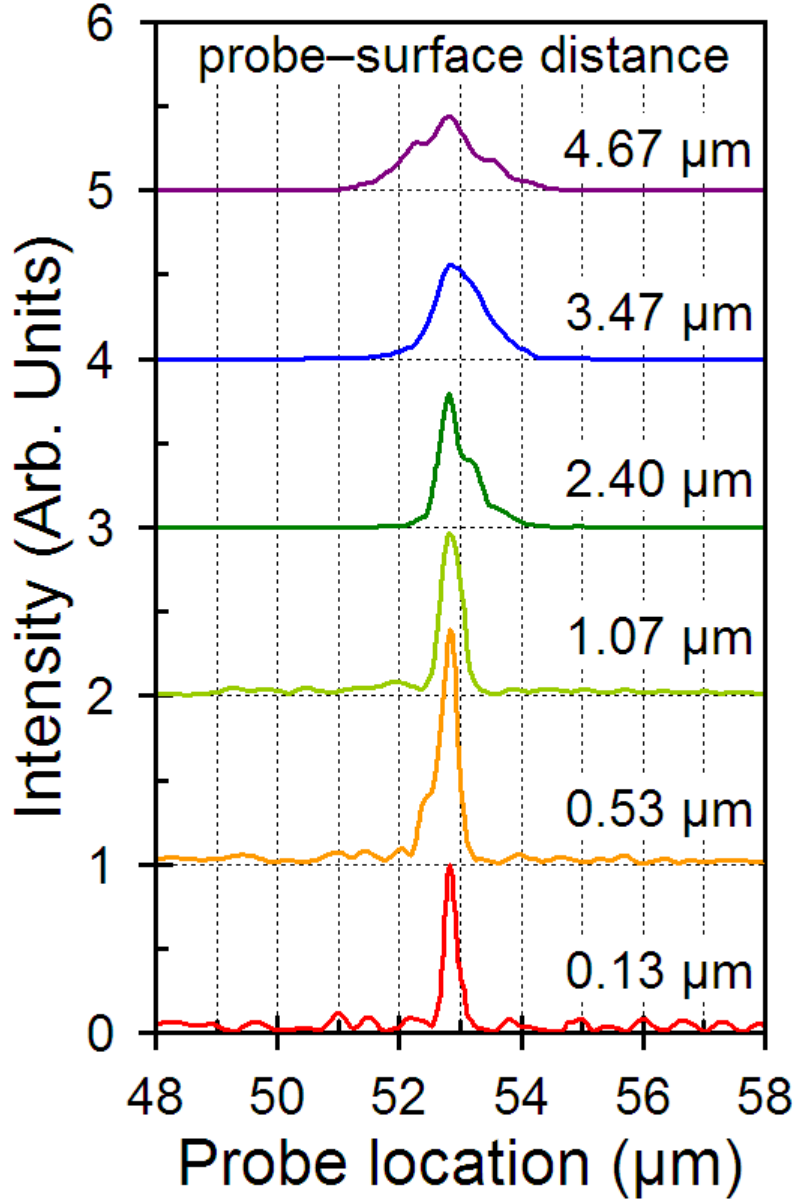


**Figure 6.9** Silver nanoslit radiation profiles scanned along the direction perpendicular to the probe axis. The probe was aligned normal to the substrate surface (Refer to Figure 6.5 (a) for the scan mode used in this characterization.). The scan profiles obtained at probe-metal distance of 0.13, 0.53, 1.07, 2.40, 3.47, and 4.67  $\mu\text{m}$  (bottom up). A single narrow peak is observed with increasing peak width for larger distance.

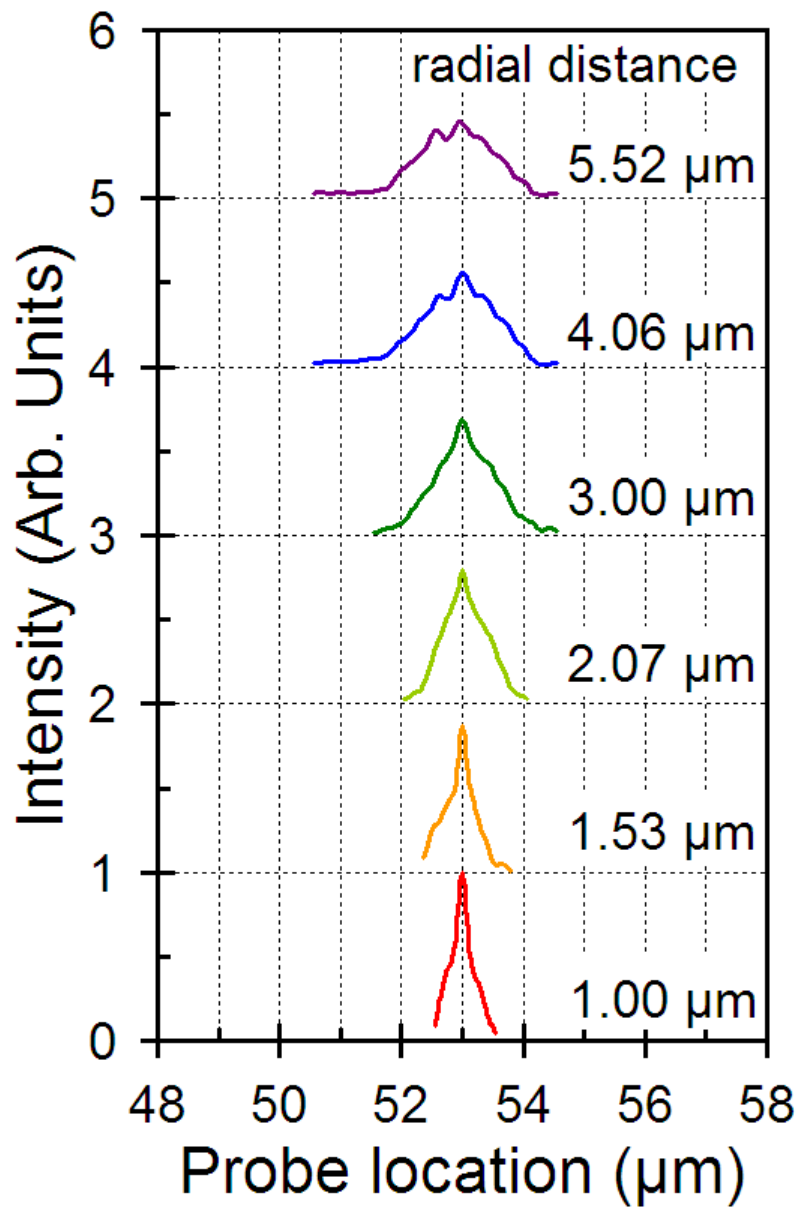
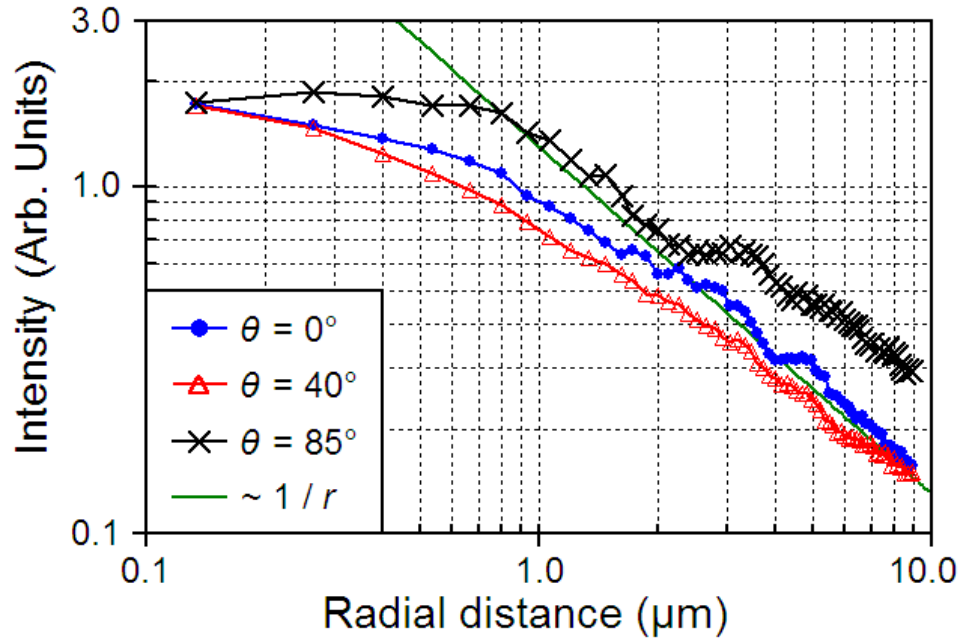
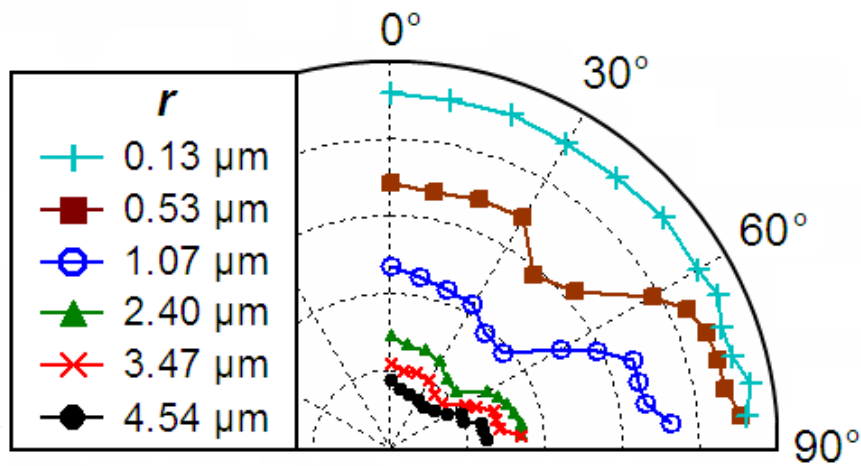


**Figure 6.10** Silver nanoslit radiation profiles scanned across a single nanoslit with the  $45^\circ$  tilted probe axis. The nanoprobe was aligned close to metal surface with  $45^\circ$  tilt angle (Refer to Figure 6.6 (a) for the scan mode used in this characterization.). The scan profiles obtained at probe-slit distance of 1.00, 1.53, 2.07, 3.00, 4.06, and 5.52  $\mu\text{m}$  (bottom up). A single narrow peak (with increasing peak width for larger distance) is observed.



(a)



(b)

**Figure 6.11** Radiation pattern of a silver nanoslit obtained with the probe linearly scanned along the radial direction (Refer to Figure 6.7 (a) for the scan mode used in this characterization.). (a) The log-log scale plots of the scanned profiles (intensity versus radial distance) for tilt angles of  $0^\circ$  (blue),  $40^\circ$  (red), and  $85^\circ$  (black). The  $1/r$  dependence expected from cylindrical wave propagation is shown for reference. (b) Radiation patterns plotted in polar coordinates: radial distances of 0.13, 0.53, 1.07, 2.40, 3.47, and 4.54  $\mu\text{m}$  (from outside).

### 6.3 RESULTS AND DISCUSSION

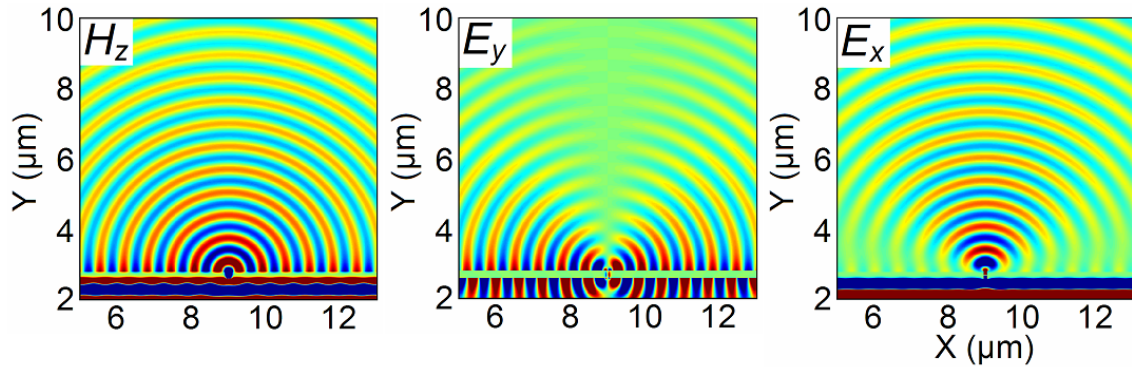
In order to substantiate these observations, a finite-difference time domain (FDTD) analysis was carried out on optical transmission through a nanoslit structure. Also, the FDTD results were generated using a 2D Yee mesh with 10 nm grid spacing and perfectly matched layer (PML) boundary conditions [114]. Figure 6.12 (a) shows the snap-shot images of optical fields (the horizontal magnetic field,  $H_z$ , the horizontal component of electric field,  $E_x$ , and the vertical component,  $E_y$ ) emanating from a Ag nanoslit (slit width of 100 nm and metal thickness of 200 nm). A TM-polarized planar wave (650 nm wavelength) is incident from the bottom side, exciting surface plasmons at the slit edges. The free-space wavefronts of  $H_z$  and  $E_y$  fields appear circular (cylindrical in 3D) for all angles. While the  $H_z$  field strength remains constant for all angles (except for on metal surface) on each wavefront, the  $E_y$  field tapers off towards the forward normal direction. In the case of the  $E_x$  field, the field strength is highest in the normal propagation direction and becomes weaker for larger (glancing) angles. It is interesting to note that the wavefronts of the  $E_x$  field show a distortion near metal surface, i.e., the circular wavefronts become thinner initially when approaching the metal and then become thicker and bent inward when touching the surface. This wavefront distortion indicates strong presence of the tangential component of  $E$ -field on metal surface, contributed by surface plasmons. SPs propagating on a metal/dielectric interface are known to have both vertical (transverse) and horizontal (longitudinal) components of  $E$ -field, with an amplitude ratio of  $E_x/E_y = -i\gamma_D/k_{sp} = -i(-\epsilon_M/\epsilon_D)^{-1/2}$ . Here  $\gamma_D$  is the decay constant of the field along the transverse direction in air and  $k_{sp}$  is the surface plasmon propagation constant.  $\epsilon_M$  and  $\epsilon_D$  are the dielectric constant of metal and air, respectively. In the case of Ag/air interface at 650 nm wavelength (dielectric constant of Ag,

$\epsilon_M = -16 + i1.1$ ) [115], this ratio is calculated to be 1/4. In lossless plasmonic metals (i.e., when dielectric functions are purely negative real), the two components of the  $E$ -field are  $90^\circ$  out of phase each other, while the transverse component ( $E_y$ ) is  $180^\circ$  out of phase with the magnetic field ( $H_z$ ). When the  $E_x$  wavefronts' touch-down points on metal surface are compared with the  $H_z$  wavefronts, it can be shown that the  $E_x$  field is  $90^\circ$  out of phase with the  $H_z$  and  $E_y$  fields. This confirms the plasmonic nature of the tangential electric field observed in the distorted region. The in- or out of phase relationship between the electric and magnetic field components indicates that there is a net steady-state energy flow along the metal surface (longitudinal direction), but not across the interface (transverse direction). The transverse component of the Poynting vector is imaginary on the metal surface and this induces a vortex-like circulation of energy flow across the interface [116,117]. The SPs and free-space radiation components have different propagation constants, and one may speculate that this also contributed to the wavefront distortion of the  $E_x$  field [100,106]. The corresponding difference in wavelength, however, is only 3 % for Ag/air at 650 nm free-space wavelength, and would not make a noticeable change on the wavefront profiles. This interpretation is consistent with the analysis results of other field components ( $E_y$  and  $H_z$ ) which comprise contributions from both free-space radiation and surface plasmons, but do not show any noticeable distortion in their wavefronts.

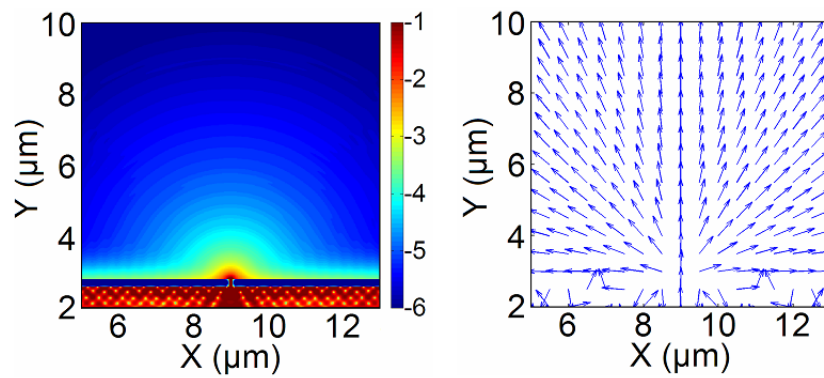
The time-averaged Poynting vector was calculated from the electromagnetic fields (Figure 6.12 (b) for the amplitude and orientation, and Figure 6.12 (c) for the vertical and horizontal components). The energy flow associated with the waves emanating from the nanoslit appears uniform in most radial directions. In the glancing angle region, however, the horizontal component of Poynting vector becomes stronger towards the metal surface. This indicates that a significant amount of energy flows away from the slit along the metal surface in the form of SPs.

Figure 6.13 shows the radiation pattern plotted as a function of angle for different radial distances ( $r = 0.65, 1.30, 2.60, \text{ and } 5.20 \text{ } \mu\text{m}$ ). Measurement results are also shown for comparison. For the radiation angles approaching  $90^\circ$ , the SP power becomes significantly larger than the horizontal component of the optical power carried by a free-space cylindrical wave. At  $r = 5.2 \text{ } \mu\text{m}$ , for example, the calculated intensity at  $\theta = 85^\circ$  is  $\sim 2$  times that at  $\theta = 0^\circ$ , and the ratio increases to  $\sim 6$  at  $\theta = 90^\circ$ . The intensity measured at ( $r = 5.2 \text{ } \mu\text{m}, \theta = 85^\circ$ ) is  $\sim 2$  times the intensity at  $0$  degree, showing a good agreement with the calculation. The SP propagation length in an Ag/air interface is estimated to be  $\sim 20 \text{ } \mu\text{m}$  at  $633 \text{ nm}$ , significantly larger than the scan range tested in this work. Assuming the SP propagation loss is negligible over the  $5 \text{ } \mu\text{m}$  span, the initial total power carried by SPs emanating from the nanoslit is expressed as  $P_{sp} = \gamma_D^{-1} I_{sp}(r, \theta = 90^\circ)$ . Similarly the total power carried by a free-space cylindrical wave is expressed as  $P_r = \pi r I_r(r)$ . Here,  $I_{sp}$  and  $I_r$  are the intensities of the surface plasmons and free-space radiation, respectively. The ratio of the two powers,  $P_{sp}/P_r$  is estimated to be  $\sim 1/9$  from the simulation result at  $r = 5 \text{ } \mu\text{m}$ . This corresponds to the branching ratio of the plasmon power transmitted through a nanoslit when it splits into a free-space radiation and surface plasmons. This ratio is expected to be sensitively dependent of the geometry of slit edges, and the sharpness (or the radius of curvature). In a more detailed comparison, the measured profiles tend to show somewhat earlier rises compared to the simulation result. The intensity profile measured at  $r = 1.3 \text{ } \mu\text{m}$ , for example, begins to rise at around  $60^\circ$ . This corresponds to a probe-to-metal distance of  $0.65 \text{ } \mu\text{m}$ , significantly larger than the penetration depth of plasmon power to the air side ( $(2\gamma_D)^{-1} \sim 0.2 \text{ } \mu\text{m}$ ). This discrepancy is ascribed to the fact that the nanoapertured probe has a relatively large acceptance angle ( $\pm 20^\circ$ ) whereas the simulation assumed the probe transmits only the pure radial component of radiation (i.e., a

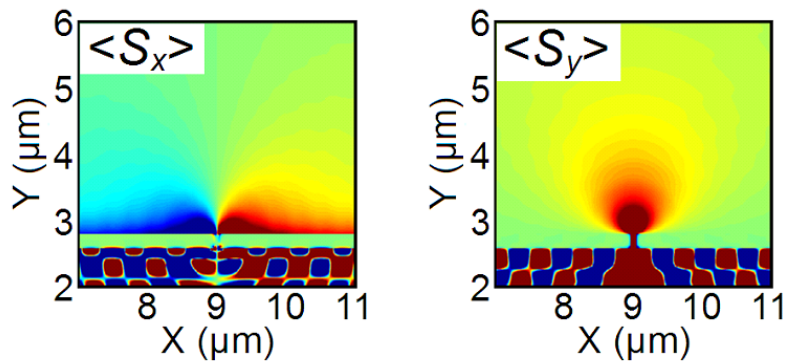
normally incident light) in calculating the radiation pattern. In the near- to intermediate region ( $r < 2 \mu\text{m}$ ), the measured intensity turned out to be significantly lower than the simulation result. This is ascribed to the finite size of apertures (slit width and aperture diameter) used in this work. The wavelet components emanating from the two edges of a nanoslit, for example, arrive at the observation points (probe aperture edges) with a certain amount of phase difference. In conjunction with the sensitive angular dependence of the nanoapertured probe transmission, this phase difference has the effect of destructive interference causing a reduction of the overall probe transmission.



(a)



(b)



(c)

**Figure 6.12** FDTD simulation of nanoslit radiation. (a) Snap-shot images of field distributions ( $H_z$ ,  $E_x$ , and  $E_y$ ). (b) Intensity distribution (left: log scale for intensity) and the direction of energy flow (right: orientation of the time-averaged Poynting vector). (c) The horizontal (left) and vertical (right) components of the time-averaged Poynting vector.

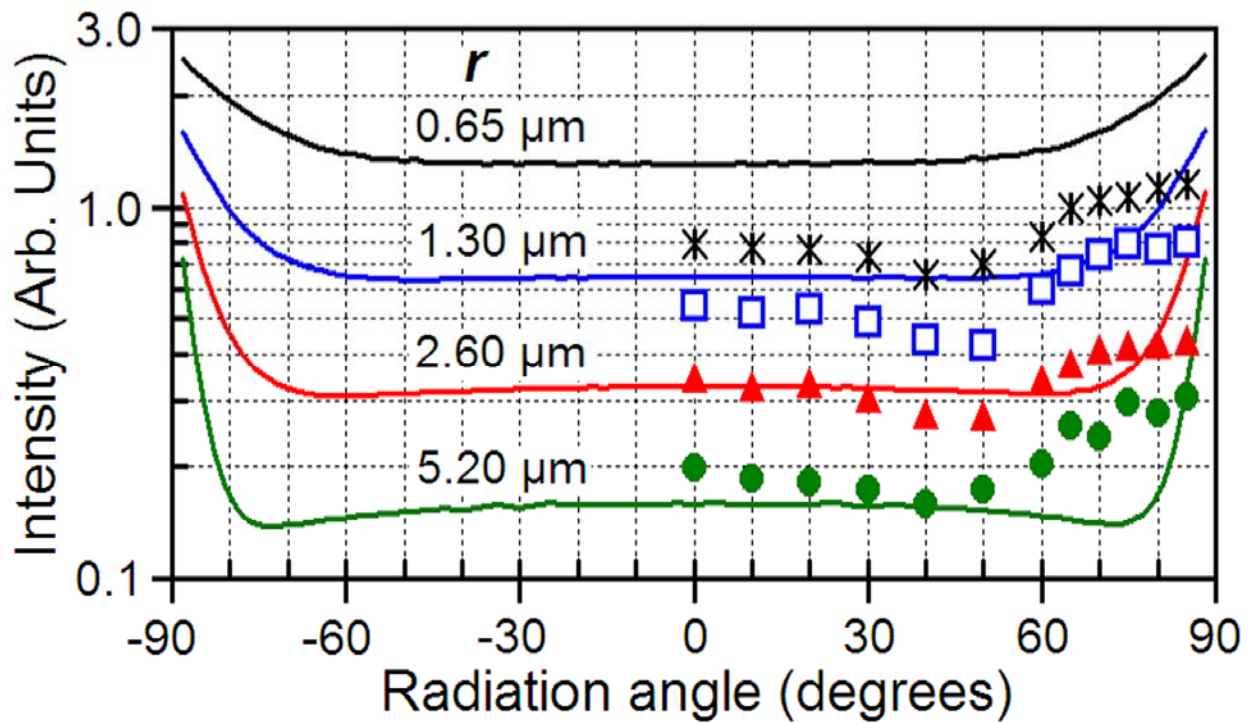


**Figure 6.13** The radiation intensity plotted as a function of angle for different radial distances: radial distance of 0.65, 1.30, 2.60, 5.20  $\mu\text{m}$  (top to bottom). Measurement results are shown for comparison (black star for 0.67, blue square for 1.34, red triangle for 2.54; green circle for 5.21  $\mu\text{m}$ ).

## 6.4 SUMMARY

We reported the radiation pattern (radial and angular distribution of light intensity) of a silver nanoslit measured in the near- to far-fields by linearly scanning a nanoapertured probe along the radial direction with the probe axis tilted parallel to the scan direction. In most of the far-field regime the  $1/r$  dependence is clearly observed. In the glancing angle regime, the radiation pattern is found to be significantly affected by the presence of surface plasmons, showing higher intensity closer to the metal surface. In the near- to intermediate regime where the finite aperture sizes of the slit and the probe have an effect of destructive interference, the intensity profiles fall off faster than the  $1/r$  dependence. The scanning probe technique introduced in this work allows for measurements of radiation patterns (angular and radial dependence) of a metal nanoslit in the near- to far-fields. A detailed understanding gained in this study on how the different propagation components behave and interplay in the near- to far-fields is expected to serve as an important base when studying advanced plasmonic structures.

## **7.0 NEAR- TO FAR-FIELD IMAGING OF PHASE EVOLUTION OF LIGHT EMANATING FROM A METAL NANOSLIT**

### **7.1 INTRODUCTION**

Interaction of light with a nanoapertured metal film has been the subject of extensive study because it produces many interesting phenomena, such as “enhanced” transmission of light through a nanohole array or shaping the spatial or spectral profiles of the transmitted light [118-128]. The richness of the phenomena stems from the complexity of the way that light interacts with the nanostructures formed in the metal film. Surface plasmons (SPs), collective oscillation of electrons carrying the electromagnetic energy in the form of photons trapped at a meta/dielectric interface, can effectively mediate the interactions between metal nanostructures [129]. Unlike the dielectric case, a metal nanostructure can also efficiently interact with free-space radiation, diffracting an incident light and/or coupling the light into surface plasmons (vice versa, decoupling surface plasmons into free-space radiation). This implies the multiplicity of the interaction pathways available on nanostructured metal surface. When properly designed, the effects of near-field interactions between nanostructures can also reach the far-field region through diffraction and constructive interference among them. The spatial and/or spectral profiles of far-field optical transmission through a metal nanoslit array, for example, are known to be governed by various resonances occurring on different sections of metal surface [130]. The

roles played by surface plasmons and free-space radiation in the interaction of metal nanostructures, however, have not been clearly understood and have been a subject of debate. The surface-bound wave and free-space radiation behave differently in terms of propagation constant (wavelength and attenuation), field distribution, etc., and analyzing individual roles and their interplay in an arbitrary structure is considered a challenge.

A single nanoaperture formed in a metal film is a simple and yet the most fundamental structure that can be viewed as a basic building block of aperture-based nano-plasmonic structures. Evolution of optical wavefronts emanating from a metal nanoaperture is of essential interest in studying the plasmonic structures, and yet a detailed understanding is not fully established on how the different wave components (free-space diffraction and surface bound waves) interplay and evolve over the near- to far-field regime [120-127]. In this work, we report near- to far-field imaging of optical wavefronts emanating from a single nanoslit formed on a thin Ag film.

## **7.2 FABRICATION AND CHARACTERIZATION**

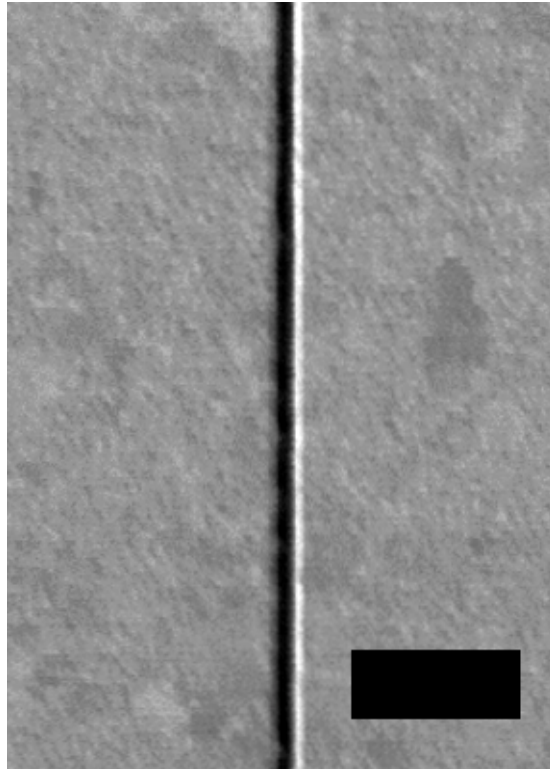
### **7.2.1 Fabrication of single nanoslit using a focused-ion-beam etching technique**

Figure 7.1 shows a scanning electron microscope (SEM) image of a 80-nm-wide single nanoslit formed in a 50-nm-thick Ag layer. Ag nanoslits were formed on a fused silica substrate (Corning 7980: 500  $\mu\text{m}$  thick; double-side polished). First, a 50-nm-thick Ag layer was deposited on the substrate by thermal evaporation of Ag (Alfar, 4N8 purity). Single nanoslit (80 nm width and 500  $\mu\text{m}$  length) was then formed in the Ag layer using a focused-ion-beam etching

technique and the etching depth of a nanoslit was 100 nm. Seiko SMI-3050-SE dual beam system was used with Ga ion beam (beam current of 10 pA). The schematic process flow of this technique has been described in Figure 6.2.

### **7.2.2 Measurement setup**

Figure 7.2 shows the intensity profile measurements setup using a nanoaperture probe. A nanoapertured fiber probe (Veeco Aurora NSOM probe 1720-00: 100-nm-thick Al coated; 80-nm diameter aperture; formed on a tapered, single-mode silica fiber with core diameter of 4  $\mu\text{m}$  and NA of 0.11; 1400  $\mu\text{m}$  total length of the tapered section coated with Al; full tapered angle of  $4^\circ$ ) was used in this work. A TM-polarized laser light (He-Ne laser; 633 nm wavelength; 10 mW; 1 mm beam diameter; 1 mrad beam divergence) was incident to the substrate side, and the transmitted light was imaged by scanning a nanoprobe (Veeco Aurora NSOM probe 1720-00: 100-nm-thick Al coated; 80-nm aperture diameter) in the horizontal direction at the exit side. The probe output was measured with a photomultiplier tube (Hamamatsu H7468-20). The scanning probe experiments were carried out with a home-built scanning stage setup (PI E-621.1CD for nanopositioning and E-665.CR for servo control) interfaced with LabView 7.0 (National Instruments). Figure 7.3 shows a schematic drawing of the measurement scanned across a single nanoslit with the nanoprobe fiber aligned perpendicular to the metal surface. The scan range used in this work was 20  $\mu\text{m}$  x 8  $\mu\text{m}$ , with a step size of 50 nm in the horizontal direction and 133 nm in the vertical direction.



**Figure 7.1** SEM image (Top view) of a 80-nm-wide slit formed in a 50-nm-thick Ag layer deposited on a fused silica substrate. A focused-ion-beam etching technique was employed to form the nanoslit structure (scale bar, 500 nm).

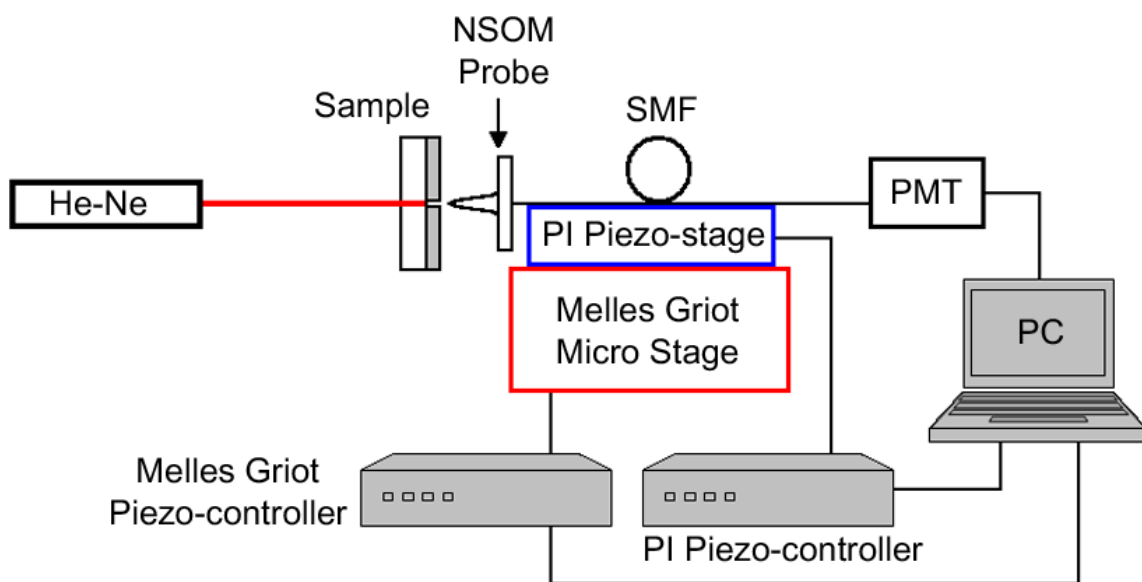


**Figure 7.2** Schematic of an optical transmission measurement setup using a scanning probe technique.

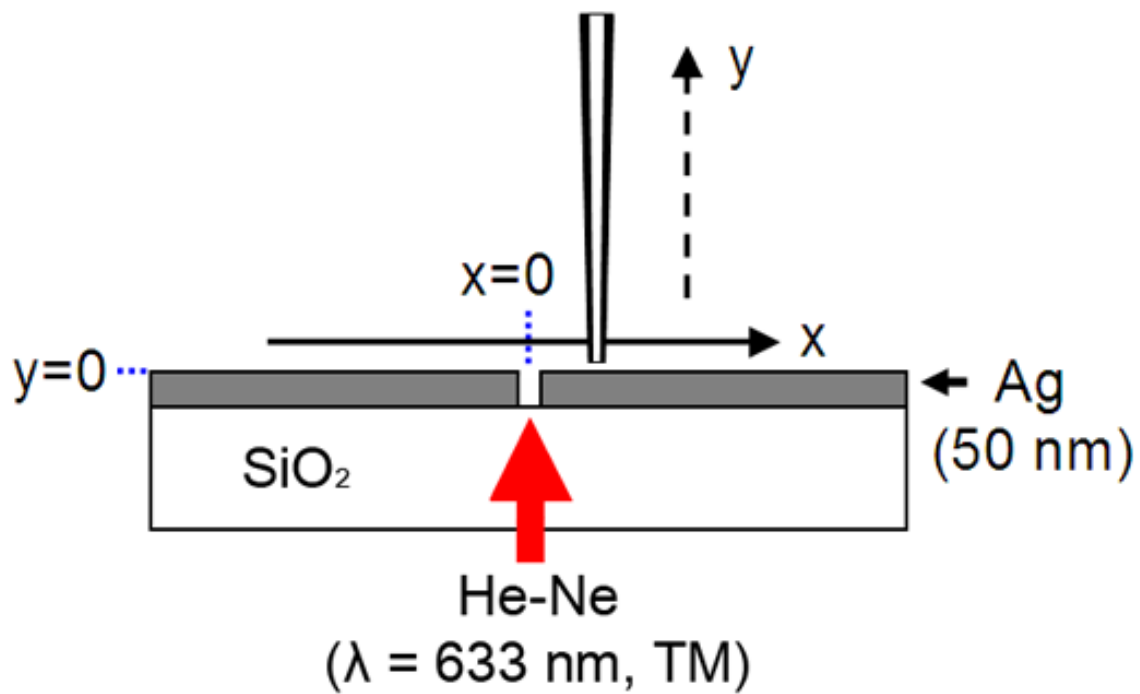


**Figure 7.3** Schematic drawing of the measurement setup. TM polarized laser light is incident to the nanoslit (80-nm wide and 50-nm thick) from the substrate side, and a nanoapertured scanning probe is scanned along the horizontal direction with a step size of 50 nm.

### 7.2.3 Characterization

Figure 7.4 shows some of the scan profiles obtained in the near- to far-field regime using a metal nanoapertured probe. Fringes form and evolve over the entire regime, since the light partially (and directly) transmitted through the thin Ag film interferes with the waves transmitted through the nanoslit [131-133]. The fringe spacing increases for larger probe-to-surface distance and/or towards the central region on a given scan. Figure 7.5 (a) shows a two-dimensional (2D) map of the scan profiles over the entire regime (near- to far-fields): 71 scan profiles are displayed with the fringe amplitude color-coded.

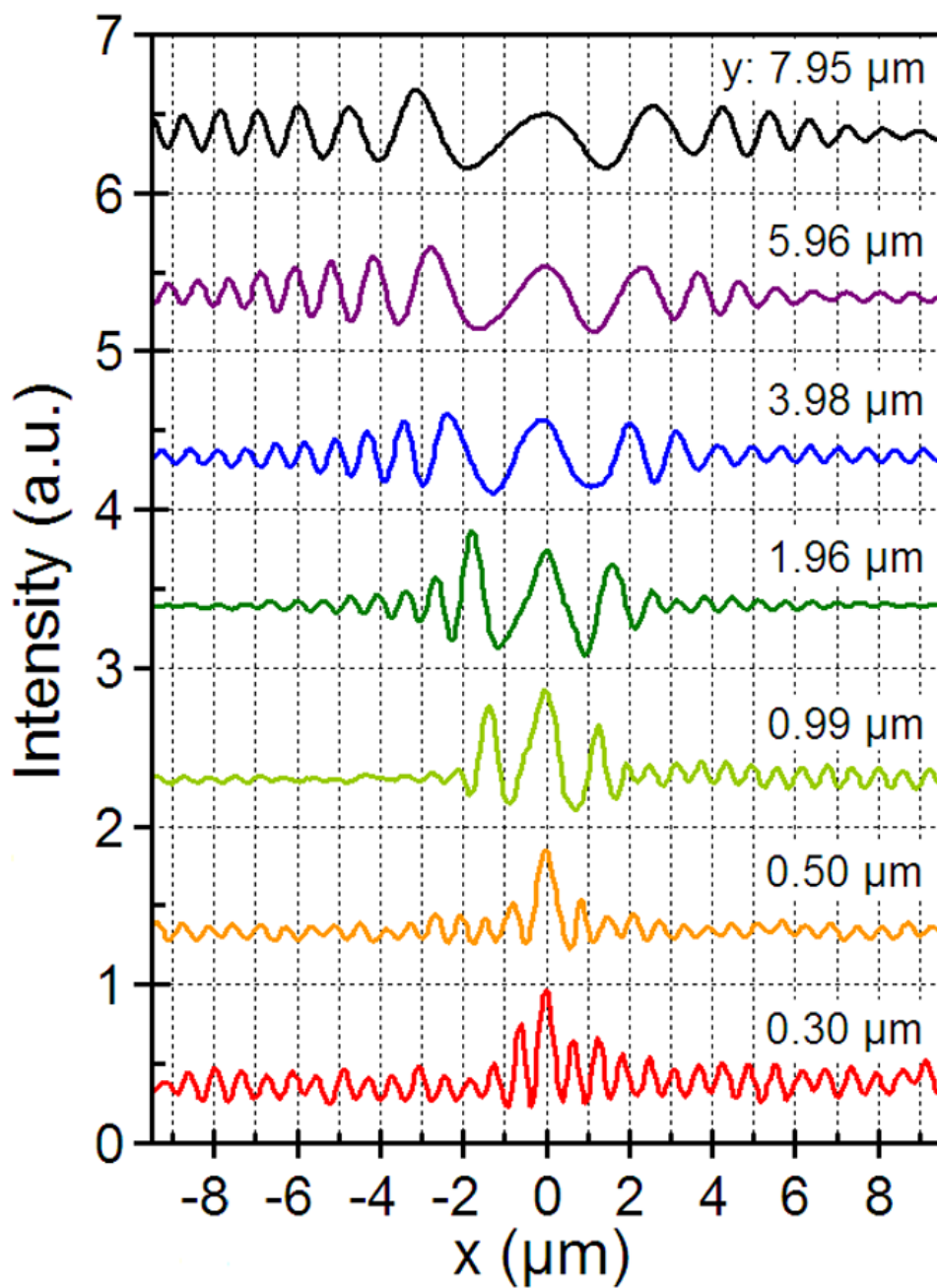


**Figure 7.4** Scan profiles of the interference pattern of slit-transmitted and direct film-transmitted waves. The base line of each scan is shown as a dotted line.

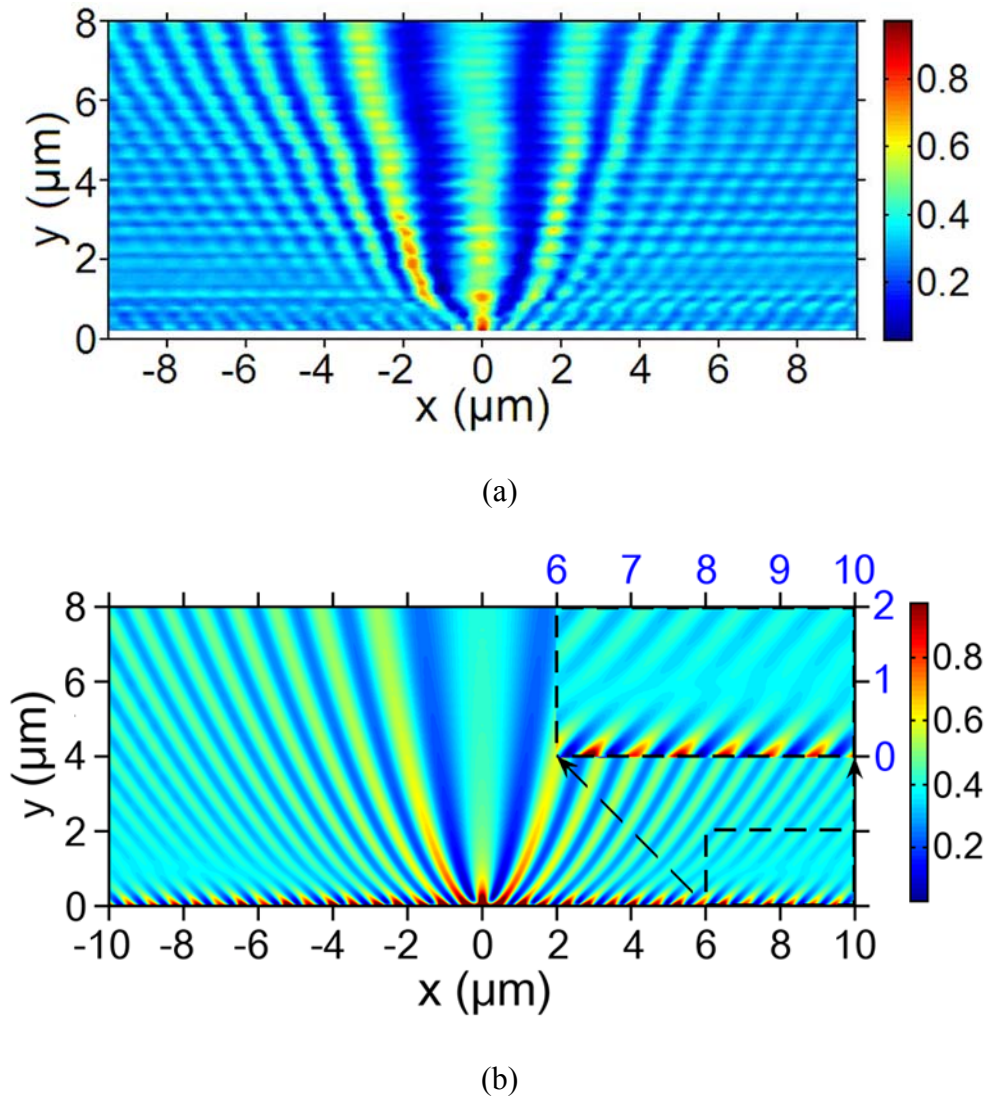


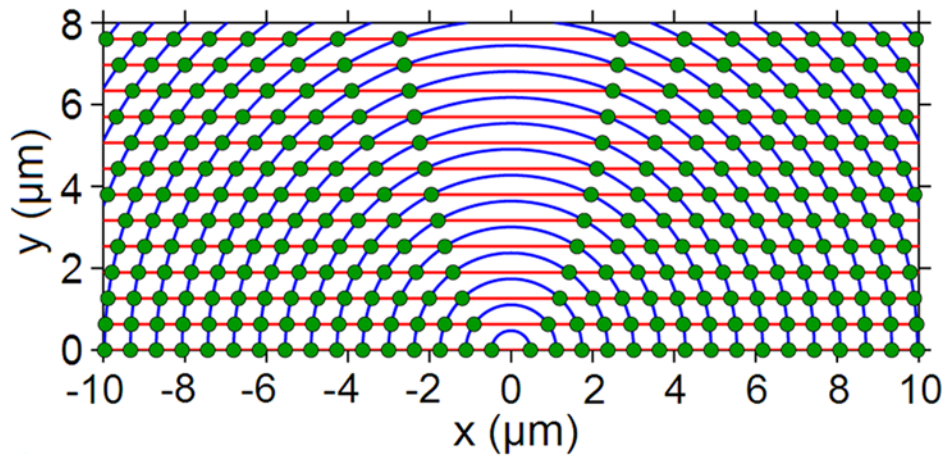
**Figure 7.5** Near- to far-field imaging of optical wavefronts emanating from a nanoslit formed in a thin Ag film. (a) 2D map of the interference pattern with the intensity color-coded (measurements). Red corresponds to the peak of a fringe and blue represents the valley. The periodic modulation of intensity along the vertical ( $y$ ) direction is ascribed to the Fabry-Perot resonance effect of a local cavity structure formed by the probe tip and the sample surface. (b) The interference fringe pattern calculated from a FDTD simulation of optical transmission through a Ag nanoslit (80-nm wide and 50-nm thick): The vertical component of the Poynting vector. The inset in the top right part is a magnified view of the bottom right corner region ( $x$ : 6-10  $\mu\text{m}$ ;  $y$ : 0-2  $\mu\text{m}$ ). The dielectric constants of silica and Ag used in this simulation are from References 18 and 19.

### 7.3 RESULTS AND DISCUSSION

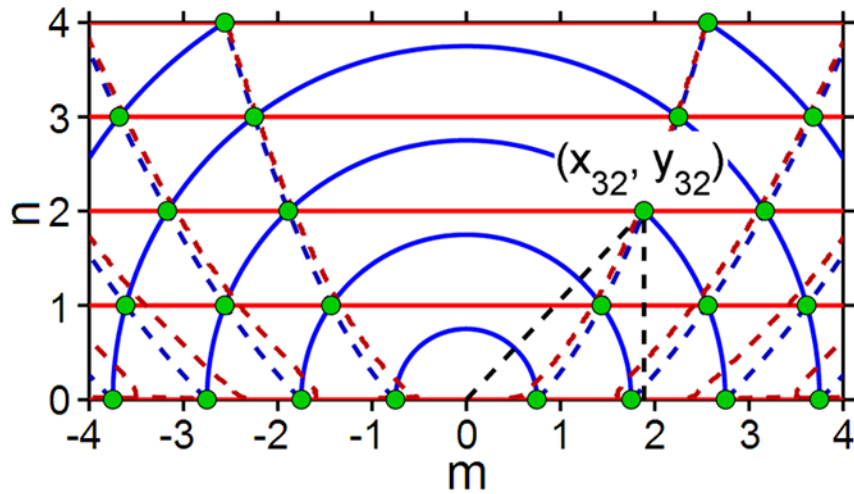
In order to elucidate the interference nature of fringe formation, a schematic of two propagating waves is shown in Figure 7.6 (a), one emanating from a nanoslit with cylindrical wavefronts and the other directly transmitted through a thin metal film for a planar wave incident from the bottom side. The fringes resulting from constructive interference of the two waves are marked on the cross points of the wavefronts. In this diagram, the  $(m,n)$ -th cross point corresponds to the interference of the  $m$ -th cylindrical wavefront ( $m = 1, 2, 3, \dots$ ) radiating from the nanoslit and the  $n$ -th planar wavefront ( $n = 0, 1, 2, 3, \dots$ ) directly transmitted through a metal film. After a simple analysis, the coordinates of the  $(m,n)$ -th cross points,  $(x_{m,n}, y_{m,n})$  can be determined as follows.

$$x_{m,n} = \left[ \left( m + \frac{\phi}{2\pi} \right)^2 - n^2 \right]^{1/2} \lambda \quad ; \quad y_{m,n} = n\lambda \quad (7.1)$$

Here  $\lambda$  is the free-space wavelength of the transmitted light.  $\phi$  is the phase difference between the directly-transmitted planar wave ( $\phi_1$ ) and the nanoslit-transmitted cylindrical wave ( $\phi_2$ ), that is,  $\phi = \phi_1 - \phi_2$ , and  $|\phi| < \pi$ . In the region far from the slit and yet with relatively small probe-surface distance ( $m \gg n$ ), the fringe location can be expressed as  $x_{m,n} \cong (m + \phi/2\pi)\lambda$  ;  $y_{m,n} = n\lambda$ . This tells the fringe spacing asymptotically approaches the free-space wavelength, and the fringe locations are off-shifted from the integer multiple of wavelength positions by the amount proportional to phase retardation  $\phi$ .



(a)



(b)

**Figure 7.6** Interference of slit-transmitted and direct, film-transmitted waves. (a) Wavefronts of slit-transmission (cylindrical curves) and direct film-transmission (horizontal lines). (b) A close-up view of the low-order fringe tracks in the two-wave interference model. The blue dashed curves represent the fringe tracks calculated from the two-wave model, and the red dashed curves are a FDTD simulation result. The dielectric constants of silica and Ag used in this simulation are from References 18 and 19.

Interference of two waves of different symmetry (cylindrical versus planar) results in a characteristic fringe pattern (Figure 7.5 and Figure 7.6). The first track on either side from the center corresponds to the cross-points of the  $n$ -th planar wavefront and the  $(n+1)$ -th radial wavefront, i.e., the case of  $m = n + 1$  in equation (7.1). In general, the  $l$ -th track comprises the cross-points,  $(x_{m,n}, y_{m,n})$  with  $m = n + l$ . On a given track and in the region far from the metal surface ( $n \gg l$ ), the fringe location traces approximately a parabolic profile, i.e.,  $x_l(n) \cong \lambda\sqrt{2nl}$ . Figure 7.5 (b) shows a Poynting vector (the  $y$ -component) distribution calculated from the finite-difference-time-domain (FDTD) analysis of wave transmission through a nanoslit [134]. The vertical ( $y$ -) component of the Poynting vector is the main contributor to the scanning probe output, since the probe is aligned normal to the sample surface [120]. Overall the fringe pattern obtained from a FDTD simulation shows a good agreement with the measurement result (Figure 7.5 (a) and (b)). Figure 7.6 (b) shows a detailed comparison between the cylindrical-and-planar-wave-interference model (blue dashed curves) and the FDTD simulation (red dashed curves) results. While both agree well in the far-field regime, a clear difference is observed in the near-to intermediate-field regime: the FDTD simulation predicts a fringe track shifted inward from that of the two-wave-model. This discrepancy is ascribed to stronger presence of surface plasmon waves near the metal surface compared with the slit-transmitted cylindrical wave (Figure 7.5 (b)). The fringe spacing near the metal surface is significantly smaller than the free space wavelength as can be seen in the mismatch of the fringe patterns in the near and far-fields. The fuzzy area corresponds to the transition region between the two distinct regimes where either slit radiation or surface plasmon field is dominant over the other. In this region, phase singularity exists at the points where the two fringes completely mismatch [123, 132] (see the

inset of Figure 7.5 (b)). The phase singularity indicates that the optical fields of slit-diffraction and surface plasmons cancel each other and the phase becomes undefined in the local area.

For detailed analysis, the three wave components that are expected to have significant presence in the near- to far-fields are expressed as follows. 1) a partial, directly-transmitted wave (TM polarized) through a thin metal layer:  $\vec{H}_1 = \hat{z}H_1e^{iky}$  and  $\vec{E}_1 = -\hat{x}\eta H_1e^{iky}$ , where  $\eta = \sqrt{\mu/\epsilon}$ .

2) a free-space radiation wave emanating from the slit:  $\vec{H}_2 = \hat{z}H_2e^{ik\cdot\vec{r}}$  and  $\vec{E}_2 = (-1/i\omega\epsilon)\nabla\times\vec{H}_2$ . In

the regime where a slowly varying condition (i.e.,  $|H_2| \gg \left|\frac{\partial H_2}{\partial x}\right|, \left|\frac{\partial H_2}{\partial y}\right|$ ) is satisfied, the electric field

vector can be approximated as follows.  $\vec{E}_2 = (-\hat{x}\sin\theta + \hat{y}\cos\theta)\eta H_2e^{ik(x\cos\theta+y\sin\theta)}$ . 3) surface

plasmons generated at the slit edges and propagating away from the slit:  $\vec{H}_3 = \hat{z}H_3e^{-\gamma_{sp}y}e^{\pm ik_{sp}x}$  and

$\vec{E}_3 = (-1/i\omega\epsilon)\nabla\times\vec{H}_3 = \hat{x}(\gamma_{sp}/i\omega\epsilon)H_3e^{-\gamma_{sp}y}e^{\pm ik_{sp}x} + \hat{y}(\pm k_{sp}/\omega\epsilon)H_3e^{-\gamma_{sp}y}e^{\pm ik_{sp}x}$ .

Here the  $\pm$  sign corresponds to the surface plasmons propagating along the positive (+) or negative  $x$ -direction (-), respectively. Regarding the phase relationship of slit-transmitted waves,

it should be noted that the free-space radiation and SP waves ( $H_2$  and  $H_3$ ) are in phase at the slit exit, since they originate from the same surface plasmon wave transmitted through a nanoslit.

The region proximal to the slit and the intermediate-to-far-field regime (where the SP fields are negligible) can be well described in terms of interplay of the two wave components, direct

transmission through a film ( $\vec{E}_1, \vec{H}_1$ ) and nanoslit radiation ( $\vec{E}_2, \vec{H}_2$ ). The time-averaged energy

flow can then be expressed with the Poynting vector as follows.  $\langle\vec{S}\rangle = (\vec{E}_1 + \vec{E}_2)\times(\vec{H}_1 + \vec{H}_2)^*$ . As the

probe scans away from the slit ( $\theta \rightarrow 0$ ) at a constant probe-surface distance ( $y = y_0$ ), the  $y$ -component of the Poynting vector (the main contributor to the probe output) asymptotically

approaches the following expression:

$$\langle S_y \rangle = \eta |H_1|^2 + \eta |H_1| |H_2| \cos(kx - ky_0 - \phi) + i \eta |H_1| |H_2| \sin(kx - ky_0 - \phi) \quad (7.2)$$

Here  $\phi$  is the phase difference between the directly-transmitted and slit-transmitted waves as defined above with equation (7.1). The real part of the Poynting vector component,  $\text{Re}(\langle S_y \rangle)$  corresponds to the scan profile measured with a nanoapertured probe, and the fringe peaks occur at  $x = \lambda(m + \frac{y_0}{\lambda} + \frac{\phi}{2\pi})$ . Note that at  $y_0 = n\lambda$  this formula reduces to the one derived from the two-wave-interference diagram shown in Figure 7.6 (b). The phase relationship ( $\phi$ ) of the slit transmitted wave and the direct transmission determines the exact location of fringes (the offset from the positions at integral multiple of free-space wavelength).

In the vicinity of the slit, the radial wave ( $H_2$ ) shows faster damping ( $1/r^{1/2}$ ) compared with the SP's exponential decay along the  $x$ -direction. In the region distant from the slit but near the metal surface, the wave interaction can be described in terms of SP and direct transmission, and the probe output at  $y = 0$  can be expressed as follows.

$$\begin{aligned} \text{Re}(\langle S_y \rangle) &= \eta |H_1|^2 + \eta |H_1| |H_3| \cos(k_{sp}x \mp \phi) \mp \frac{\gamma_{sp}}{\omega \epsilon} |H_1| |H_3| \sin(k_{sp}x \mp \phi) \\ &= \eta |H_1|^2 + \eta |H_1| |H_3| A \cos(k_{sp}x \mp \phi \pm \alpha) \end{aligned} \quad (7.3)$$

Here  $\alpha = \tan^{-1}(\gamma_{sp} / k)$ . The fringe peaks occur at  $k_{sp}x = 2\pi m \pm \phi \mp \alpha$  with the spacing equal to the plasmon wavelength  $\lambda_{sp}$ . Compared with the far-field case, the fringe location is affected by an extra term  $\alpha$ , which is separate from the shift caused by the phase retardation  $\phi$ . This extra phase

shift originates from the horizontal component of the SP electric field ( $E_{3x}$ ), which is out-of-phase (by  $\pi/2$ ) with its normal component ( $E_{3y}$ ) [129, 137].

Figure 7.7 shows a detailed comparison of the scan profiles measured in the near- to intermediate- to far-field regimes ( $y = 200$  nm, 630 nm, and 7.6  $\mu\text{m}$ , respectively) with the corresponding FDTD simulation results. Overall a good agreement is observed in all three regimes. According to the FDTD simulation (Figure 5.5 (b)), the region outside  $\sim 1$   $\mu\text{m}$  distance from the metal surface is free from the effect of surface plasmon presence. The fringe locations in this regime are governed by the interference of direct transmission and slit radiation, and can be described by equation (7.1). From the measured peak locations and referring to equation (7.1) with  $\lambda = 633$  nm,  $n = 12$ , and  $m = 13$  to 19, the phase retardation  $\phi$  is estimated to be  $-86 \pm 10$  degrees. This negative retardation depicts a relationship that the phase of the nanoslit-transmitted wave leads the directly transmitted wave by  $\sim 86$  degrees (or equivalently, in terms of wavefronts, trails by  $\sim 86$  degrees). In the case of near-field scan, the measured fringe spacing is  $605 \pm 10$  nm, showing a reasonable agreement with the surface plasmon wavelength  $\lambda_{sp}$  (613 nm) as expected from equation (7.3).

Next we elucidate the nature of phase evolution of each wave component during transmission through a nanoslit or a thin metal film. For a given planar wave incident from the substrate side, the three waves take different paths, accumulating different amount of phase when measured at the exit surface of nanoslit. For the case of direct transmission through a metal film (of thickness  $d$ ), the total phase retardation can be calculated from the transmission coefficient of the metal layer:  $t = \frac{t_{12}t_{23}e^{ik_2d}}{1 - r_{21}r_{23}e^{i2k_2d}}$ . Here  $t_{ij}$  is the transmission at the interface of the  $i$ -th and the  $j$ -th layers, and can be expressed as  $t_{ij} = 2\sqrt{\varepsilon_i} / (\sqrt{\varepsilon_i} + \sqrt{\varepsilon_j})$ .  $i = 1, 2$ , and 3 represents substrate (quartz),

metal (Ag) and air side, respectively, and  $\varepsilon_i$  is the corresponding dielectric constant. Similarly,  $r_{ij}$  is the reflection coefficient at the  $i$ - $j$  layer interface with the  $i$ -th layer as the incidence side, and is expressed as  $r_{ij} = (\sqrt{\varepsilon_j} - \sqrt{\varepsilon_i}) / (\sqrt{\varepsilon_i} + \sqrt{\varepsilon_j})$ . The total amount of phase change of direct transmission is calculated to be -50 degrees. [For the metal thickness (50 nm) studied in this work, the single pass transmission in the metal layer is 0.14, therefore the multiple internal reflection effect is insignificant. The main contributions are from the two interfacial transmissions, i.e., from the phases of  $t_{12}$  and  $t_{23}$ ]. The phase change of a slit-transmitted wave comes from the phase accumulation during SP propagation through a slit,  $\text{Re}(k_{sp})d$ . For the case of a 80-nm-wide and 50-nm-deep slit, the phase retardation is estimated to be +35 degrees. Combining the two phase change components, overall the nanoslit transmitted wave leads the directly transmitted wave by 85 degrees of phase, that is  $\phi = -85$  degrees. Figure 7.8 shows a FDTD simulation of phase relationship of the two wave components. The wave transmitted through a nanoslit leads the direct transmission by 90 degrees of phase as can be seen from the comparison of wavefront locations at the exit side for the same incident wave. The analytical and simulation results clearly confirm the phase retardation ( $\phi = -86 \pm 10$  degrees) extracted from the measurement data discussed above.

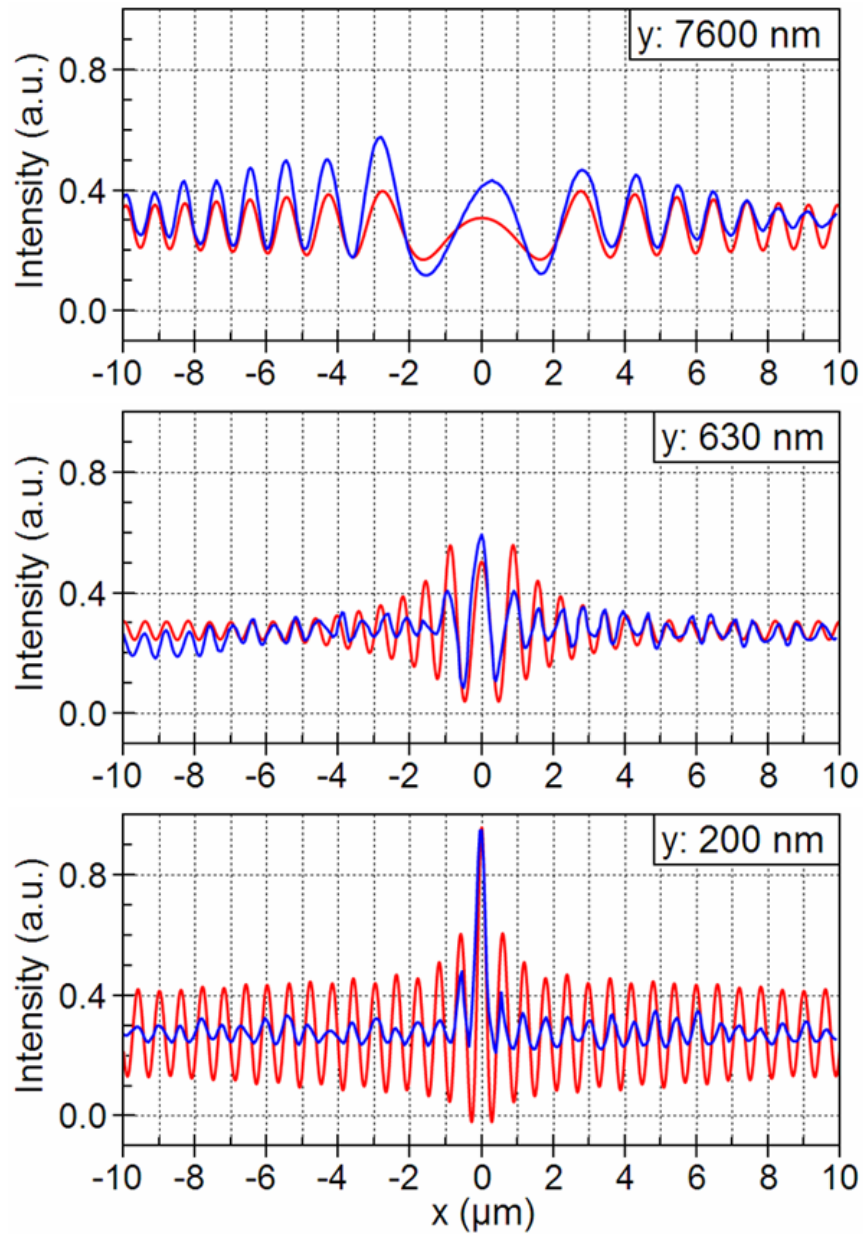


**Figure 7.7** Comparison between the measured scan profiles and FDTD simulation result. The scan profiles were measured with the same slit as in Figure 7.1 at probe-surface distance of 7.6 μm, 630 nm, or 200 nm (top to bottom) with a scan step size of 10 nm. Blue curves correspond to the measurement, and red to the FDTD.

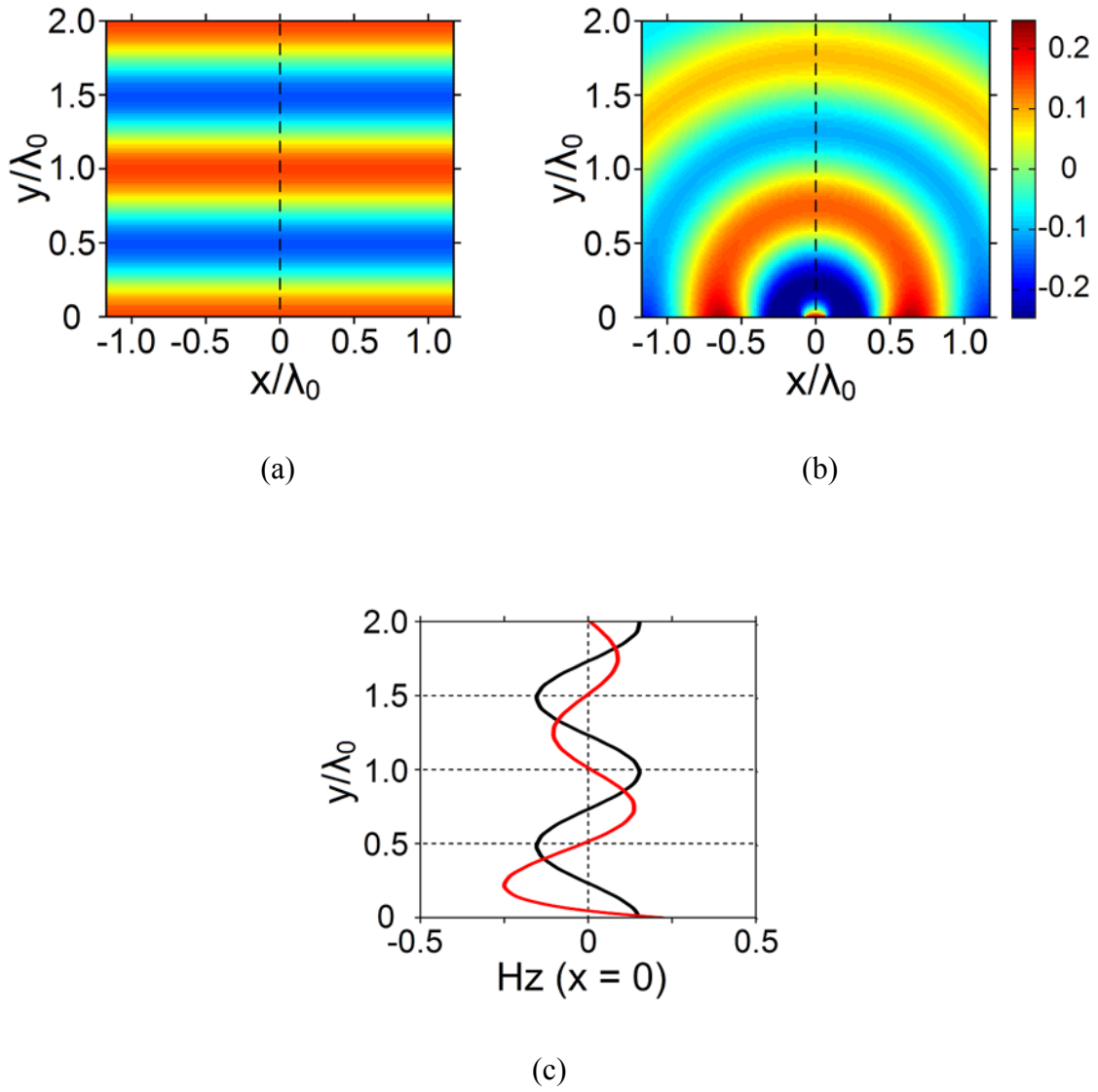


**Figure 7.8** FDTD simulation of phase relationship of slit-transmission and direct film-transmission. The wavefronts of direct film-transmission (a) and slit transmission (b). (c) Comparison of optical phases of direct transmitted wave (black) and slit transmitted wave (red). The direct transmission was calculated for a 50-nm-thick Ag layer without a slit. The slit radiation was calculated from a nanoslit simulation result by subtracting the direct transmission component.

## 7.4 SUMMARY

A single nanoaperture formed in a metal film is a simple and yet the most fundamental structure that can be viewed as a basic building block of aperture-based nano-plasmonic structures. Evolution of optical wavefronts emanating from a metal nanoaperture is of essential interest in studying the plasmonic structures, and yet a detailed understanding is not fully established on how the different wave components (free-space diffraction and surface bound waves) interplay and evolve over the near- to far-field regime. In this chapter, we reported near- to far-field measurement of optical wavefronts emanating from a nanoslit formed in a thin (50 nm thick) Ag film. The evolution of optical phases is imaged using a self-interference technique in conjunction with a scanning probe method. The phase relationship of the slit-transmitted waves with respect to the direct transmission through the thin metal film is quantitatively established. The singular-phase points resulting from the interplay of slit diffraction and surface plasmons are identified in the intermediate-field region. Imaging of optical wavefronts in the near- to far-fields is expected to be important in designing advanced nano-optic and plasmonic structures where precise control of optical phase is essential.

## **8.0 NEGATIVE REFRACTION OF LIGHT WITHOUT NEGATIVE-INDEX MEDIA**

### **8.1 INTRODUCTION**

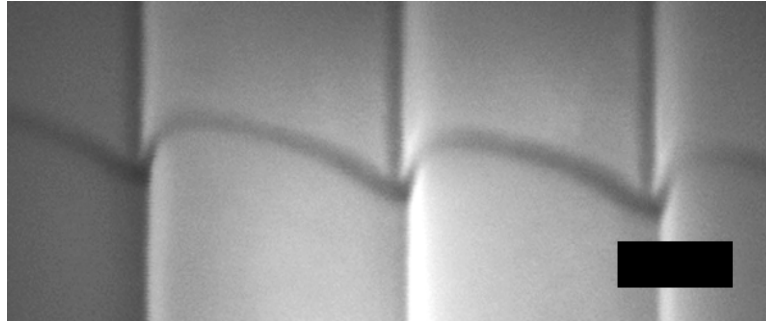
Refraction of light at an interface of two different media forms an essential basis in imaging and beam-shaping optics. In the case of an interface with an artificial medium whose refractive index is negative, light can be bent to a negative angle with the surface normal [138-141]. Refraction is commonly viewed as a macroscale phenomenon occurring at an interface of bulk media. At a microscopic level, the phenomenon involves diffractive transmission of light through atomic or molecular level scatterers and interference among the produced wavelets. An intrinsic connection is evident between refraction and grating diffraction in that both phenomena involve diffractive transmission and interference, with their difference being at vastly different length scales, that is, the atomic/molecular level spacing of scatterers versus the wavelength level of aperture spacing [142]. We report negative refraction of visible light enabled by a nanostructured thin film grating that is placed in conventional positive-index media, that is, at a silica/air interface.

## 8.2 DIFFRACTIVE TRANSMISSION AND INTERFERENCE THROUGH AN ARRAY OF VERTICAL NANOSLITS

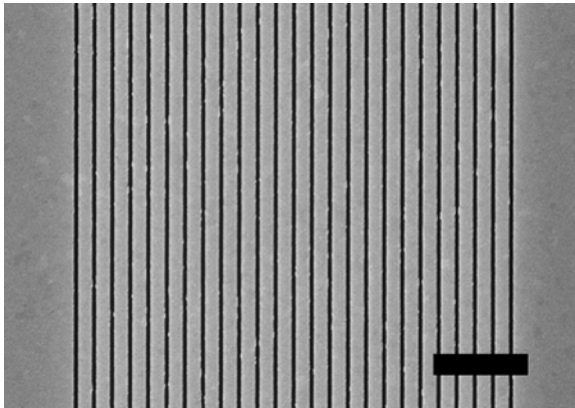
### 8.2.1 Fabrication of vertical and horizontal nanoslit arrays

Figure 8.1 (a) shows a SEM image of saw-tooth profile that contains vertical steps. The vertical nanoaperture array structure was fabricated in the following steps. First a quartz substrate was focused-ion-beam (FIB: Seiko SMI-3050SE) etched in order to form a saw-tooth profile that contains vertical steps (200-nm height) at periodic locations (760 nm grating period). A Ga ion beam (30 keV; 10-pA beam current) was used with dwell time progressively increased for deeper etching along the grating vector direction. Each grating-period span (760 nm) was divided into 40 sub-blocks (19-nm wide and 50- $\mu\text{m}$  long) in the step-wise progressive etching. A 140-nm-thick Ag layer was then deposited on the steps by thermal evaporation. In order to avoid metal deposition on the steps' sidewalls, the deposition angle was slightly tilted (10 degrees) from the substrate normal. The resulting slit width on the sidewall is estimated to be 60 nm. For a 25-period grating sample thus fabricated, the patterned area is 19  $\mu\text{m}$  x 50  $\mu\text{m}$ .

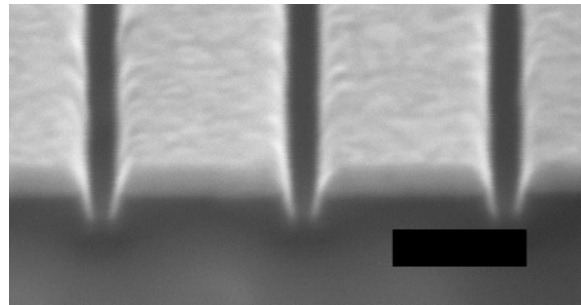
Also, a conventional nanoslit array structure with in-plane horizontal dipole apertures was fabricated (Figure 8.1 (b)). First, a 140-nm-thick Ag layer was deposited on a quartz substrate by thermal evaporation of Ag. Nanoslit arrays (100 nm width and 50  $\mu\text{m}$  length) were then formed in the Ag layer using a focused-ion-beam etching technique (Seiko SMI-3050-SE dual beam system: 30-keV Ga ion beam; 10-pA beam current). The typical etch depth for the nanoslits was 200 nm. The grating period of 25 slit arrays was 760 nm.



(a)



(b)



(c)

**Figure 8.1** SEM image of the vertical and horizontal nanoaperture arrays fabricated using a focused-ion-beam etching technique. (a) A saw-tooth pattern that contains vertical steps (200-nm height) at periodic locations (760 nm grating period) (scale bar, 400 nm). (b) and (c) A conventional nanoslit array structure with in-plane horizontal dipole apertures (140-nm-thick Ag layer on a quartz substrate). (b) Top view (scale bar, 4  $\mu\text{m}$ ). (c) Cross section view (scale bar, 500 nm).

### 8.2.2 Measurement setup

The profiles of optical transmission through the nanoslit arrays were imaged by scanning a nanoprobe ((Veeco Aurora NSOM probe 1720-00: 100-nm-thick Al coated; 80-nm diameter aperture; formed on a tapered, single-mode silica fiber with core diameter of 4  $\mu\text{m}$  and NA of 0.11; 1400  $\mu\text{m}$  total length of the tapered section coated with Al; full tapered angle of  $4^\circ$ ) [143,144]. TM-polarized He-Ne laser beam (633 nm wavelength, 1-mm beam diameter) was incident to the substrate side, and the scanning probe was scanned in the near- to far-field regime of the exit side of the nanoaperture array. The probe output was measured with a photomultiplier tube (Hamamatsu H7468-20). The scanning probe experiments were carried out with a home-built scanning stage setup (PI E-621.1CD for nanopositioning and E-665.CR for servo control) interfaced with LabView 7.0 (National Instruments). Figure 8.2 shows the schematic drawing of the measurement scanned across an array of vertical dipole apertures with the nanoprobe fiber aligned perpendicular to the substrate surface. The scan range was 60  $\mu\text{m}$  on the horizontal direction and 40  $\mu\text{m}$  in the vertical direction. The step size of scan was 50 nm and 157 nm in the horizontal and vertical directions, respectively.

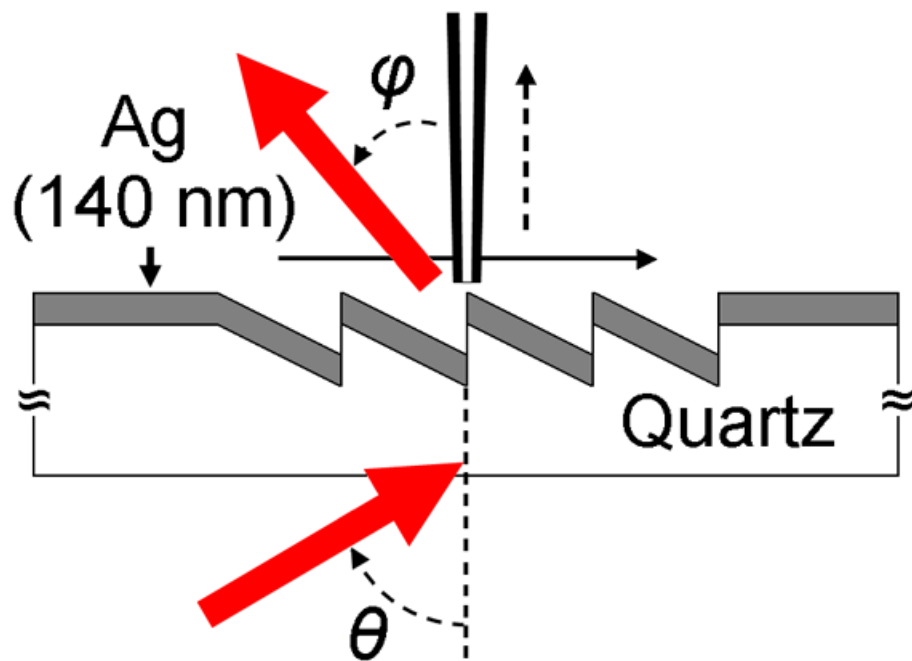


**Figure 8.2** Schematic drawing of the measurement setup. A TM-polarized light (633 nm wavelength) is incident to a periodically-slanted metal film with vertical nanoslits (140-nm thickness; 760-nm period; 60-nm slit width) from the substrate side, and the transmitted beam profile is imaged by scanning a nanoapertured fiber probe.

### 8.3 THEORY AND CHARACTERIZATION

Figure 8.3 shows FDTD simulation of radiation patterns of three different structures of a single nanoslit formed on a Ag layer. The dielectric constant of Ag was assumed to be  $-16+i1.1$  at 633 nm [145]. The simulation window was  $20\ \mu\text{m} \times 15\ \mu\text{m}$ . The FDTD results were generated using a 2D Yee mesh with 10-nm grid spacing and perfectly matched layer (PML) boundary conditions [146]. An array of vertical dipole apertures formed on a periodically-slanted metal film is utilized in redirecting the energy flow into the negative refraction direction via diffractive transmission and interference. In this design, each nanoslit aperture serves as a dipole-like line source that oscillates perpendicular to the metal film under excitation by an incident wave. For a transverse magnetic (TM)-polarized light incident to an aperture, the metal responds by inducing surface currents. At the opposing edges across the gap, the induced currents work differently on charges, that is, accumulating charges at one edge while depleting at the other. The dipole oscillation at the aperture then reradiates the incident energy into the direction tilted away from the substrate normal (Figure 8.4). When formed into an array, the ratio of the grating period to the wavelength can be designed such that the aperture radiations make constructive interference into a certain direction that falls within the radiation pattern of individual aperture. In the language of grating diffraction, this aperture array supports only the  $-1^{\text{st}}$  order diffraction (negative refraction) and blocks the  $0^{\text{th}}$  order (direct transmission) and other diffraction for a wide range of incident angles.

To demonstrate the concept, Ag nanoslit arrays (760-nm grating period) were fabricated with two different aperture orientations, vertical or horizontal dipoles. The conventional nanoslit array with in-plane horizontal dipole apertures shows the  $0^{\text{th}}$  order transmission (positive refraction) as the dominant beam as expected (Figure 8.5 (a)). In contrast, the vertical nanoslit

array shows the -1<sup>st</sup> order beam only, for the same incident angle of a TM-polarized light (633 nm wavelength) (Figure 8.5 (b)). The negative refraction enabled by the vertical dipole array can be described by the Bragg law of diffraction gratings (Figure 8.6):

$$\frac{2\pi}{\lambda}(d \sin \theta + d \sin \varphi) = -2\pi m$$

$$\sin \theta + \sin \varphi = -\frac{m\lambda}{d}$$

$$\sin \varphi = -\sin \theta - \frac{m\lambda}{d}$$

Here  $\theta$  is the incident angle measured at the air side of substrate, and  $\varphi$  is the refraction angle measured to the negative refraction direction.  $d$  is the grating period, and  $\lambda$  is the free space wavelength.  $m$  is an integer representing the diffraction order. Measurement results for a range of incident angles (0 to 45°) are summarized in Figure 8.7.

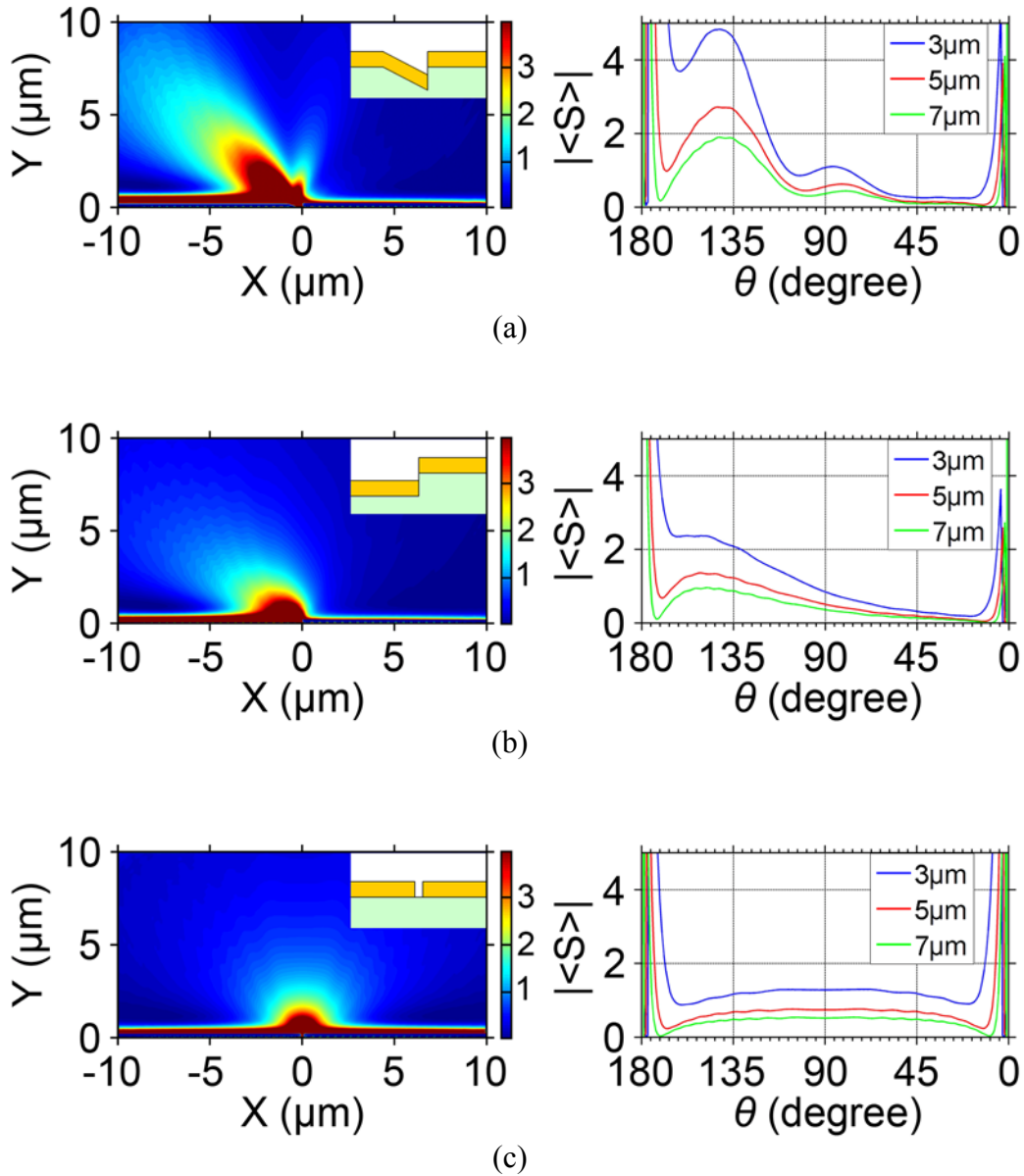


**Figure 8.3** FDTD simulation of radiation patterns of three different structures of a single nanoslit formed on a Ag layer: The dipole aperture is either vertically ((a) and (b)) or horizontally (c) oriented to the substrate. Poynting vector distributions: magnitude maps ((a), (b), and (c) left) and angular profiles of magnitude scanned at three different radial distances ((a), (b), and (c) right). A TM-polarized light (633 nm wavelength) is incident normal to the substrate. The thickness of Ag is 200 nm. The slit width (horizontal or vertical apertures) is 60 nm. The width of the sloped portion of metal in (a) is 760 nm. The angle  $\theta$  refers to the positive x-direction.

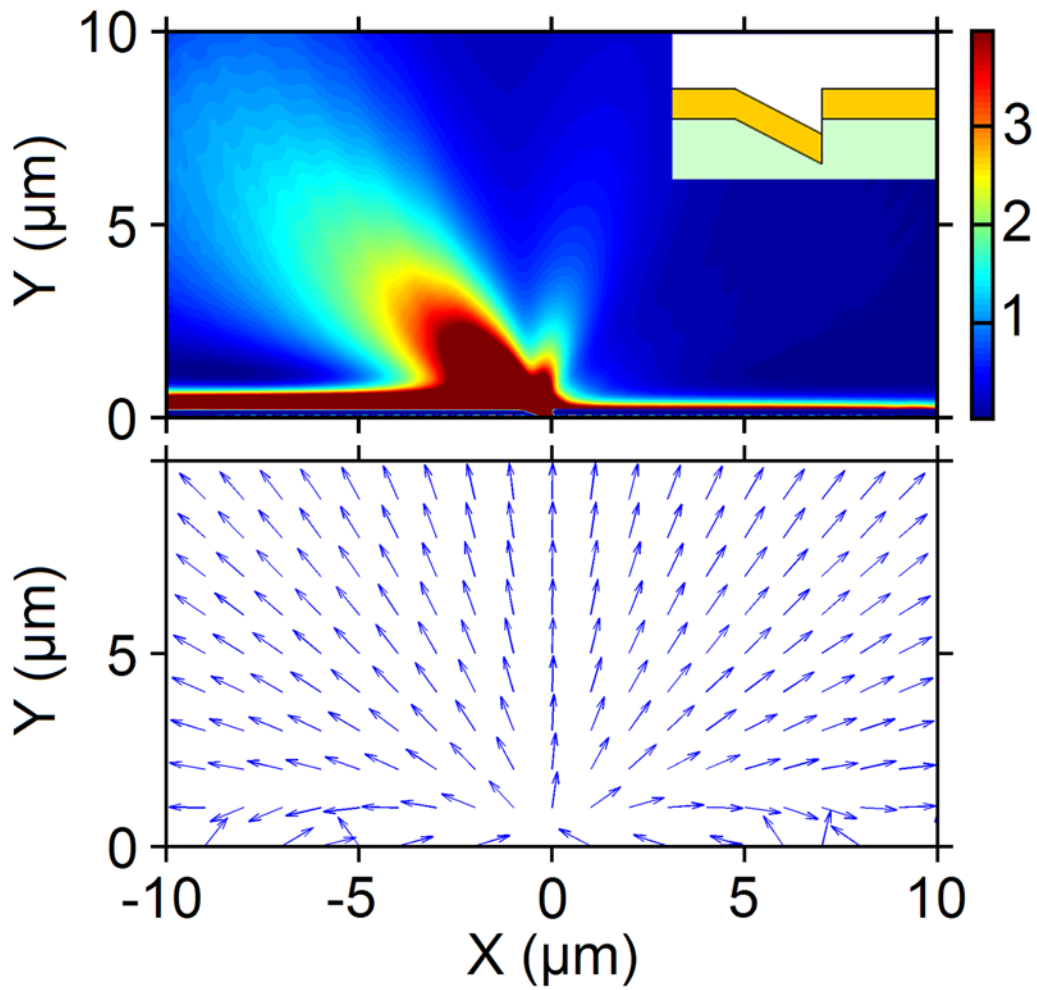
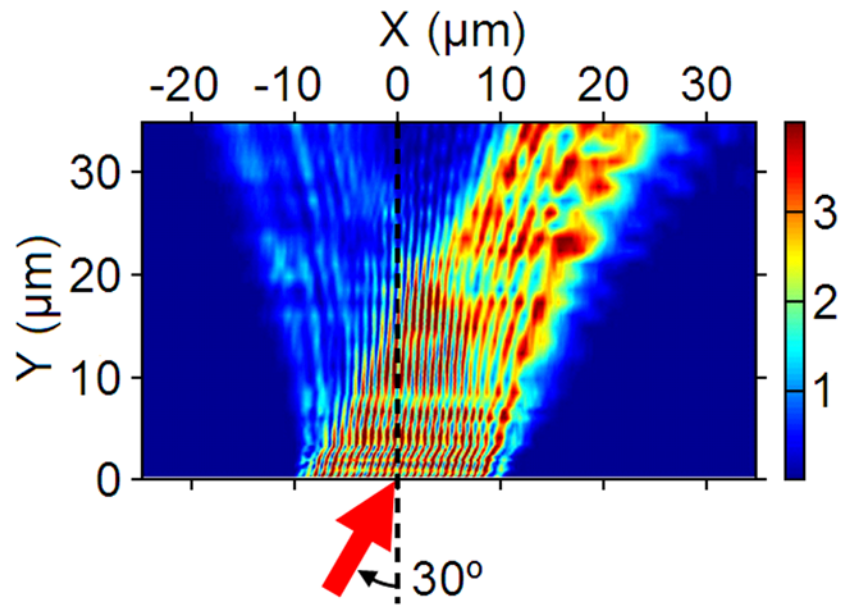
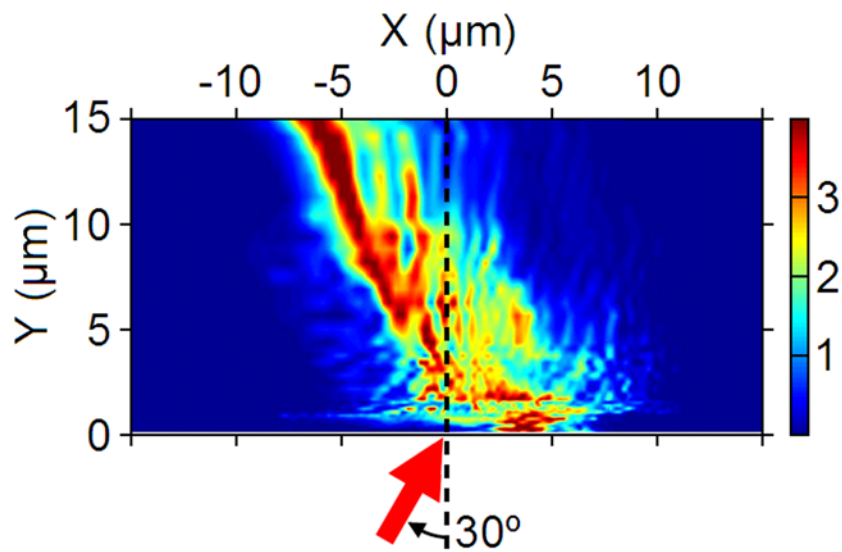


**Figure 8.4** Radiation pattern of a single vertical nanoslit calculated by finite-difference time-domain analysis: magnitude (top) and orientation (bottom) maps of Poynting vectors.



(a)



(b)

**Figure 8.5** Negative refraction of light through a metal film with an array of vertical dipole apertures. (a) Measured beam profile of a conventional nanoslit array with in-plane horizontal dipole apertures. (b) Measured beam profile of a nanoslit array with vertical dipole apertures. Negative refraction (with  $20^\circ$  refraction angle for  $30^\circ$  incident angle) is observed, which corresponds to the  $-1^{\text{st}}$  order diffraction from the grating.

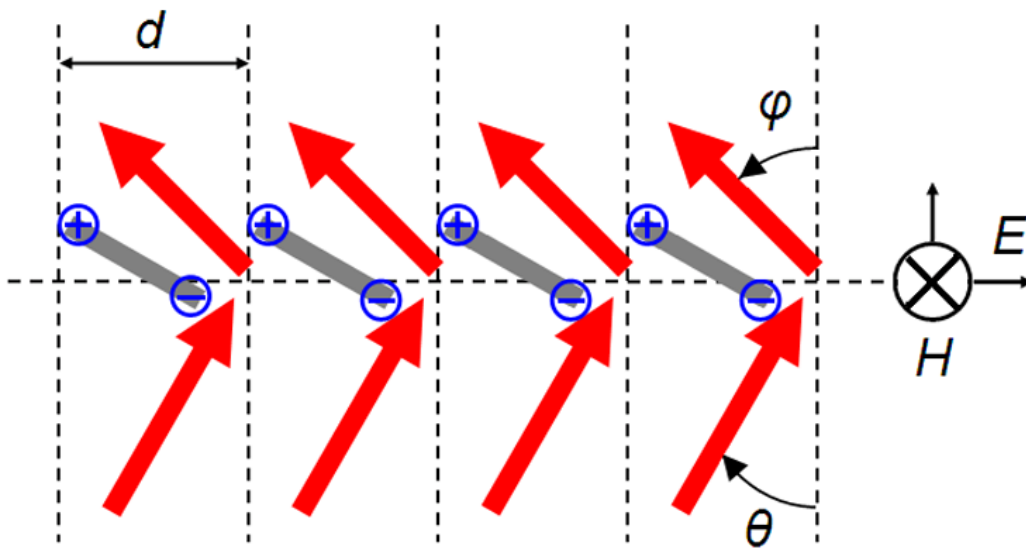


**Figure 8.6** Schematic drawing of the vertical dipole arrays.  $\theta$  is the incident angle measured at the air side of substrate, and  $\phi$  is the refraction angle measured to the negative refraction direction.  $d$  is the grating period.

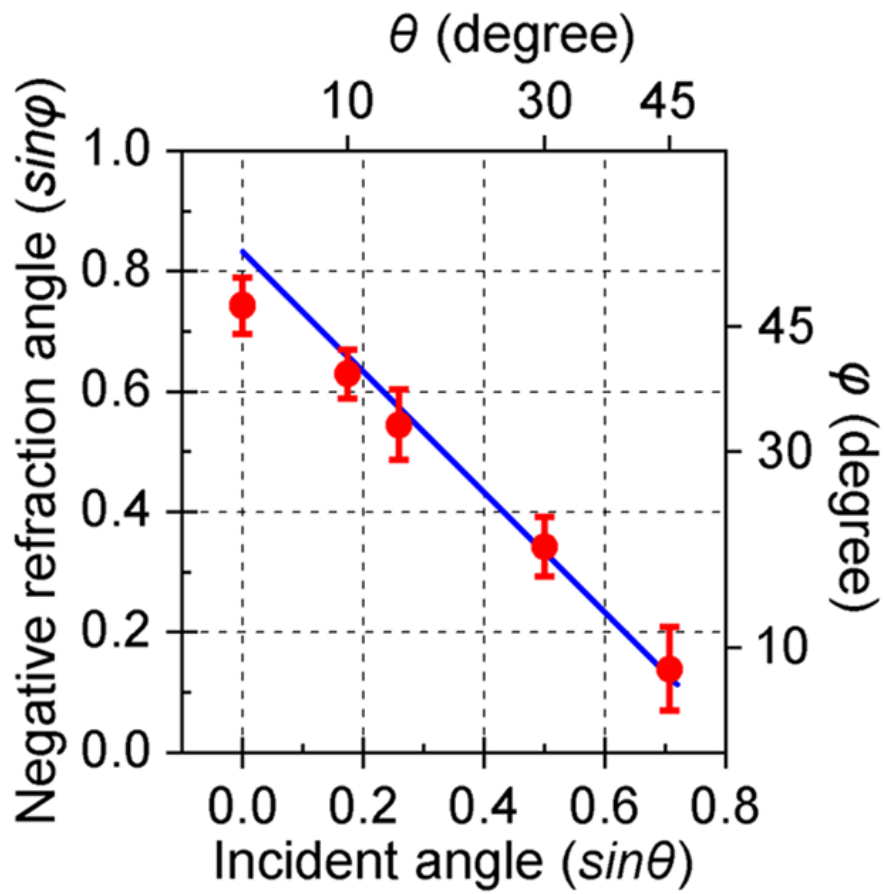


**Figure 8.7** Negative refraction angle measured as a function of incident angle. The solid line corresponds to the calculation based on the Bragg's diffraction law.

## 8.4 SUMMARY

Unlike the case of bulk metamaterials, which commonly suffer from high propagation-loss, the negative refraction enabled by this nanostructured metal film can reach the far field regime without any such loss. Most metamaterials rely on resonance phenomena, and negative refraction is limited to narrow spectral ranges [147]. In contrast, the negative refraction via grating diffraction can operate at arbitrary wavelengths. By locally varying the grating period and/or the tilt angle of individual aperture, the transmission profile can also be adjusted to match the incident beam profile. The interfacial negative refraction without bulk media loss offers a promising approach to accessing angular ranges that have not been reachable in conventional optics.

## 9.0 CONCLUSION

In this thesis, we have investigated metallic nanostructures as a medium for plasmon interactions. Surface plasmon waves excited a metallic structure can produce many interesting phenomena that can be observed in the near-field to far-field regime. The scope of this study covers both experimental and theoretical aspects. The metallic nanostructures studied in this thesis include nanoslit arrays with variable number of slits, ranging from single, to 2-10 or a large number ( $> 1000$ ). The spatial extent of SP fields is usually an order of magnitude smaller than the optical wavelength. Therefore, the structures are designed to span nano to micrometer length scales in order to accommodate wave interactions at different length scales, i.e., the slit width of the 10 nm order and the grating period of the 100 nm order.

We have developed novel fabrication processes to form nanoaperture arrays of various geometries. In forming metallic nanoslit arrays, we first fabricate a periodic mesa structure on an optically transparent dielectric substrate using a holographic lithography or electron beam lithography, followed by reactive ion etching of substrate material. With angled deposition of metal, a nanoaperture array is formed on the mesa substrate without involving direct etching of metal. As an alternative method we also employ a direct etching process using a focused-ion-beam (FIB) system.

We have investigated surface plasmon interactions in a metallic nanoslit array structure that shows characteristic transmission spectra with well-defined transmission minima and

maxima in the visible-to-infrared range. Peak transmission of ~60 % is observed for TM polarization at a wavelength red-shifted from the point of surface plasmon (SP) resonance at the metal/substrate interface. At the transmission minima, the angular dependence of reflection shows a sharp peak with minimum loss of optical power. Two types of surface plasmon excitation are found responsible for the observed transmission dips: 1) the SP resonance along the planes that comprise either the metal/air or metal/substrate interfaces for the shorter wavelength region dips, and 2) the SP resonance localized along the surface that encloses each metal island separated by slits for the longer wavelength region dip.

We have investigated the effects of thermal annealing on the surface plasmon resonance characteristics in the arrays. The spatial extension of SP waves is usually an order of magnitude smaller than the wavelength along the propagation direction. This is to accommodate the interactions of waves (plasmonic and photonic) with the structure involving different length scales. Anneal treatment of a deposited metal film is expected to alter the microstructure of metal (such as grain boundaries, surface roughness, etc.) and the size and shape of each metal island separated by slits, and thus the gap between them (i.e., slit width). This annealing-induced change of metal that may occur at nano- to microscale is expected to sensitively affect the SP interactions with the metal.

We report a transmission SPR sensor based on a metal nanoslit array structure. Optical transmission through metal nanoslit arrays shows characteristic spectra involving surface plasmon resonances that occur at various sections of the metal surfaces. We have chemically modified metal nanoslit array surfaces with alkanethiol self-assembled monolayers, and have characterized the resulting spectral shift of optical transmission. Adsorption of a self-assembled monolayer (1.5-nm thick) on a silver nanoslit array (slit width of 30-50 nm and grating period of

360 nm) is found to cause an 11 nm red-shift of the main transmission peak. Analysis of the plasmonic fields and charge distributions shows that the strong confinement of optical fields in the narrow slit region allows sensitive transduction of surface modification into a shift of surface plasmon resonance wavelength. The nano-slit-array-based surface plasmon spectroscopy is amenable to ultracompact miniaturization of instruments for biochemical sensing.

We have studied the anomalous behavior of surface plasmons that are excited in a resonant cavity structure of a metal nanoslit array. We show that the modification of a metal nanoslit array by a SAM film can give rise to either a red-shift or a blue-shift in the peak transmission wavelength. The sign of the wavelength shift depends on the surface-plasmon dispersion characteristics in the resonant cavity structure that corresponds to the stripe periphery of a nanoslit array, and they can be controlled by the composition of the metal film and the substrate that supports it. A simple model was developed to predict the wavelength shift and its sign. We show that the blue-shift of the transmission peak's wavelength, observed with adsorption of a SAM film on the metal surface, is caused by the interplay of anomalous dispersion and quadrupolar resonance of surface plasmons in the cavity structure.

We report the radiation pattern (radial and angular distribution of light intensity) of a thick (140 nm thick) silver nanoslit measured in the near- to far-fields by linearly scanning a nanoapertured probe along the radial direction with the probe axis tilted parallel to the scan direction. In most of the far-field regime the  $1/r$  dependence is clearly observed. In the glancing angle regime, the radiation pattern is found to be significantly affected by the presence of surface plasmons, showing higher intensity closer to the metal surface. In the near- to intermediate regime where the finite aperture sizes of the slit and the probe have an effect of destructive interference, the intensity profiles fall off faster than the  $1/r$  dependence. A detailed

understanding gained in this study on how the different propagation components behave and interplay in the near- to far-fields is expected to serve as an important base when studying advanced plasmonic structures.

We discuss near- to far-field measurement of optical wavefronts emanating from a nanoslit formed in a thin (50 nm thick) Ag film. The evolution of optical phases is imaged using a self-interference technique in conjunction with a scanning probe method. The phase relationship of the slit-transmitted waves with respect to the direct transmission through the thin metal film is quantitatively established. The singular-phase points resulting from the interplay of slit diffraction and surface plasmons are identified in the intermediate-field region. Imaging of optical wavefronts in the near- to far-fields is expected to be important in designing advanced nano-optic and plasmonic structures where precise control of optical phase is essential.

Finally, we report negative refraction of visible light enabled by a nanostructured thin film grating that is placed in conventional positive-index media, that is, at a silica/air interface. The negative refraction via grating diffraction can operate at arbitrary wavelengths. By locally varying the grating period and/or the tilt angle of individual aperture, the transmission profile can also be adjusted to match the incident beam profile. The interfacial negative refraction without bulk media loss offers a promising approach to accessing angular ranges that have not been reachable in conventional optics.

## REFERENCES

- [1] M. L. Brongersma, and P. G. Kik (ed.), *Surface Plasmon Nanophotonics* (Springer Series in Optical Sciences 131, Springer, 2007).
- [2] H. Raether, *Surface Plasmons on Smooth and Rough Surfaces and on Gratings* (Springer-Verlag, Berlin, 1988).
- [3] S. A. Maier, *Plasmonics: Fundamentals and Applications* (Springer, 2007).
- [4] J. A. Porto, F. J. Garcia-Vidal, and J. B. Pendry, *Phys. Rev. Lett.* 83, 2845 (1999).
- [5] M. Born, and E. Wolf, *Principles of Optics* (7<sup>th</sup> edition, Cambridge University Press, 1999).
- [6] Z. Sun, *Study of Metallic Nano-Optic Structures* (Ph.D. dissertation, University of Pittsburgh, 2005).
- [7] C. F. Bohren, and D. R. Huffman, *Absorption and Scattering of Light by Small Particles* (John Wiley & Sons, 1983).
- [8] K. Cho, H. Hori, and K. Kitahara, *Nano-Optics* (S. Kawata, M. Ohtsu, and M. Irie (ed.), Springer-Verlag, Berlin, Heidelberg and New York, 2002).
- [9] C. Kittel, *Introduction to Solid State Physics* (8<sup>th</sup> edition, John Wiley & Sons, 2005).
- [10] E. D. Palik (ed.), *Handbook of Optical Constants of Solids* (Academic Press, New York, 1998).
- [11] A. Liebsch, *Electronic Excitations at Metal Surfaces* (Plenum Press, New York and London, 1997).
- [12] T. W. Ebbesen, H. J. Lezec, H. F. Ghaemi, T. Thio, and P. A. Wolff, *Nature* 391, 667 (1998).
- [13] H. F. Ghaemi, T. Thio, D. E. Grupp, T. W. Ebbesen, and H. J. Lezec, *Phys. Rev. B* 58, 779 (1998)

- [14] D. E. Grupp, H. J. Lezec, T. W. Ebbesen, K. M. Pellerin, and T. Thio, *Appl. Phys. Lett.* 77, 1569 (2000).
- [15] T. J. Kim, T. Thio, T. W. Ebbesen, D. E. Grupp, and H. J. Lezec, *Opt. Lett.* 24, 256 (1999).
- [16] T. Thio, H. J. Lezec, T. W. Ebbesen, K. M. Pellerin, G. D. Lewen, A. Nahata, and R. A. Linke, *Nanotechnology* 13, 429 (2002).
- [17] A. Krishnan, T. Thio, T. J. Kim, H. J. Lezec, T. W. Ebbesen, P. A. Wolff, J. Pendry, L. Martin-Moreno, and F. J. Garcia-Vidal, *Opt. Commun.* 200, 1 (2001).
- [18] U. Schröter and D. Heitmann, *Phys. Rev. B* 58, 15419 (1998).
- [19] M. M. J. Treacy, *Phys. Rev. B* 66, 195105 (2002).
- [20] J. A. Porto, F. J. Garcia-Vidal, and J. B. Pendry, *Phys. Rev. Lett.* 83, 2845 (1999).
- [21] Y. Takakura, *Phys. Rev. Lett.* 86, 5601 (2001).
- [22] Q. Cao and P. Lalanne, *Phys. Rev. Lett.* 88, 057403 (2002).
- [23] F. J. Garcia-Vidal and L. Martin-Moreno, *Phys. Rev. B* 66, 155412 (2002).
- [24] T. Lopez-Rios, D. Mendoza, F. J. Garcia-Vidal, J. Sanchez-Dehesa, and B. Pannetier, *Phys. Rev. Lett.* 81, 665 (1998).
- [25] Z. Sun, Y. S. Jung, and H. K. Kim, *Appl. Phys. Lett.* 83, 3021 (2003).
- [26] A. Degiron, H. J. Lezec, W. L. Barnes, and T. W. Ebbesen, *Appl. Phys. Lett.* 81, 4327 (2002).
- [27] L. Martin-Moreno, F. J. Garcia-Vidal, H. J. Lezec, K. M. Pellerin, T. Thio, J. B. Pendry, and T. W. Ebbesen, *Phys. Rev. Lett.* 86, 1114 (2001).
- [28] E. D. Palik (ed.), *Handbook of Optical Constants of Solids* (Academic Press, New York, 1998).
- [29] T. Ito and K. Sakoda, *Phys. Rev. B* 64, 045117 (2001).
- [30] P. W. Barber, R. K. Chang, and H. Massoudi, *Phys. Rev. Lett.* 50, 997 (1983).
- [31] W. L. Barnes, A. Dereus, and T. W. Ebbesen, *Nature* 424, 824 (2003)
- [32] J. A. Porto, F. J. Garcia-Vidal, and J. B. Pendry, *Phys. Rev. Lett.* 83, 2845 (1999).
- [33] F. J. Garcia-Vidal and L. Martin-Moreno, *Phys. Rev. B* 66, 155412 (2002).
- [34] Q. Cao and P. Lalanne, *Phys. Rev. Lett.* 88, 057403 (2002).

- [35] M. M. J. Treacy, Phys. Rev. B 66, 195105 (2002).
- [36] Z. Sun and H. K. Kim, Appl. Phys. Lett. 85, 642 (2004).
- [37] Z. Sun, Y. S. Jung, and H. K. Kim, Appl. Phys. Lett. 83, 3021 (2003).
- [38] Z. Sun, Y. S. Jung, and H. K. Kim, Appl. Phys. Lett. 86, 023111 (2005).
- [39] H. Raether, *Surface Plasmons on Smooth and Rough Surfaces and on Gratings* (Springer-Verlag, Berlin, 1988).
- [40] J. I. Goldstein et al., *Scanning Electron Microscopy and X-ray Microanalysis* (Plenum Press, New York, 1992)
- [41] C. V. Thompson, Annu. Rev. Mater. Sci. 30, 159 (2000).
- [42] P. Lalanne, C. Sauvan, J. P. Hugonin, J. C. Rodier, and P. Chavel, Phys. Rev. B 68, 125404 (2003).
- [43] Y. Xie, A. R. Zakharian, J. V. Moloney, and M. Mansuripur, Opt. Express 13, 4485 (2005).
- [44] P. Yeh, *Optical Waves in Layered Media* (Wiley, Hoboken, 1998)
- [45] E. D. Palik (ed.), *Handbook of Optical Constants of Solids* (Academic Press, New York, 1998).
- [46] W. L. Barnes, T. W. Preist, S. C. Kitson, and J. R. Sambles, Phys. Rev. B 54, 6227 (1996).
- [47] J. Homola, S. S. Yee, and G. Gauglitz, Sensors and Actuators B 54, 3-15 (1999).
- [48] H. Raether, *Surface Plasmons on Smooth and Rough Surfaces and on Gratings* (Springer-Verlag, Berlin, 1988).
- [49] T. A. Leskova, A. A. Maradudin, and W. Zierau, Opt. Commun. 249, 23 (2005).
- [50] M. D. Malinsky, K. L. Kelly, G. C. Schatz, and R. P. Van Duyne, J. Am. Chem. Soc. 123, 1471 (2001).
- [51] J. C. Riboh, A. J. Haes, A. D. McFarland, C. R. Yonzon, and R. P. Van Duyne, J. Phys. Chem. B 107, 1772 (2003).
- [52] S. M. Williams, A. D. Stafford, K. R. Rodriguez, T. M. Rogers, and J. V. Coe, J. Phys. Chem. B 107, 11871 (2003).
- [53] A. G. Brolo, R. Gordon, B. Leathem, and K. L. Kavanagh, Langmuir 20, 4813 (2004).
- [54] M. Lahav, A. Vaskevich, and I. Rubinstein, Langmuir 20, 7365 (2004).

- [55] W. L. Barnes, A. Dereus, and T. W. Ebbesen, *Nature* 424, 824 (2003).
- [56] J. A. Porto, F. J. Garcia-Vidal, and J. B. Pendry, *Phys. Rev. Lett.* 83, 2845 (1999).
- [57] A. Degiron, H. J. Lezec, W. L. Barnes, and T. W. Ebbesen, *Appl. Phys. Lett.* 81, 4327 (2002).
- [58] Z. Sun, Y. S. Jung and H. K. Kim, *Appl. Phys. Lett.* 83, 3021 (2003).
- [59] C. J. Love, L. A. Estroft, J. K. Kriebel, R. G. Nuzzo, and G. M. Whitesides, *Chem. Rev.* 105, 1103 (2005).
- [60] W. L. Barnes, T. W. Priest, S. C. Kitson, and J. R. Sambles, *Phys. Rev. B* 54, 6227- (1996).
- [61] Y. S. Jung, Z. Sun, H. K. Kim, *Appl. Phys. Lett.* 87, 263116 (2005).
- [62] Z. Sun, Y. S. Jung, and H. K. Kim, *Appl. Phys. Lett.* 86, 023111 (2005).
- [63] Z. Sun and H. K. Kim, *Appl. Phys. Lett.* 85, 642 (2004).
- [64] I. P. Kaminow, W. L. Mammel, and H. P. Weber, *Appl. Opt.* 13, 396 (1974).
- [65] E. D. Palik (ed.), *Handbook of Optical Constants of Solids* (Academic Press, New York, 1998).
- [66] J. D. Jackson, *Classical Electrodynamics*, (3<sup>rd</sup> edition, Wiley, NJ, 1999).
- [67] R. W. Boyd and D. J. Gauthier, *Progress in Optics*, Vol. 43 (E. Wolf (ed.), Elsevier, 2002)
- [68] S. Chu and S. Wong, *Phys. Rev. Lett.* 48, 738 (1982).
- [69] A. M. Steinberg and R. Y. Chiao, *Phys. Rev. A* 49, 2071 (1994).
- [70] A. Dogariu, K. Kuzmich, and L. J. Wang, *Phys. Rev. A* 63, 053806 (2001).
- [71] A. M. Akulshin, S. Barreiro, and A. Lezama, *Phys. Rev. Lett.* 83, 4277 (1999).
- [72] G. Wähling, D. Möbius, and H. Raether, *Z. Naturforsch* 33a, 907 (1978).
- [73] G. Wähling, *Z. Naturforsch* 36a, 588 (1981).
- [74] I. Pockrand, A. Brillante, and D. Möbius, *J. Chem. Phys.* 77, 6289 (1982).
- [75] I. Pockrand and J. D. Swalen, *J. Opt. Soc. Am.* 68, 1147 (1978).
- [76] H. Raether, *Surface Plasmons on Smooth and Rough Surfaces and on Gratings* (Springer-Verlag, Berlin, 1988).

- [77] Z. Sun, Y. S. Jung, and H. K. Kim, *Appl. Phys. Lett.* 83, 3021 (2003).
- [78] H. J. Lezec, J. A. Dionne, and H. A. Atwater, *Science* 316, 430 (2007).
- [79] J. Homola, S. S. Yee, and G. Gauglitz, *Sens. Actuators B* 54, 3 (1999).
- [80] U. Kreibig and M. Vollmer, *Optical properties of metal clusters* (Springer-Verlag, Berlin, 1995).
- [81] C. F. Bohren and D. R. Huffman, *Absorption and Scattering of Light by Small Particles*, (Wiley, New York, 1983).
- [82] Q. Cao, and P. Lalanne, *Phys. Rev. Lett.* 88, 057403 (2002).
- [83] Y. Xie, A. R. Zakharian, J. V. Moloney, and M. Mansuripur, *Opt. Express* 13, 4485 (2005).
- [84] D. Pacifici, H. J. Lezec, H. A. Atwater, and J. Weiner, *Phys. Rev. B* 77, 115411 (2008).
- [85] Y. S. Jung, J. Wuenschell, H. K. Kim, P. Kaur, L. Wang, and D. Waldeck, *Appl. Phys. Lett.* 88, 243105 (2006).
- [86] M. D. Malinsky, K. L. Kelly, G.C. Schatz, and R. P. Van Duyne, *J. Am. Chem. Soc.* 123, 1471 (2001).
- [87] M. J. Kofke, D. H. Waldeck, Z. Fakhraai, S. Ip, and G. C. Walker *Appl. Phys. Lett.* 94, 023104 (2009).
- [88] Referring to Equation (6.3),  $N_{top}$  and  $N_{bottom}$  are calculated to be 1.04 and 1.59, respectively.  $N_{slit}$  is estimated to be 1.35 from Ref. [86]. Here the following values are used:  $\epsilon_{Ag} = -13.3+i0.2$  and  $\epsilon_{SiO_2} = 2.1$  at 600 nm wavelength (Ref. [87]),  $L = 360$  nm, and  $t = 100$  nm.
- [89] Z. Sun and H. K. Kim, *Appl. Phys. Lett.* 85, 642 (2004).
- [90] E. D. Palik (ed.), *Handbook of Optical constants of solids* (Academic Press, New York, 1998).
- [91] D. M. Sullivan, *Electromagnetic Simulation Using the FDTD Method* (IEEE Press, NJ, 2000)
- [92] C. J. Love, L. A. Estroft, J. K. Kriebel, R. G. Nuzzo, and G. M. Whitesides, *Chem. Rev.* 105, 1103 (2005).
- [93] The dielectric constant versus frequency data were taken from Ref. [87].
- [94] E. Hecht, *Optics*, (4<sup>th</sup> edition, Addison-Wesley, New York, 2002).
- [95] D. W. Pohl, W. Denk, and M. Lanz, *Phys. Lett.* 44, 651 (1984).

- [96] F. Zenhausern, M. P. O'Boyle, and H. K. Wickramasinghe, *Appl. Phys. Lett.* 65, 1623 (1994).
- [97] T. W. Ebbesen, H. J. Lezec, H. F. Ghaemi, T. Thio, and P. A. Wolff, *Nature* 391, 667 (1998).
- [98] W. L. Barnes, A. Dereux, and T. W. Ebbesen, *Nature* 424, 824 (2003).
- [99] J. D. Jackson, *Classical Electrodynamics*, (3<sup>rd</sup> edition, Wiley, New York, 1999).
- [100] R. Wannemacher, *Opt. Commun.* 195, 107 (2001).
- [101] P. B. Johnson and R. W. Christy, *Phys. Rev. B* 6, 4370 (1972).
- [102] H. Raether, *Surface Plasmons on Smooth and Rough Surfaces and on Gratings* (Springer-Verlag, Berlin, 1988).
- [103] G. Gay, O. Alloschery, B. V. De Leseigno, C. O'Dwyer, J. Weiner, and H. J. Lezec, *Nature Phys.* 2, 262 (2006).
- [104] P. Lalanne and J. P. Hugonin, *Nature Phys.* 2, 551 (2006).
- [105] M. W. Kowarz, *Appl. Opt.* 34, 3055 (1995).
- [106] L. Chen, J. T. Robinson, and M. Lipson. *Opt. Express* 14, 12629 (2006).
- [107] A. Sommerfeld, *Optics* (Academic Press, New York, 1964).
- [108] H. J. Lezec, A. Degiron, E. Devaux, R. A. Linke, L. Martin-Moreno, F. J. Garcia-Vidal and T. W. Ebbesen, *Science* 297, 820 (2002).
- [109] L. Yin, V. K. Vlasko-Vlasov, A. Rydh, J. Pearson, U. Welp, S. -H. Chang, S. K. Gray, G. C. Schatz, D. B. Brown, and C. W. Kimball, *Appl. Phys. Lett.* 85, 467 (2004).
- [110] P. Lalanne and J. P. Hugonin, *Nature Phys.* 2, 551 (2006).
- [111] K. G. Lee, H. W. Kihm, J. E. Kihm, W. J. Choi, H. Kim, C. Ropers, D. J. Park, Y. C. Yoon, S. B. Choi, D. H. Woo, J. Kim, B. Lee, Q. H. Park, C. Lienau, and D. S. Kim, *Nature Photon.* 1, 53 (2007).
- [112] B. Hecht, B. Sick, U. P. Wild, V. Decker, R. Zenobi, O. J. F. Martin, and D. W. Pohl, *J. Chem. Phys.* 112, 7761 (2000).
- [113] R. Ulrich, *Opt. Commun.* 13, 259 (1975).
- [114] D. M. Sullivan, *Electromagnetic Simulation Using the FDTD Method* (IEEE Press, New York, 2000).

- [115] E. D. Palik (ed.), *Handbook of Optical Constants of Solids* (Academic Press, New York, 1998).
- [116] J. Nkoma, R. Loudon, and D. R. Tilley, *J. Phys. C: Solid State Phys.* 7, 3547 (1974).
- [117] J. Wuenschell, and H. K. Kim, *Opt. Express* 14, 10000 (2006).
- [118] C. Genet and T. W. Ebbesen, *Nature* 445, 39-46 (2007).
- [119] H. J. Lezec, A. Degiron, E. Devaux, R. A. Linke, L. Martín-Moreno F. J. García-Vidal, and T. W. Ebbesen, *Science* 297, 820-822 (2002).
- [120] L. Yin, V. K. Vlasko-Vlasov, A. Rydh, J. Pearson, U. Welp, S.-H. Chang, S. K. Gray, G. C. Schatz, D. B. Brown, and C. W. Kimball, *Appl. Phys. Lett.* 85, 467-469 (2004).
- [121] G. Gay, O. Alloschery, B. Viaris de Lesegno, C. O'Dwyer, J. Weiner, and H. J. Lezec, *Nature Phys.* 2, 262-267 (2006).
- [122] P. Lalanne and J. P. Hugonin, *Nature Phys.* 2, 551-556 (2006).
- [123] L. Chen, J. T. Robinson, and M. Lipson, *Opt. Express* 14, 12629-12636 (2006).
- [124] F. López-Tejeira, Sergio G. Rodrigo, L. Martín-Moreno, F. J. García-Vidal, E. Devaux, T. W. Ebbesen, J. R. Krenn, I. P. Radko, S. I. Bozhevolnyi, M. U. González, J. C. Weeber, and A. Dereux, *Nature Phys.* 3, 324-328 (2007).
- [125] K. G. Lee, H. W. Kihm, J. E. Kihm, W. J. Choi, H. Kim, C. Ropers, D. J. Park, Y. C. Yoon, S. B. Choi, D. H. Woo, J. Kim, B. Lee, Q. H. Park, C. Lienau, and D. S. Kim, *Nature Photon.* 1, 53-56 (2007).
- [126] L. Aigouy, P. Lalanne, J. P. Hugonin, G. Julie' and V. Mathet, and M. Mortier, *Phys. Rev. Lett.* 98, 153902(1)-(4) (2007).
- [127] Y. S. Jung, J. Wuenschell, T. Schmidt, and H. K. Kim, *Appl. Phys. Lett.* 92, 02310(1)-(3) (2008).
- [128] T. W. Ebbesen, H. J. Lezec, H. F. Ghaemi, T. Thio, and P. A. Wolff, *Nature* 391, 667-669 (1998).
- [129] H. Raether, *Surface Plasmons on Smooth and Rough Surfaces and on Gratings* (Springer-Verlag, Berlin, 1988).
- [130] Z. Sun, Y. S. Jung, and H. K. Kim, *Appl. Phys. Lett.* 83, 3021-3023 (2003).
- [131] J. N. Walford, K. A. Nugent, A. Roberts, and R. E. Scholten, *Appl. Opt.* 38, 3508-3515 (1999).
- [132] M. L. Balistreri, J. P. Korterik, L. Kuipers, and N. F. van Hulst, *Phys. Rev. Lett.* 85, 294-297 (2000).

- [133] A. Nesci, R. Dändliker, and H. P. Herzig, *Opt. Lett.* 26, 208-210 (2001).
- [134] D. M. Sullivan, *Electromagnetic Simulation Using the FDTD Method* (IEEE Press, New York, 2000).
- [135] E. D. Palik (ed.), *Handbook of Optical Constants of Solids* (Academic Press, New York, 1998).
- [136] P. B. Johnson and R. W. Christy, *Phys. Rev. B* 6, 4370-4379 (1972).
- [137] J. Wuenschell and H. K. Kim, *Opt. Express* 14, 10000-10013 (2006).
- [138] V. G. Veselago, *Sov. Phys. Usp.* 10, 509 (1968).
- [139] J. B. Pendry, *Phys. Rev. Lett.* 85, 3966 (2000).
- [140] H. J. Lezec, J. A. Dionne, and H. A. Atwater, *Science* 316, 430 (2007).
- [141] J. Yao, Z. Liu, Y. Liu, Y. Wang, C. Sun, G. Bartal, A. M. Stacy, and X. Zhang, *Science* 321, 930 (2008).
- [142] Z. Sun and H.K. Kim, *Appl. Phys. Lett.* 85, 642 (2004).
- [143] Y. S. Jung, J. Wuenschell, T. Schmidt, and H. K. Kim, *Appl. Phys. Lett.* 92, 02310 (2008).
- [144] Y. S. Jung, Y. Xi, J. Wuenschell, and H. K. Kim, *Optics Express*, 16, 18881 (2008)
- [145] E. D. Palik (ed.), *Handbook of Optical Constants of Solids* (Academic Press, New York, 1998).
- [146] D. M. Sullivan, *Electromagnetic Simulation Using the FDTD Method* (IEEE Press, New York, 2000).
- [147] R. A. Shelby, D. R. Smith, and S. Schultz, *Science* 292, 77 (2001).

## JOURNAL PAPERS PUBLISHED

1. Y. S. Jung, Y. Xi, J. Wuenschell, and H. K. Kim, "Near- to Far-field Imaging of Phase Evolution of Light Emanating from a Metal Nanoslit", *Optics Express*, 16, 18881-18888 (2008) and *Virtual Journal of Nanoscale Science & Technology*, Vol. 18, 23 (2008).
2. Y. S. Jung, J. Wuenschell, T. Schmidt, and H. K. Kim, "Near- to Far-field Imaging of Free-Space and Surface-bound Waves Emanating from a Metal Nanoslit", *Applied Physics Letters*, 92, 023104(1)-023104(3) (2008) and *Virtual Journal of Nanoscale Science & Technology*, Vol. 17, 4 (2008).
3. A. Kubo, Y. S. Jung, H. K. Kim, and H. Petek, "Femtosecond Microscopy of Localized and Propagating Surface Plasmons in Silver Gratings", *Journal of Physics B: Atomic, Molecular and Optical Physics*, 40, S259-S272 (2007).
4. H. K. Kim, Y. S. Jung, J. Wuenschell, Z. Sun, P. Kaur, L. Wang, and D. Waldeck "Plasmonic Phenomena in Metal Nanoapertures and Chip-scale Instrumentation for Biochemical Sensing", *Proceedings of IEEE Nanotechnology Materials and Devices Conference*, Vol. 1, pp. 144-145 (2006).
5. Y. S. Jung, Z. Sun, J. Wuenschell, H. K. Kim, P. Kaur, L. Wang, and D. Waldeck, "High-Sensitivity Surface-plasmon-resonance Spectroscopy Based on a Metal Nanoslit Array", *Applied Physics Letters*, 88, 243105(1)-243105(3) (2006).
6. Y. S. Jung, Z. Sun, H. K. Kim, and J. Blachere, "Blueshift of Surface Plasmon Resonance Spectra in Anneal-treated Silver Nanoslit Arrays", *Applied Physics Letters*, 87, 263116(1)-263116(3) (2005).
7. A. Kubo, K. Onda, H. Petek, Z. Sun, Y. S. Jung, and H. K. Kim, "Femtosecond Imaging of Surface Plasmon Dynamics in a Nano-structured Silver Film", *Nano Letters*, 5, 1123-1127 (2005).
8. Z. Sun, Y. S. Jung, and H. K. Kim, "Dynamic Evolution of Surface Plasmon Resonances in Metallic Nanoslit Arrays", *Applied Physics Letters*, 86, 023111(1)-023111(3) (2005).
9. H. K. Kim, Z. Sun, Y. S. Jung, and M. Liu, "Nano-optic Chip Technology", *Proceedings of the 2nd International Workshop on Advanced Materials for Information Technology and Applications: Organic/Inorganic Nanoelectronics and Nanophotonics*, pp. 21-26, 2004 (invited paper).

10. Z. Sun, Y. S. Jung, and H. K. Kim, "Role of Surface Plasmons in the Optical Interaction in Metallic Gratings with Narrow Slits", *Applied Physics Letters*, 83, 3021-3023 (2003).